



PHD

## Magnetic Induction Tomography Spectroscopy for Liquid Metal Applications

Muttakin, Imamul

*Award date:*  
2022

*Awarding institution:*  
University of Bath

[Link to publication](#)

### Alternative formats

If you require this document in an alternative format, please contact:  
[openaccess@bath.ac.uk](mailto:openaccess@bath.ac.uk)

Copyright of this thesis rests with the author. Access is subject to the above licence, if given. If no licence is specified above, original content in this thesis is licensed under the terms of the Creative Commons Attribution-NonCommercial 4.0 International (CC BY-NC-ND 4.0) Licence (<https://creativecommons.org/licenses/by-nc-nd/4.0/>). Any third-party copyright material present remains the property of its respective owner(s) and is licensed under its existing terms.

#### Take down policy

If you consider content within Bath's Research Portal to be in breach of UK law, please contact: [openaccess@bath.ac.uk](mailto:openaccess@bath.ac.uk) with the details. Your claim will be investigated and, where appropriate, the item will be removed from public view as soon as possible.

# Magnetic Induction Tomography Spectroscopy for Liquid Metal Applications

Imamul Muttakin

A thesis submitted for the degree of Doctor of Philosophy

University of Bath

Department of Electronic and Electrical Engineering

September 2021

## **COPYRIGHT**

Attention is drawn to the fact that copyright of this thesis rests with the author and copyright of any previously published materials included may rest with third parties. A copy of this thesis has been supplied on condition that anyone who consults it understands that they must not copy it or use material from it except as licenced, permitted by law or with the consent of the author or other copyright owners, as applicable.

### **Declaration of any previous submission of the work**

The material presented here for examination for the award of a higher degree by research has not been incorporated into a submission for another degree.

Candidate's typed signature: Imamul Muttakin

### **Declaration of authorship**

I am the author of this thesis, and the work described therein was carried out by myself personally.

Candidate's typed signature: Imamul Muttakin

# Abstract

The industrial sector continuously demands innovation in sensing technology. Identification of flow conditions, gas/void detection, and porosity estimation are important factors in many liquid metal processes. This thesis aims to demonstrate the magnetic induction tomography (MIT) system in a liquid metal process model at a laboratory scale.

The work designs MIT instrumentations which are able to acquire measurement data from eight coils system. The frequency range is between 100 Hz to 100 kHz enabling multi-frequency measurement. Its signal-to-noise ratio (SNR) reached 66 dB with a speed of 1.5 s/frame to produce real, imaginary, amplitude, and phase data and reconstructed images. On the software side, spatio-spectral image reconstruction algorithm has been formulated to do a spectrally correlated analysis identifying an object's circumstances.

MIT sensors have been constructed for detecting and visualising liquid metal flow. Typical flow shapes have been successfully recovered with a correlation coefficient up to 0.9 and relative error as low as 0.2. In addition, a liquid metal shape classifier based on a neural network yields a test accuracy of 99%. As for interior voids in liquid metal, a convolutional neural network has been trained to quantify the number of non-metallic inclusions with 96% of test accuracy.

This research also develops a vector-based complex mutual inductance spectroscopic imaging and derives regional complex impedance diagrams. The resulting complex plots from the reconstruction comprehensively indicate the functional and structural characteristics of the metallic materials. Furthermore, this investigation for the first time demonstrates a novel thermal mapping system using eddy current based spectroscopic imaging data. Inductive based temperature mapping devices can have great potential applications where none of the existing thermal measuring devices could work noninvasively.

This study intends to contribute to the context of eddy current, imaging, and induction spectroscopy.



Alhamdulillah

I dedicate this to my family

## Acknowledgments

First and foremost, I profoundly thank my supervisor, Prof. Manuchehr Soleimani, for all his support within four years of research work. It is a privilege to join his group and get infected with the passion of doing experiments. I would like to thank PhD confirmation examiner: Dr Martin Fullekrug, Dr Kang Ma; PhD viva examiner: Dr Stephen Pennock and Dr Wuliang Yin (the University of Manchester), for their review and feedback improve the thesis. I also acknowledge Dr Thomas Wondrak (HZDR), Mr Dirk van der Plas, Mr Sjaak van Oord, and Dr Daniel van Odyck (Tata Steel) for their suggestions on some of the experiments. It has been a pleasure collaborating with TOMOCON Early Stage Researchers and, among them, colleagues in the continuous casting demonstration group: Artem, Ivan, and Shereen. I want to thank people with whom I engage along the project: Mrs Susann Riedel, Mr Thomas Gundrum, Dr Klaus Timmel, Dr Matthias Ratajczak (HZDR), Mr Raimund Kirchschrager (Primetals), Dr Arto Voutilainen, Mr Mika Mononen (Rocsole), Prof. Aleš Richter, and Dr Jaroslav Hlava (Technical University of Liberec). Lots of help during my time at the University that I should mention Mr Gavin Dingley, Mr David Chapman, Mrs Ann Linfield, Dr Hugo Jenks, Dr Siva Sivaraya, and Mr Mike Linham, to name but a few. Last but not least, to friends of Engineering Tomography Lab and Herschel Office: Panos, Gege, Chenning, Fang, Victor, Habila, Miguel, Simon, Manasavee, Carl, Yandan, Ander, Bo, Xi, Quanbao, fellow Indonesians in the UK, especially in Bristol and Bath, Thoni, Budi, and Hilda, thank you all.

This project has received funding from the European Union's Horizon 2020 research and innovation programme under the Marie Skłodowska-Curie grant agreement No 764902. Part of this research made use of the Balena High Performance Computing (HPC) Service at the University of Bath. Gratitude is expressed to PIU-IsDB UNTIRTA for the opportunity to embark on overseas study.

# Contents

<b>1</b>	<b>Introduction</b>	<b>15</b>
1.1	Background and Motivation . . . . .	15
1.2	Aims and Objectives . . . . .	19
1.3	Statement of Originality . . . . .	19
1.4	Contributions . . . . .	19
1.5	Thesis Organisation . . . . .	20
<b>2</b>	<b>Liquid Metal Flow Measurement</b>	<b>22</b>
2.1	Electrical Capacitance Tomography . . . . .	22
2.2	Magnetic Induction Tomography . . . . .	25
2.3	Contactless Inductive Flow Tomography . . . . .	30
2.4	Application . . . . .	32
2.5	Summary . . . . .	34
<b>3</b>	<b>Magnetic Induction Tomography Spectroscopy</b>	<b>36</b>
3.1	Forward Problem . . . . .	36
3.2	Inverse Problem . . . . .	39
3.2.1	Tikhonov Method . . . . .	39
3.2.2	Landweber Iteration Method . . . . .	40
3.2.3	Spatio-Spectral Total Variation . . . . .	41
3.2.4	Neural Network . . . . .	43
3.3	Measurement System . . . . .	45
3.3.1	Magnitude-Based Hardware . . . . .	46
3.3.2	Hardware System for Spectroscopy . . . . .	48
3.3.3	Complex-Valued Hardware . . . . .	50

3.4	Summary . . . . .	60
<b>4</b>	<b>Visualisation of Liquid Metal Flow Shape</b>	<b>61</b>
4.1	Introduction . . . . .	61
4.2	Continuous Casting Model . . . . .	62
4.3	Sensor Design . . . . .	63
4.4	Measurement Setup . . . . .	64
4.5	Visualisation Result . . . . .	65
4.6	Classification using Neural-Network . . . . .	68
4.7	Conclusion . . . . .	73
<b>5</b>	<b>Structural and Functional Characterisation in Metallic Materials</b>	<b>74</b>
5.1	Introduction . . . . .	74
5.2	Experimental Setup . . . . .	77
5.3	Results and Analysis . . . . .	82
5.3.1	Single Metal Sample . . . . .	83
5.3.2	Different Samples at Different Locations . . . . .	85
5.3.3	Non-Conductive Inclusion in Conductive Liquid . . . . .	86
5.3.4	Spectral Derivative for Structural and Functional Classification . . . . .	89
5.3.5	Complex Plot of Normalised Impedance from Reconstruction . . . . .	92
5.4	Discussion . . . . .	96
5.5	Conclusion . . . . .	97
<b>6</b>	<b>Conductivity and Temperature Sensing</b>	<b>98</b>
6.1	Introduction . . . . .	98
6.2	Method . . . . .	100
6.3	Spectroscopy . . . . .	104
6.3.1	Mutual Impedance on Conductivity Level . . . . .	104
6.3.2	Mutual Impedance on Conductive Structure . . . . .	106
6.3.3	Spectral Imaging of Mutual Impedance . . . . .	107
6.4	Application . . . . .	114
6.4.1	Inclusion in Liquid Metal . . . . .	114
6.4.2	Temperature Sensing . . . . .	116

6.5	Discussion . . . . .	121
6.6	Conclusion . . . . .	123
<b>7</b>	<b>Interior Void Classification in Liquid Metal</b>	<b>124</b>
7.1	Introduction . . . . .	124
7.2	Machine Learning Method . . . . .	125
7.3	FCNN Classifier . . . . .	126
7.4	CNN Classifier . . . . .	132
7.5	Discussion . . . . .	137
7.6	Conclusion . . . . .	138
<b>8</b>	<b>Conclusion</b>	<b>139</b>
8.1	Summary . . . . .	139
8.2	Limitations and Further Work . . . . .	140
	<b>Appendix</b>	<b>142</b>
	<b>References</b>	<b>143</b>

# List of Figures

2-1	ECT measurement concept . . . . .	23
2-2	MIT measurement concept. . . . .	26
2-3	Sensitivity map. . . . .	29
2-4	CIFT principle and setup . . . . .	32
2-5	Mini-LIMMCAST construction . . . . .	33
2-6	Input output control model . . . . .	34
3-1	COMSOL model . . . . .	38
3-2	NN pipeline . . . . .	44
3-3	CNN concept . . . . .	45
3-4	Magnitude-based hardware . . . . .	46
3-5	Simulation receiver circuits . . . . .	48
3-6	Spectroscopy hardware . . . . .	49
3-7	Complex-valued hardware . . . . .	50
3-8	Tx Rx characteristic . . . . .	51
3-9	Measurement SNR . . . . .	52
3-10	PCB design . . . . .	53
3-11	Hardware control flowchart . . . . .	54
3-12	Demodulation scheme . . . . .	55
3-13	Signal demodulation . . . . .	57
3-14	Measurement data . . . . .	58
3-15	Complex image reconstruction . . . . .	59
4-1	Mini-LIMMCAST scheme . . . . .	62
4-2	Sensor design. . . . .	63
4-3	Experiment for liquid metal in SEN tube. . . . .	65

4-4	MIT imaging for metal flow scenarios in SEN. . . . .	66
4-5	Neural network classifier model. . . . .	70
4-6	Training and validation accuracy-loss vs epoch. . . . .	71
4-7	Prediction flow shape . . . . .	72
4-8	Normalised confusion matrix. . . . .	73
5-1	Measurement setup . . . . .	77
5-2	Background measurement . . . . .	78
5-3	Amplitude spectrum of a test sample . . . . .	78
5-4	Phase spectrum of a test sample . . . . .	79
5-5	Spectral plot for metallic samples . . . . .	80
5-6	Spectral plot for size variations . . . . .	80
5-7	Spectral plot for metallic structure . . . . .	81
5-8	Spectral derivative for conductivity variations . . . . .	81
5-9	Spectral derivative for size variations . . . . .	82
5-10	Spectral derivative for metallic structures . . . . .	82
5-11	Spectral profile and its derivative copper . . . . .	83
5-12	Spectral profile and its derivative aluminum . . . . .	84
5-13	Spectral profile and its derivative brass . . . . .	84
5-14	Spectral profile and its derivative GaInSn . . . . .	85
5-15	Spectral profile and its derivative positions . . . . .	87
5-16	Spectral profile and its derivative single inclusion . . . . .	88
5-17	Spectral profile and its derivative multiple inclusions . . . . .	88
5-18	Spectral gradient conductivity variations . . . . .	89
5-19	Spectral gradient size variations . . . . .	90
5-20	Spectral gradient structure variations . . . . .	91
5-21	Complex plot conductivity variations . . . . .	93
5-22	Complex plot structure variations . . . . .	94
5-23	Complex plot size variations . . . . .	94
5-24	Complex plot inclusions . . . . .	95
5-25	Complex plot locations . . . . .	95
6-1	Behaviour of conductive body as function of voltage–frequency . .	100
6-2	Mutual impedance measurement scheme. . . . .	101
6-3	Multi-channels setup for tomographic projection system. . . . .	102

6-4	Reference measurement. . . . .	103
6-5	Spatial arrangement of objects in the sensing region and example of MIT image . . . . .	104
6-6	Mutual impedance spectrum conductive samples. . . . .	105
6-7	Phase spectrum conductive samples. . . . .	105
6-8	Mutual impedance spectrum conductive structures. . . . .	106
6-9	Phase spectrum conductive structures. . . . .	107
6-10	Mutual impedance spectrum aluminum . . . . .	109
6-11	Phase spectrum aluminum . . . . .	110
6-12	Mutual impedance spectrum imaging conductivity . . . . .	112
6-13	Phase spectrum imaging conductivity . . . . .	113
6-14	Experiment setup for liquid metal inclusion. . . . .	114
6-15	Mutual impedance liquid metal inclusion . . . . .	115
6-16	Experiment setup for temperature sensing. . . . .	116
6-17	Mutual impedance temperature sensing . . . . .	117
6-18	Conductive objects distribution and the impedance-phase spectrum	118
6-19	Spatial and spectral color map. . . . .	119
6-20	Reconstruction value vs temperature difference in heat map. . . .	120
6-21	Experiment setup for temperature sensing in pipe. . . . .	121
7-1	Experiment setup liquid metal with inclusion . . . . .	126
7-2	1D data plot . . . . .	128
7-3	Wood inclusions cases . . . . .	128
7-4	Neural network architecture . . . . .	129
7-5	FCNN accuracy loss epoch . . . . .	130
7-6	FCNN prediction case . . . . .	131
7-7	FCNN confusion matrix . . . . .	132
7-8	Pseudo image layout . . . . .	133
7-9	CNN model . . . . .	133
7-10	CNN accuracy loss epoch . . . . .	135
7-11	CNN predictions . . . . .	136
7-12	CNN confusion matrix . . . . .	137



# List of Tables

3.1	Measurement Index . . . . .	38
3.2	Hardware Timing . . . . .	58
3.3	Hardware Comparison . . . . .	60
4.1	Sensor Parameter . . . . .	64
4.2	Imaging Evaluation . . . . .	67
4.3	Flow Shape Dataset . . . . .	69
4.4	NN Model Summary . . . . .	69
4.5	NN Performance Evaluation . . . . .	70
6.1	Conductivity of Tested Objects . . . . .	106
7.1	FCNN Model Summary . . . . .	129
7.2	CNN Model Summary . . . . .	134

# List of Abbreviations

<b>SEN</b> Submerged entry nozzle	<b>BiCGStab</b> Bi-conjugate gradient stabilized method
<b>UTT</b> Ultrasound transmit-time	<b>ADC</b> Analog to digital converter
<b>MIT</b> Magnetic induction tomography	<b>VCCS</b> Voltage-controlled current source
<b>ECT</b> Electrical capacitance tomography	<b>Op-Amp</b> Operational amplifier
<b>CIFT</b> Contactless inductive flow tomography	<b>USB</b> Universal serial bus
<b>AI</b> Artificial intelligence	<b>PC</b> Personal computer
<b>ML</b> Machine learning	<b>SCPI</b> Standard commands for programmable instruments
<b>AC</b> Alternating current	<b>FPGA</b> Field-programmable gate-array
<b>EMT</b> Electromagnetic inductance tomography	<b>DIO</b> Digital input-output
<b>DC</b> Direct current	<b>TCP</b> Transmission control protocol
<b>LIMMCAST</b> Liquid Metal Model of Continuous Casting	<b>SPICE</b> Simulation Program with Integrated Circuit Emphasis
<b>UDV</b> Ultrasonic doppler velocimetry	<b>SNR</b> Signal to noise ratio
<b>Tx</b> Transmitter	<b>ESR</b> Equivalent series resistance
<b>Rx</b> Receiver	<b>PCB</b> Printed circuit board
<b>TV</b> Total variation	<b>BNC</b> Bayonet Neill-Concelman

<b>SMA</b> Sub-Miniature Version A	<b>ReLU</b> Rectified linear unit
<b>DDS</b> Direct digital synthesis	<b>ADAM</b> Adaptive with momentum
<b>AVR</b> Alf-Egil Bogen Vegard Wollan RISC microcontroller	<b>CPU</b> Central processing unit
<b>ARM</b> Advanced RISC Machines	<b>RAM</b> Random access memory
<b>HZDR</b> Helmholtz-Zentrum Dresden- Rossendorf	<b>MIS</b> Magnetic induction spectroscopy
<b>AWG</b> American Wire Gauge	<b>MITS</b> Magnetic induction tomography spectroscopy
<b>PMMA</b> Poly methyl methacrylate	<b>IRT</b> Infrared thermography
<b>PLA</b> Polylactic acid	<b>NMI</b> Non-metallic inclusions
<b>CC</b> Correlation coefficient	<b>FCNN</b> Fully connected neural network
<b>RE</b> Relative error	<b>CNN</b> Convolutional neural network
<b>NN</b> Neural network	<b>CFD</b> Computational fluid dynamics

# List of Symbols

$A$ – Magnetic potential	$T$ – Electric vector potential
$B$ – Magnetic flux density	$V$ – Voltage
$C$ – Capacitance	$v$ – Velocity
$E$ – Electric field	$Z$ – Electric impedance
$f$ – frequency	$\mu$ – Magnetic permeability
$H$ – Magnetic field intensity	$\varepsilon$ – Electrical permittivity
$I$ – Electric current	$\sigma$ – Electrical conductivity
$J$ – Electric current density	$\theta$ – Phase
$M$ – Mutual inductance	$\phi$ – Electric potential distribution
$Q$ – Electric charge	$\omega$ – Angular frequency
$R_m$ – Reynolds number	

# Chapter 1

## Introduction

### 1.1 Background and Motivation

Metal has become an essential element for engineering. Steel, as a prominent example of metal-based materials, is used in almost every product in human life. In 2020, apparent steel use reaches 1772 million tonnes worldwide, an increase from 1315 million tonnes a decade ago. This translates to 228 kg of finished steel products use per capita. To this day, the production of steel consumes a huge amount of energy which is sourced mostly from fossil fuel, hence carbon footprint. On average, every tonne of steel produced led to the emission of 1.85 tonnes of  $CO_2$  into the atmosphere, thus representing 7–9% of global anthropogenic emissions [1]. From the steelmaking engineering perspective, yield improvement to increase output is directly linked to energy and material reduction. Process reliability reduces losses in quality and process time so that energy use per tonne of steel is also suppressed. Therefore, an innovation that results in efficiency in this industrial sector will benefit engineering, social-economic, as well as environmental aspects.

Around 96.9% of the world's crude steel output comes from the continuous casting process [1]. Continuous casting is a process to solidify steel in the form of a continuous strand. Molten steel carried in the ladle is transferred into tundish which acts as a reservoir. The tundish has a hole(s) for pouring liquid steel into the nozzle. The flow is regulated by a sliding gate or stopper rod. An inlet

in the upper nozzle is used to inject gas for preventing clogging and removing impurities. Then, the steel flows through the nozzle into open-bottomed, water-cooled moulds. As the molten steel passes through the mould, the outer shell solidifies.

In continuous casting, flow regime, phase distribution, as well as gas inclusion in the submerged entry nozzle (SEN) are very important phenomena related to steel quality [2]. It is desired to anticipate flow patterns and ensure cleanliness before the shell is solidified further down the mould. Clogging nozzle causes asymmetrical, chaotic flow, and highly fluctuated meniscus level [3] which are bad for shell formation. Proper concentration of gas injection helps to remove impurities, but an excessive amount of gas could be trapped in the solid shell becoming defects. A comprehensive measurement of such has not yet been achieved because there is no unique measurement technique that can resolve the outer interface and bubbles in the liquid metal bulk with sufficient accuracy.

Measurement techniques for liquid metal were reviewed in [4]. Inclusion (in the form of gas bubbles) can be observed using ultrasound transit-time (UTT), contactless inductive detection, and X-ray imaging. The UTT can quantify gas bubble with diameter 5 – 7 mm without producing an image. However, any impurity or unclean medium will hinder the sound transmission, hence its detection capability. On the other hand, high-resolution X-ray can recover the gas bubbles image down to about 1 mm with a maximum thickness of the fluid layer of about 15 mm. This limitation arises due to the ray is highly attenuated through a conductive medium. Therefore, given an adequate penetration depth, the inductive method is favourable for industrial implementation.

For liquid metal fast breeder reactors, real-time radiography is used to image the system [5]. Basic research has been conducted in using neutron radiography for observing liquid metal two-phase flows in vessels. Using the technique reported in [6], radial void fraction profiles were obtained. Also, the follow-up research by the same authors [7] clarified the basic characteristics of the flow. They visualised the liquid metal two-phase flow and measured its void fraction using neutron radiography and conductivity probe, respectively. The radiography method was used earlier utilising a tracer particle [8]. However, it requires the attenuation of rays caused by the liquid metal being less than  $1/e$ , and particle size larger than

one digitised image element size. The other known method is invasive. Report by [9] discloses a probe insertion for detecting gas bubbles in liquid metals. A recent technique, optical fibre sensors were used and tested in a well-controlled lab-scale and a pilot-scale reactor [10].

Porous metal is another engineering material product that is formed in the liquid phase. Its processing method involves bubble generation where pore growth is one of the parameters of interest [11]. Although several modelling methods for liquid metal foam processing have been established [12], experimental observations are still limited. The difficulty in investigating opaque system such as metallic foam is acknowledged. In [13], X-ray tomography was used to clarify the liquid metal's dynamic phenomena, one of which is bubble arrangements.

Generally, alloy casting suffers from inclusions such as dissolved gases. A technique was demonstrated to assess the metal quality by visualising gas content, albeit only a single dissolved gas in the aluminium alloy was tested by [14]. An online liquid metal cleanliness analyzing system is used for quality assurance of inclusion sensitive products. The commercial system [15] is based on the electric sensing zone.

Electromagnetic sensors are arguably the most feasible means to do the measurement in close proximity of a harsh, high temperature, and opaque SEN at the caster. Pair of coils were designed to sense molten steel profiles such as bubbly flow, central stream, and annular flow using a wood metal model. It could differentiate those flow profiles by evaluating the relative detection values over a certain frequency range [16]. The expanded version of the sensor was then tested on the steel caster's nozzle. It was able to visualise the flow [17], as well as infer the pattern in accordance with casting parameter gas injection [18]. Tomographic configuration was introduced for imaging molten steel flow [19]. A hot trial test was conducted and able to visualise the steel flow [20].

Electromagnetic tomography is a method for generating cross-sectional images utilizing a low-radiation intensity electromagnetic field as excitation energy. It is capable of examining the electromagnetic properties of the object. Owing to a contact-less non-invasive non-intrusive low-cost system and fast imaging process, it has been rigorously appraised for various applications, from industrial

to medical, in the past three decades. Historically reported in chronological order, the modalities make use of resistance [21], capacitance [22], and inductance [23] measurements.

Magnetic induction tomography (MIT) is able to reconstruct the conductivity distribution in one cross-section of the SEN, and thereby distinguish between liquid metal and argon gas in case of a two-phase flow, in a physical model, as been done by [24]. A preliminary study for electrical capacitance tomography (ECT) as a new imaging tool for metal flow was introduced in a report from Wondrak and Soleimani [25]. ECT is capable of producing a high-quality image of the outer surface of metal flow. On the other hand, contactless inductive flow tomography (CIFT) was developed to observe the flow velocity field in the mould. This paves way for a combined tomographic imaging approach to tackle the common task in a system.

Meanwhile, the advancement in artificial intelligence (AI) is accelerated by the availability of data generated from potent sectors. Since the algorithm shows its capability for image interpretation, its implementation progressively finds the broad area of medical, industrial and informatics [26] [27]. This trend also applies in tomography technology [28] [29], where the data and/or the resulting image can be exploited to obtain conclusive outputs. Machine learning (ML) utilised in tomography research has mainly been for the reconstruction scheme [30] [31], image enhancement [32] [33], and various post-processing mechanisms [34] [35]. Those methods are rarely directly targeting primary information embedded in the measurement data. Bypassing the complexity of tomographic image reconstruction, the detection based on raw data will reduce the computational resources in the deployment phase [36]. Moreover, end-to-end learning of spatio-temporal feature from raw tomography sensor data was assessed to be an efficient scheme [37].

Key parameters in multiphase flow were predicted from multiple sensors reading using a deep-learning method [38]. The model demonstrated generalisation capability for potential field measurement. The work presented in [39] took a direct approach to map the relationship between measurements from ECT sensors and hydrodynamics parameters of flow patterns in a fluidised bed. Although the reconstruction process was still conducted to infer the process parameters, it ex-



perimentally collected training samples offline and then the model was used for online monitoring to estimate solid concentration and bubble diameter.

Among the intended implementation of tomography technology, is its incorporation into a process. This is leveraged by the ever-increasing of hardware performance, material technology, and computation power. Monitoring and/or controlling an industrial process is becoming possible. The thesis deals with the use of magnetic induction tomography and spectroscopy for liquid metal application.

## 1.2 Aims and Objectives

The development of the MIT technique would benefit from both forward-inverse solutions, as well as low-cost high-performance systems [40]. This research aims to demonstrate the MIT system in a liquid metal process model. It has several objectives:

- apply the MIT system for liquid metal process
- design and experiment of multi-frequency MIT
- design and experiment with complex impedance imaging in MIT

A multi-frequency approach is explored to elevate the MIT capability and producing rich information. This is in some ways answering the future direction from a previous thesis [41]. Furthermore, measurement and imaging of complex impedance in MIT will give more perspective on the resulting image. It also correlates to further recommendation from a prior work [42].

## 1.3 Statement of Originality

The work in this thesis is the author's original work with the supervisor that has been conducted between September 2017 to September 2021. Exceptions are conceded where reference has been cited to prior work of other people.

## 1.4 Contributions

Published peer-reviewed works which constitute the backbone of the thesis are:

1. Direct capacitance measurement for tomographic imaging of metallic objects (2018) [43]. This paper was presented at the 9th World Congress in Industrial Process Tomography. It served as an entry point to electromagnetic tomography, measurement system, and reconstruction method. Chapter 2 is partly taken from it.
2. Real-time control of the mould flow in a model of continuous casting in frame of the TOMOCON project [2], presented at 9th International Symposium on Electromagnetic Processing of Materials in 2018. Co-authored with collaborators in the working group, this paper describes a framework of the project. The proposal triggers the work in Chapter 4 and Chapter 7.
3. Magnetic induction tomography sensors for quantitative visualisation of liquid metal flow shape [44]. The publication appeared in IEEE Sensors Letters in 2020. This exposes an experimental work with liquid metal as in Chapter 4.
4. Magnetic induction tomography spectroscopy for structural and functional characterization in metallic materials [45]. This paper was published in MDPI Materials in 2020. Chapter 5 is based on this.
5. Noninvasive conductivity and temperature sensing using magnetic induction spectroscopy imaging, published in IEEE Transactions on Instrumentation and Measurement in 2021 [46]. This paper is the main source for Chapter 6.
6. Interior void classification in liquid metal using multi-frequency magnetic induction tomography with a machine learning approach, published in IEEE Sensors Journal in 2021 [47]. This paper is a direct consequence of the work in Chapter 7.

## 1.5 Thesis Organisation

The next chapter presents a briefing on measurement methods for liquid metal flow. It proposes some ideas for integrating electromagnetic tomography with a control system in a demonstration environment. It is immediately followed by chapter on MIT which covers forward formulation, inverse solution, and hardware

method. This chapter provides a general basis which is common to the remaining chapters. Chapter 4 describes MIT implementation for visualising liquid metal flow shape. It informs the direction of the applied work in the research project. In Chapter 5, the structural and functional of metallic materials are characterised. This is an example of the capability of complex MIT. Chapter 6 focuses on exploring multi-frequency MIT measurement and the resulting information for conductivity and temperature sensing. Chapter 7 deals with a machine learning approach for the problem of interior void detection in liquid metal. The last chapter presents the overall conclusions of the thesis. The importance of the results and their implications will be discussed. The limitations of the research will also be discussed.

## Chapter 2

# Liquid Metal Flow Measurement

Measurement methods have been applied for liquid metal detection. Examples of non-contact and non-invasive solutions are electrical capacitance tomography (ECT), magnetic induction tomography (MIT), and contactless inductive flow tomography (CIFT). This chapter introduces these techniques and explores the prospective on integrated implementation.

### 2.1 Electrical Capacitance Tomography

Capacitance can be used as boundary measurement to extract dielectric distribution in a sensing region. ECT has been well-known as a low-cost non-invasive non-intrusive non-radiating technique for imaging a substance that has dominant permittivity value. However, recent researches by Al Hosani [48] and Zhang [49] showed the capability of ECT to reconstruct a metal object in order to obtain information about inclusion's surface along the region of interest. This development opens an opportunity for ECT to be implemented into a wider application where the imaging target is metallic material [25].

ECT uses electrostatics approach in which the governing equation for the ECT is defined as Poisson's equation [50]:

$$\nabla \cdot \varepsilon \nabla \phi = 0 \tag{2.1}$$

Mutual capacitance ( $C$ ) between electrodes  $i - j$  is [51],

$$C_{ij} = \frac{Q_j}{\Delta V_{ij}} \quad (2.2)$$

here ( $\Delta V$ ) is voltage difference, whereas charge ( $Q$ ) at the electrode  $j$  can be written as,

$$Q_j = \oint_{\Gamma_j} \varepsilon(x, y) \nabla \phi(x, y) \cdot \hat{\mathbf{n}} d\mathbf{l} \quad (2.3)$$

combining (2.2) and (2.3) yields,

$$C_{ij} = \frac{1}{\Delta V_{ij}} \oint_{\Gamma_j} \varepsilon(x, y) \nabla \phi(x, y) \cdot \hat{\mathbf{n}} d\mathbf{l} \quad (2.4)$$

where  $\varepsilon$  is permittivity and  $\phi$  is potential,  $\Gamma_j$  is the enclosing path for detection electrodes, and  $\hat{\mathbf{n}}$  is its normal unit vector. Figure 2-1 is ECT concept illustrated through simulation. Typical ECT sensors consist of a set of electrodes from which capacitance values between electrodes will be measured as boundary measurements. The traditional implementation of ECT is directed to an object whose conductivity is low and material with low-frequency permittivity in the range of 1–100. Nevertheless, a recent development by [43] showed that it also can be conditioned to reconstruct high conductivity inclusion inside the sensor.

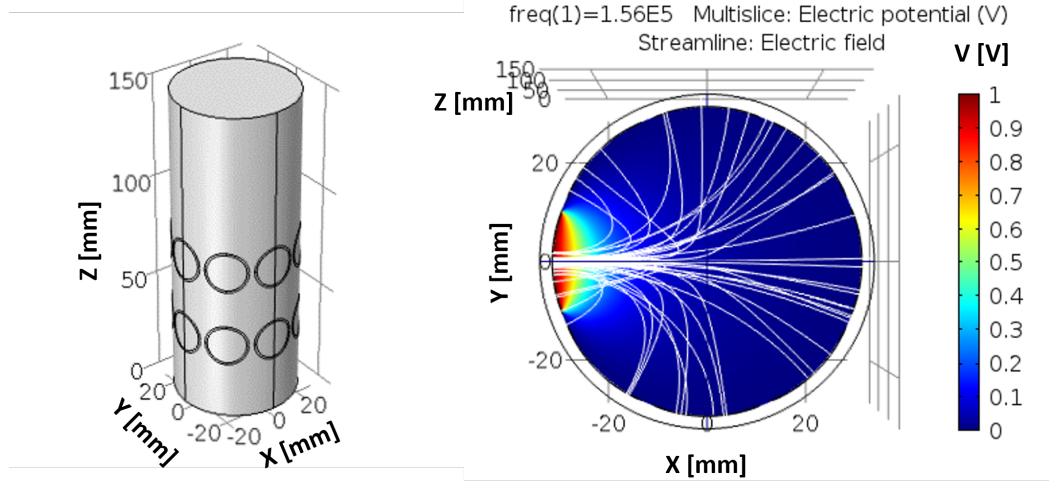


Figure 2-1: ECT measurement concept. Cylindrical vessel with set of circular capacitive electrodes (left); simulation where an electrode is energised with voltage resulting in electric field inside the vessel (right).

Conventional ECT system has a frequency in the range of 250 kHz up to 2.5 MHz with various types of excitation signal [52]. Given the implementation where the sensing space is few inches in diameter and electrode thickness less than one millimetre, the most common operating frequency is 500 kHz. This ensures an electrostatic approach is applicable due to signal wavelength significantly larger than sensor geometry or object's size [53].

For an object that is not pure dielectric, the measurement method and frequency operation should be adjusted accordingly. Primary readout circuitry for lossy capacitance value is necessary. The charge transfer principle is the foremost mean for measuring capacitance between electrodes. It also has been used since the first generation of the ECT system. Alternating current (AC) -based capacitance measurement was later adopted as an improvement in ECT hardware. Due to the nature of AC signal processing, the complexity is increased especially on phase-sensitive demodulation required to accomplish accurate measurement results [54]. On the other hand, a commercial module for capacitance measurement has been proven in electrical tomography systems as reported in [55]. It is a low-cost and easy-to-integrate solution for direct measurement in a preliminary study of capacitance tomography applications.

The concept of capacitance-based metallic object imaging is derived from the work of Zhang [49]. This method considers a metal object as dielectric inclusion inside capacitive sensor. Metal inclusion can be seen as a high permittivity object between capacitive electrodes. The term 'permittivity illusion' was used by prior work [49] to describe a pure conductive object which acts as though it was a very high dielectric substance seen by a capacitive electrode. This 'illusion' will shorten spacing between capacitance electrode pairs. In other words, the inclusion of metal (floating conductor) acts as a pseudo dielectric material that can be imaged by ECT. In addition, a three-dimensional (3D) image can also be produced with a single-plane sensor as described by [56], taking advantage of the fringe effect of the electric field.

The work in [43] proposes a method of metallic object imaging using capacitance measurement. It shows a system setup of capacitance measurement for imaging metallic inclusion inside the ECT sensor. The boundary shape of the object has been successfully retrieved by reconstruction. This method could not recover

the inner distribution of the metal object but might be complemented with a penetrating magnetic field in order to obtain the whole structure. Therefore, a combination of ECT and MIT modalities would be an attractive solution for metallurgical process imaging.

## 2.2 Magnetic Induction Tomography

Mutual inductance tomography, also known in terms of magnetic induction tomography or electromagnetic inductance tomography (EMT) [57], [58], works on several routines. The region of interest is excited by a magnetic field from the alternating current which flows through a coil. The field is then modified as a result of material distribution in the sensing space. These primary and secondary field distributions are measured using an array of coils arranged (usually) circumventing the region. The boundary measurements can be reconstructed as an image using the inversion algorithm to map the electromagnetic properties in the sensing area. In addition to an image, other means of information such as parameters or profiles are also of interest. That information can be obtained directly from measurement or derived from reconstruction results.

The method is based on trans-impedance measurement between the transmitting coil (excited by a current source) and receiving coil (from which induced voltage is sensed). Having established reference measurement with air background condition, the relationship between induced voltage  $V$  and excitation current  $I$  is,

$$V = j\omega MI \quad (2.5)$$

where  $M$  is the mutual inductance between transmitter and receiver coils. When an object with electromagnetic properties is placed in between coils, the spatial distribution of the magnetic field is perturbed. Consequently, the change in mutual inductance  $\Delta M$  raises a modification in the detection signal  $\Delta V$  at receiving coil, re-arranged into:

$$\Delta M = \frac{\Delta V}{j\omega I} \quad (2.6)$$

Here, the current is kept at an independent level.  $\Delta M$  is a complex value consists of resistive and reactive components. Magnetic material will increase the

mutual induction between coils, hence increasing the measured signal; whereas conductive material will reduce the signal. In other words, the real part of the impedance change represents a change in the magnetic flux while the imaginary part represents the loss due to the eddy currents.

Considering an imaging system where conductivity  $\sigma$  is sought, a formulation using magnetic vector potential  $\mathbf{A}$  in the conductive region [59],

$$\nabla \times \left( \frac{1}{\mu} \nabla \times \mathbf{A} \right) + j\omega\sigma\mathbf{A} = \mathbf{J}_s \quad (2.7)$$

where  $\mu$  is permeability,  $\omega$  is the angular frequency, and  $\mathbf{J}_s$  is the source's current density. MIT principle is depicted in Figure 2-2, where a coil is excited by current

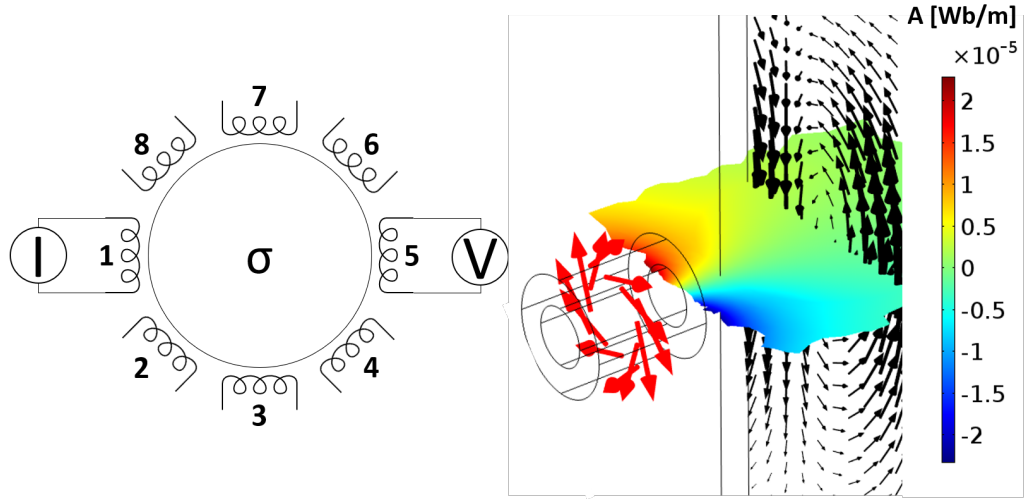


Figure 2-2: MIT measurement concept.

$I$  (red arrows), while the other coil is induced by voltage  $V$  as a result of  $\mathbf{A}$  field (surface plot) in the region with the distribution of conductivity  $\sigma$  and eddy current (black arrows). Thus, tomographic data are formed as arrays of sensors' measurement combinations. In the case of 8 sensors, each of which can act as either exciter or detector, one frame (a complete set of 'projection') consists of  $(C_2^8)$  28 readings.

A linear approximation can be applied only for a small perturbation on pixel value, and a linear response is assumed between the change in pixel value and the change in mutual inductance being measured between coil pairs. Supposed



that there are  $k$  pixel each has a value of  $p_i$  representing electromagnetic property required from a pixel, then pixel values can be arranged to be a vector  $\mathbf{P}$ . Likewise, if there are  $n$  measured coil pairs each with the measured mutual inductance of  $m_j$ , then the measured values can be arranged into vector  $\mathbf{M}$ . Small change in  $\mathbf{M}$  ( $\delta\mathbf{M}$ ) with change in  $\mathbf{P}$  ( $\delta\mathbf{P}$ ) may be linearly related through sensitivity matrix  $\mathbf{S}$  [60],

$$\delta\mathbf{M} = \mathbf{S}\delta\mathbf{P} \quad (2.8)$$

Therefore,  $\mathbf{S}$  is Jacobian matrix in the system where:

$$\delta\mathbf{P} = \begin{bmatrix} \delta P_1 \\ \vdots \\ \delta P_i \\ \vdots \\ \delta P_k \end{bmatrix}; \delta\mathbf{M} = \begin{bmatrix} \delta M_1 \\ \vdots \\ \delta M_j \\ \vdots \\ \delta M_n \end{bmatrix}; \mathbf{S} = \begin{bmatrix} \frac{\partial m_1}{\partial p_1} & \cdots & \frac{\partial m_1}{\partial p_k} \\ \vdots & \ddots & \vdots \\ \frac{\partial m_n}{\partial p_1} & \cdots & \frac{\partial m_n}{\partial p_k} \end{bmatrix} \quad (2.9)$$

Due to signal's change is relative to empty (air) background,  $\delta\mathbf{P}$  and  $\delta\mathbf{M}$  are simply notated as  $\mathbf{P}$  and  $\mathbf{M}$  respectively. This coefficient  $\mathbf{S}$  can be obtained experimentally by scanning small test object as a perturbation in the sensing space and measuring the response on every coil pairs accordingly. However, the common approach is to calculate  $\frac{\partial m_j}{\partial p_i}$  using finite element modelling or vector field solution.

Mutual impedance changes ( $\Delta Z$ ) between transmitter and receiver coils affected by an object is derived. Derivations in [61] and [62] expose some relations of source's and probe's change due to electromagnetic field modification. Lorentz reciprocity relation is considered and a generalised formula applies for coil pairs [63],

$$\begin{aligned} \Delta Z &= Z_b - Z_a \\ &= \frac{1}{I^2} \int_v j\omega(\mu_b - \mu_a) \mathbf{H}_a \cdot \mathbf{H}_b - (\sigma_b + j\omega\epsilon_b - \sigma_a - j\omega\epsilon_a) \mathbf{E}_a \cdot \mathbf{E}_b dv \end{aligned} \quad (2.10)$$

where  $Z_a$  is the mutual impedance between coil pairs when properties of the medium are  $(\mu_a, \sigma_a, \varepsilon_a)$ . One of the coils is excited by a current  $I$  with angular frequency  $\omega$  generating magnetic and electric fields  $\mathbf{H}_a$  and  $\mathbf{E}_a$  respectively.  $Z_b$  is the mutual impedance when properties of the medium are  $(\mu_b, \sigma_b, \varepsilon_b)$ . Identically, the other coil is excited by a current  $I$  with angular frequency  $\omega$  generating magnetic and electric fields  $\mathbf{H}_b$  and  $\mathbf{E}_b$  respectively. The region  $v$  covers the medium (and object) under inspection.

In the interest of observing only a conductive object, the permeability change is neglected. Furthermore, as the reference measurement is air background, both conductivity  $\sigma_a$  and permittivity  $\varepsilon_a$  are negligible as well. Thus, (2.10) is simplified,

$$\Delta Z = -\frac{1}{I^2} \int_v (\sigma_b + j\omega\varepsilon_b) \mathbf{E}_a \cdot \mathbf{E}_b dv \quad (2.11)$$

As an attempt to reduce the coupling capacitance between coils and object, the sensing system is designed in such a way that the electric field generated by coils is eliminated. Consequently, for background condition  $\nabla V \approx 0$ , the electric field becomes,

$$\mathbf{E}_a \approx -\frac{\partial \mathbf{A}_a}{\partial t} = -j\omega \mathbf{A}_a \quad (2.12)$$

whereas the current density in the object is,

$$\mathbf{J}_b = (\sigma_b + j\omega\varepsilon_b) \mathbf{E}_b \quad (2.13)$$

putting altogether (2.11), (2.12), and (2.13),

$$\begin{aligned} \Delta Z &\approx \frac{j\omega}{I^2} \int_v \mathbf{A}_a \cdot \mathbf{E}_b (\sigma_b + j\omega\varepsilon_b) dv \\ &= \frac{j\omega}{I^2} \int_v \mathbf{A}_a \cdot \mathbf{J}_b dv \end{aligned} \quad (2.14)$$

Therefore, an approximation for the system that observes complex conductivity changes related to the measurement of mutual impedance can be obtained as a discrete coefficient,

$$S = \frac{\Delta Z}{\Delta(\sigma + j\omega\varepsilon)} \quad (2.15)$$

Examples of sensitivity matrix derivation for some electromagnetic problems have been reported in [64] [65] [66] [67]. The general form of the sensitivity formula for excitation-detection pairs (e.g. coil-1 and coil-5 in Figure 2-2) is [68]

$$\int_{\Gamma} \delta \mathbf{E}_1 \times \mathbf{H}_5 \cdot \mathbf{n} ds = \int_{\Omega} -j\omega \delta \mu \mathbf{H}_1 \cdot \mathbf{H}_5 + (\delta \sigma + j\omega \delta \epsilon) \mathbf{E}_1 \cdot \mathbf{E}_5 dv \quad (2.16)$$

where the left-hand side represents excitation and detection by surface integral on surface  $\Gamma$ ; while the right-hand-side is the volume integral over the perturbed region  $\Omega$ . The magnetic and electric fields when sensor 1 is excited are  $\mathbf{H}_1$  and  $\mathbf{E}_1$ ; whereas  $\mathbf{H}_5$  and  $\mathbf{E}_5$  are the magnetic and electric fields when sensor 5 is excited. Therefore, a relationship between the change of detection voltage and conductivity change at eddy current region can be derived from the dot product of electric fields [69]. Here, the space  $\Omega$  is discretised onto elements in two-dimensional  $50 \times 50$  pixels along X and Y axes.

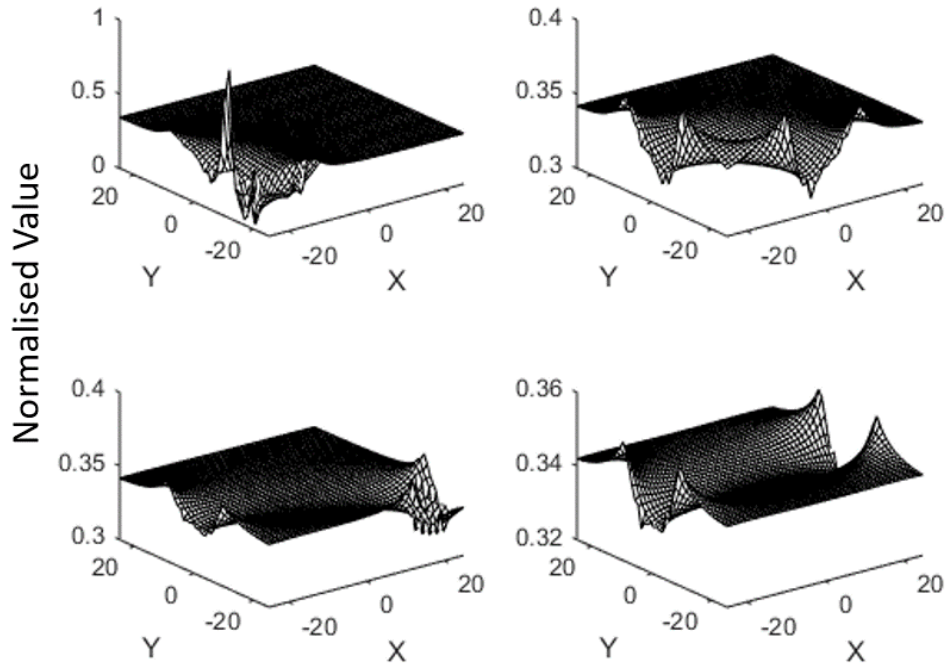


Figure 2-3: Sensitivity map.

Figure 2-3 illustrates a computed sensitivity map for coil pairs in adjacent (top-

left), orthogonal (top-right), near-opposite (bottom-left), and opposite (bottom-right) positions. These four maps are the basis that can be rotated to form a full combination sensitivity matrix. They are plotted relative to the adjacent map's value and reveals high-sensitive regions near the boundary. This will affect the reconstruction result.

The linear case has an inevitable limitation. Nevertheless, this method gives a rough qualitative image which indicates material distribution. The inversion determines  $\mathbf{P}$  from the measurement of  $\mathbf{M}$ . However, the sensitivity matrix  $\mathbf{S}$  cannot be inverted in an obvious fashion. The Moore-Penrose generalised inverse  $\mathbf{S}^\dagger$  may be chosen [60],

$$\mathbf{S}^\dagger = (\mathbf{S}^\mathbf{T} \cdot \mathbf{S})^{-1} \cdot \mathbf{S}^\mathbf{T} \quad (2.17)$$

where  $\mathbf{P} = \mathbf{S}^\dagger \mathbf{M}$  is least-square solution for  $\mathbf{M} = \mathbf{S} \mathbf{P}$ , i.e.  $\min \|\mathbf{M} - \mathbf{S} \cdot \mathbf{P}\|^2$ . Mostly, the applications demand a large number of  $k$  than the number of measurements  $n$ . This makes the problem ill-posed, and computation of  $(\mathbf{S}^\mathbf{T} \cdot \mathbf{S})^{-1}$  or  $(\mathbf{S} \cdot \mathbf{S}^\mathbf{T})^{-1}$  has a numerical error. Thus, regularisation is required to minimise least square error as well as penalise large value in  $\mathbf{P}$ ,

$$\min \{ \|\mathbf{M} - \mathbf{S} \cdot \mathbf{P}\|^2 + \alpha^2 \|\mathbf{P}\|^2 \} \quad (2.18)$$

$\alpha^2$  compromise between matching the data and controlling solution. The choice of  $\alpha^2$  represents the level of a priori knowledge related to the solution.

## 2.3 Contactless Inductive Flow Tomography

The CIFT reconstructs the velocity field of flowing conductive liquid [70]. The basis of this technique is the induction of secondary magnetic fields when a primary magnetic field exposes the flowing liquid. As a result, magnetic field perturbation outside the volume can be measured, and the inversion problem will determine the flow velocity. While MIT reconstructs conductivity distribution in a body through induced eddy current from AC magnetic field, CIFT utilises induced eddy current due to the interaction between a moving liquid with an applied DC (or very low frequency) magnetic field [71].

If a moving fluid with velocity  $\mathbf{v}$  is exposed to a stationary magnetic field  $\mathbf{B}$ , then

by using Ohm's law the current density will be induced [72],

$$\mathbf{J} = \sigma(\mathbf{v} \times \mathbf{B} - \nabla\phi) \quad (2.19)$$

where  $\sigma$  is the electrical conductivity of the fluid and  $\phi$  is the electric scalar potential. The current density  $\mathbf{J}$  will then in turn induce a secondary magnetic field  $\mathbf{b}$  at position  $\mathbf{r}$  which is defined by Biot-Savart's law:

$$\mathbf{b}(\mathbf{r}) = \frac{\mu_0\sigma}{4\pi} \iiint_V [\mathbf{v}(\mathbf{r}') \times \mathbf{B}(\mathbf{r}')] \times \frac{\mathbf{r} - \mathbf{r}'}{|\mathbf{r} - \mathbf{r}'|^3} dV' - \frac{\mu_0\sigma}{4\pi} \iint_S \phi(\mathbf{s}') \mathbf{n}(\mathbf{s}') \times \frac{(\mathbf{r} - \mathbf{s}')}{|\mathbf{r} - \mathbf{s}'|^3} dS' \quad (2.20)$$

here  $dV'$  is the volume element,  $\mathbf{r}'$  is the position vector in the volume,  $dS'$  is a surface element and  $\mathbf{n}(\mathbf{s}')$  is the normal vector of the surface at position  $\mathbf{s}'$ . Assuming insulating boundaries, with the divergence-free of  $\mathbf{J}$ , a Poisson equation for electric potential can be derived from (2.19). The solution fulfils the boundary integral equation according to Green's theorem.

$$\phi(\mathbf{s}) = \frac{1}{2\pi} \iiint_V [\mathbf{v}(\mathbf{r}') \times \mathbf{B}(\mathbf{r}')] \cdot \frac{\mathbf{s} - \mathbf{r}'}{|\mathbf{s} - \mathbf{r}'|^3} dV' - \frac{1}{2\pi} \iint_S \phi(\mathbf{s}') \mathbf{n}(\mathbf{s}') \cdot \frac{(\mathbf{s} - \mathbf{s}')}{|\mathbf{s} - \mathbf{s}'|^3} dS' \quad (2.21)$$

Generally, the total magnetic field  $\mathbf{B}$  is a sum of the primary magnetic field  $\mathbf{B}_0$  and the secondary magnetic field  $\mathbf{b}$ . The ratio between  $\mathbf{b}$  and  $\mathbf{B}_0$  follows the magnetic Reynolds number ( $R_m$ ). For industrial application, typically  $R_m$  is smaller than 1 so that  $\mathbf{B}$  can be replaced by  $\mathbf{B}_0$ . Therefore, this approximation leads to a linear inverse problem for determining the velocity field  $\mathbf{v}$  from the measurement of the induced magnetic field  $\mathbf{b}$  [73]. Figure 2-4 illustrates the principle and application of CIFT.

This technique has been implemented to observe fluid flow in a rectangular vessel in the physical model of continuous casting of steel slabs using a cold liquid metal [74]. The flow structure in the mould, where the steel starts to solidify, is an important factor that affects the product quality [75].

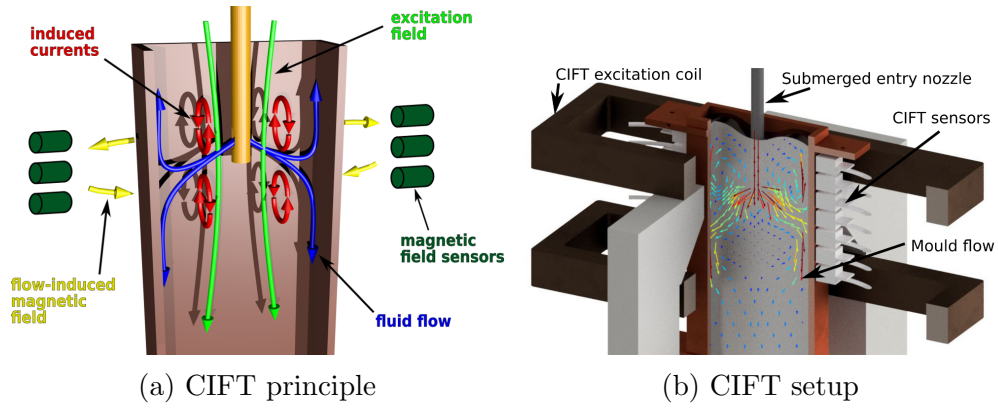


Figure 2-4: CIFT principle and setup in velocity field reconstruction (images from hzdr.de)

## 2.4 Application

The hydrodynamic measurement and visualisation of liquid metal inside nozzle and mould play an important role in improving the steel quality. Transferring liquid steel from tundish to the mould, the SEN contains and determines flow condition which affects the subsequent process. However, temperature and opacity hinder the conventional probe and/or optical measurement access. Examination of SEN flow pattern remains necessary [76].

While operational conditions in the continuous caster pose difficulties for studying liquid steel phenomena, physical models present feasible means to perform experimental practices. This kind of reduced geometry within the ambient temperature system is frequently used to represent fluid dynamic system [76]. The mini-LIMMCAST facility was constructed for the purpose of observing two-phase flow using cold liquid metal GaInSn and argon gas [77]. There is a need to sense the nozzle (imaging area in Figure 2-5) to obtain the two-phase distribution of liquid metal and gas while the system is running. The immediate goal is to handle clogging in the nozzle as well as maintain stable flow down in the mould by actuating the stopper rod and gas supply.

The injection of inert gas is an attempt to obtain clean steel. The resulting bubbles help in dealing with clogging and inclusion removal. On the other hand, the excessive amount of them is also threatening in the form of entrapment in solidified steel, hence the deteriorated product. Therefore, understanding the

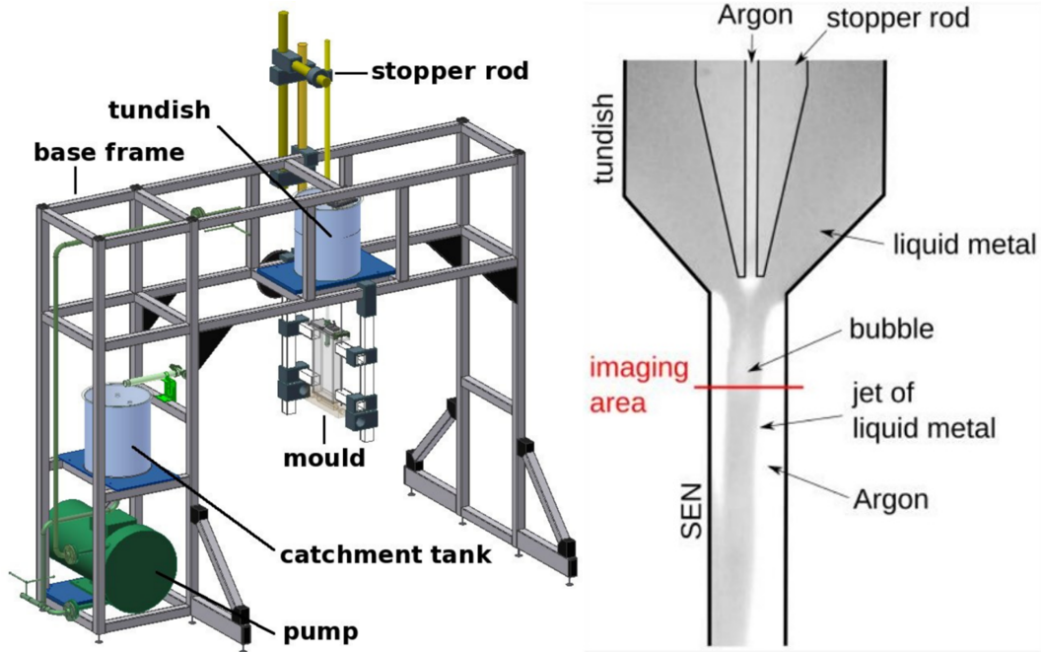


Figure 2-5: Mini-LIMMCAST construction at HZDR (figures from [77] and [2])

metal/gas regime in a bubbly flow might be influential for quality assurance by controlling the responsible process parameters such as metal and gas flow rates. Numerical simulation shows that argon gas bubbles injected from the inner wall of the tundish upper nozzle will initially go down along the wall due to the liquid steel action. Farther away from tundish, argon bubbles penetrate gradually to the nozzle's central region [78]. The measurement technique that is able to characterise those behaviours is essential [79].

Some experimental techniques for identifying two-phase liquid-gas flow patterns are reviewed [80]. Impedance (capacitance, conductance, wire-mesh) sensors, pressure fluctuation, photon attenuation, and ultrasonic are commonly used in a non-transparent process. Setting aside those which are intrusive and nuclear radiation methods, ECT, MIT, and CIFT are prospective.

In control perspective, fuzzy technique was used to recognise flow pattern [81], identify two-phase gas-liquid [82], and analyse tomographic data [83]. Information from multiple sensors also can be fused by using the fuzzy method, as described in [84]. Practically, fuzzy control has been implemented in continuous casting process [85], [86], and generally in iron-making [87].

Interpretation of the sensors' output, i.e. metal shape and gas fraction, can be quantified as linguistic variables required for fuzzy inference. Together with flow velocity data (either from ultrasonic doppler velocimetry –UDV– measurement in the nozzle or CIFT measurement in the mould investigated by [88]), they constitute important flow characteristics in deciding control action. Figure 2-6 depicts the simplified input-output scheme.

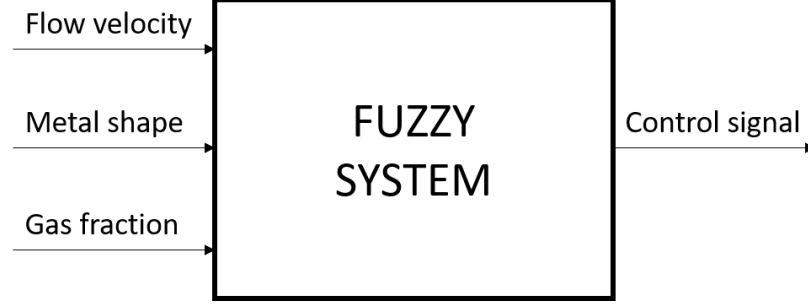


Figure 2-6: Input output control model

Generally, fuzzy rules composition can be described as [89],

$$R_i : \text{IF } x \text{ is } A \text{ and } y \text{ is } B, \text{ THEN } z \text{ is } C$$

where  $R_i$  is the  $i^{th}$  rule,  $x$  and  $y$  are controlled variables and  $z$  is control input.  $A$  and  $B$  are input subsets; whereas  $C$  is the output subset. For instance [90], fuzzy sets of the control output for stopper rod may be assigned as positive small (PS) and positive medium (PM) to describe an increase in position; negative small (NS) and negative medium (NM) to describe a decreasing position; also zero (ZR) to indicate no change.

The determination of parameters and knowledge base can be derived and tuned through experiments as well as experts' analysis in future work. The tomographic sensors designed and reinforced by experts involved in the framework [91] have been demonstrated in an industrial model to achieve the control objective for the continuous steel casting process.

## 2.5 Summary

The abovementioned techniques are reviewed in the interest of liquid metal flow measurement. Implementation prospect utilising the measurement methods is,



for instance, to control the flow in continuous casting model utilising data and/or image from electromagnetic tomography sensors. An expert-based inference system could be implemented to provide a control scheme to regulate the process.

## Chapter 3

# Magnetic Induction Tomography Spectroscopy

This chapter explains the basis of MIT and spectroscopy methods. Forward problem formulates field and eddy current due to given passive electromagnetic properties in the sensing space. Inverse problem attempts to resolve the object distribution or parameter from the boundary measurements. The hardware system is designed to conduct measurements for providing the necessary data.

### 3.1 Forward Problem

MIT utilizes an array of inductive coils, distributed equally around an imaging region, to visualize the electromagnetic property distribution of the electrical conductivity of an imaging subject. The imaging principle is based on the laws of induction and eddy currents which are induced in an AC magnetic field [92]. The formulation can be obtained from Maxwell's equations [59] [93], recalling (2.7) from the previous chapter:

$$\nabla \times \frac{1}{\mu} \nabla \times \mathbf{A} + j\omega\sigma\mathbf{A} = \mathbf{J}_s \quad (3.1)$$

Equation (3.1) can be solved by approximating the system as a combination of linear equations in small elements with appropriate boundary conditions using

the Galerkin's approximation [94]:

$$\int_{\Omega_C + \Omega_S} (\nabla \times \mathbf{N}_i \cdot \frac{1}{\mu} \nabla \times \mathbf{A}) dv + \int_{\Omega_C + \Omega_S} (j\omega\sigma \mathbf{N}_i \cdot \mathbf{A}) dv = \int_{\Omega_S} (\nabla \times \mathbf{N}_i \cdot \mathbf{T}_s) dv \quad (3.2)$$

where  $\mathbf{T}_s$  is the electric vector potential and  $\mathbf{J}_s = \nabla \times \mathbf{T}_s$ ,  $\mathbf{N}_i$  is the linear combination of edge shape functions, and  $\Omega_C$  and  $\Omega_S$  are eddy current region and current source region or excitation coil region, respectively.

The right-hand side of equation (3.2) can be solved with the aid of Biot-Savart Law. When  $\mathbf{J}_0$  is the unit current density passing through coil, the measured induced voltage in sensing coil can be calculated:

$$V_{mn} = -j\omega \int_{\Omega_S} (\mathbf{A} \cdot \mathbf{J}_0) dv \quad (3.3)$$

Then Jacobian matrix can be formulated by:

$$J = \frac{\delta V_{mn}}{\delta \sigma_x} = -\omega^2 \int_{\Omega_x} \frac{\mathbf{A}_m \cdot \mathbf{A}_n dv}{I} \quad (3.4)$$

where  $\sigma_x$  is the conductivity of pixel  $x$  and  $\Omega_x$  is the volume of the perturbation,  $\mathbf{A}_n$  is the forward solver of sensor coil excited by unit current,  $\mathbf{A}_m$  is the forward solver of excitation coil  $m$  excited with  $I$ . Amplitude and phase Jacobian are given

$$J_{amp} = \frac{V_r J_r - V_i J_i}{|V|} \quad (3.5)$$

$$J_{phs} = \frac{V_r J_i - V_i J_r}{|V|^2} \quad (3.6)$$

Where  $V_r$  and  $V_i$  are real and imaginary part of the measurement voltage. If one reconstructs real and imaginary part of the impedance, then real and imaginary part of  $J$  in equation (3.4) can be used. For forward modelling, the author used non-ferrous materials, which means relative permeability of 1, and conductivity

according to the metal sample.

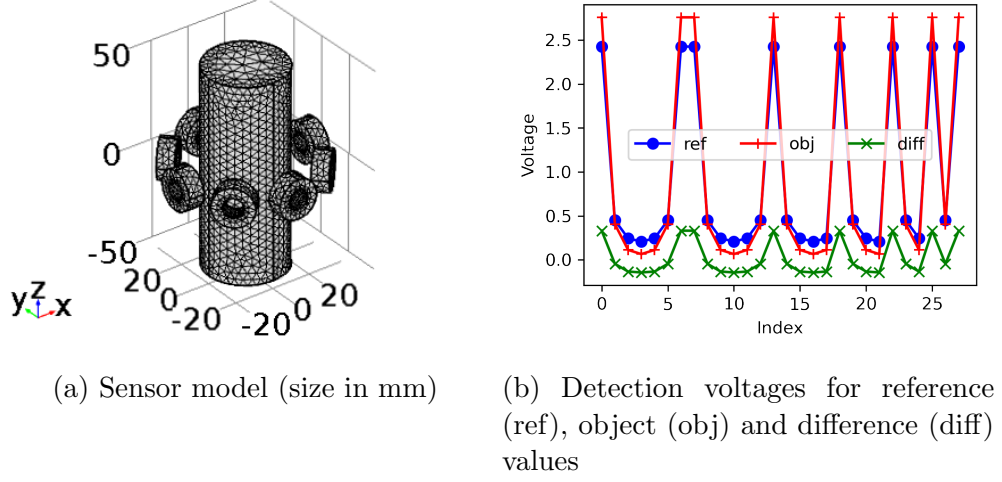


Figure 3-1: Sensor and signal modelling in COMSOL

Figure 3-1a shows sensor model in COMSOL using finite element method. There are non-conducting (outer region, sensing region) and conducting (coil, object) domains. The complete mesh consists of 93419 domain elements, 7702 boundary elements, and 1066 edge elements. Here, for clarity, only coil and object are shown. Then field computation is run in coil geometry and frequency domain analysis. Induced voltages from every coil pair are collected. Detailed in

Table 3.1: Measurement Index

	Rx						
	coil-2	coil-3	coil-4	coil-5	coil-6	coil-7	coil-8
coil-1	0	1	2	3	4	5	6
coil-2		7	8	9	10	11	12
coil-3			13	14	15	16	17
Tx coil-4				18	19	20	21
coil-5					22	23	24
coil-6						25	26
coil-7							27

Table 3.1, 8-coil transmitter-receiver (Tx-Rx) combination produces 28 data arrangement. The numbering can be referred from Figure 2-2. This corresponds to *index* in Figure 3-1b. The patterns here are the voltages for reference (air

background), object (metal) and the difference/change between object presence against a reference.

## 3.2 Inverse Problem

Algorithms for solving soft-field tomography, in general, have been studied extensively. The following briefly describes some methods which are used in the subsequent chapters. Applicability in liquid metal imaging is the main consideration for selecting these reconstruction techniques.

### 3.2.1 Tikhonov Method

It is assumed that the forward problem has a linear form,

$$\Delta \mathbf{V} = \mathbf{J} \Delta \sigma \quad (3.7)$$

For ensuring uniqueness and stability, a least square solution is applied [95].

$$\min \|\Delta \mathbf{V} - \mathbf{J} \Delta \sigma\|^2 = \min [(\Delta \mathbf{V} - \mathbf{J} \Delta \sigma)^T (\Delta \mathbf{V} - \mathbf{J} \Delta \sigma)] \quad (3.8)$$

$$\frac{\partial}{\partial \sigma} [(\Delta \mathbf{V} - \mathbf{J} \Delta \sigma)^T (\Delta \mathbf{V} - \mathbf{J} \Delta \sigma)] = -2 \mathbf{J}^T (\Delta \mathbf{V} - \mathbf{J} \Delta \sigma) \quad (3.9)$$

$$\Delta \sigma = (\mathbf{J}^T \mathbf{J})^{-1} \mathbf{J}^T (\Delta \mathbf{V}) \quad (3.10)$$

Further regularisation function shall be added for the accuracy and robustness of the solution. Therefore, the Tikhonov regularisation method can be used as the inverse solution to compute the conductivity distribution,

$$\Delta \sigma = (\mathbf{J}^T \mathbf{J} + \alpha \mathbf{R})^{-1} \mathbf{J}^T (\Delta \mathbf{V}) \quad (3.11)$$

where  $\mathbf{R}$  and  $\alpha$  are regularisation matrix and regularisation parameter, respectively.

### 3.2.2 Landweber Iteration Method

Assume that  $\hat{\mathbf{J}}_0$  is initial approximation of  $\mathbf{J}^{-1}$ , residual value of the inverse will be

$$\mathbf{R} = \mathbf{I} - \hat{\mathbf{J}}_0 \mathbf{J} \quad (3.12)$$

and

$$\mathbf{J}^{-1} = (\mathbf{I} - \mathbf{R})^{-1} \hat{\mathbf{J}}_0 \quad (3.13)$$

if both values are close, i.e.  $\hat{\mathbf{J}}_0 \approx \mathbf{J}^{-1}$ , spectral radius of  $\mathbf{R}$  is less than unity  $\rho(\mathbf{R}) < 1$ . Series expansion of  $(1 - \mathbf{R})^{-1}$  can be made with  $k_{th}$  approximation of the inverse is

$$\hat{\mathbf{J}}_k \equiv (\mathbf{I} + \mathbf{R}) + \cdots + \mathbf{R}^{k-1} \hat{\mathbf{J}}_0 \quad (3.14)$$

Note that

$$(\mathbf{I} - \mathbf{R})(1 + \mathbf{R} + \cdots + \mathbf{R}^{k-1}) = \mathbf{I} - \mathbf{R}^k \quad (3.15)$$

arranging (3.12) using (3.14) dan (3.15) results in

$$\mathbf{R}_k \hat{\mathbf{J}}_0 = \hat{\mathbf{J}}_0 (\mathbf{I} - \mathbf{J} \hat{\mathbf{J}}_k) \quad (3.16)$$

For  $(k+1)_{th}$  approximation inverse of  $\mathbf{J}_{k+1}$ , image is given as

$$\hat{\mathbf{K}}_{k+1} = \hat{\mathbf{J}}_{k+1} \mathbf{V} \quad (3.17)$$

expanding (3.17) using (3.14)

$$\hat{\mathbf{K}}_{k+1} = \hat{\mathbf{K}}_k + \mathbf{R}^k \hat{\mathbf{J}}_0 \mathbf{V} \quad (3.18)$$

substituting (3.16) to (3.18), taking  $\hat{\mathbf{J}}_k \mathbf{V} = \hat{\mathbf{K}}_k$

$$\hat{\mathbf{K}}_{k+1} = \hat{\mathbf{K}}_k + \hat{\mathbf{J}}_0 (\mathbf{V} - \mathbf{J} \hat{\mathbf{K}}_k) \quad (3.19)$$

Landweber method estimates  $\hat{\mathbf{J}}_0$  by transpose of  $\mathbf{J}$  with gain factor  $\alpha$  for controlling convergence rate, hence

$$\hat{\mathbf{K}}_{k+1} = \hat{\mathbf{K}}_k + \alpha \mathbf{J}^T (\mathbf{V} - \mathbf{J} \hat{\mathbf{K}}_k) \quad (3.20)$$

a suitable convergence criterion is  $\|\alpha \mathbf{J}^T \mathbf{J}\|_2 < 2$  so that  $\alpha$  can be estimated into  $2/\lambda$  where  $\lambda$  is the maximum eigenvalue of  $\mathbf{J}^T \mathbf{J}$  [96].

### 3.2.3 Spatio-Spectral Total Variation

The linear inverse problem can be defined as the recovery of a change in complex conductivity  $\Delta\sigma$  from a change in measured data  $\Delta u$ , where  $\Delta u = J\Delta\sigma$ . The Jacobian  $J$  is computed by the Fréchet derivative of  $u$  with respect to  $\sigma$  [97]. The complex conductivity includes the resistive component and reactive component of the admittivity of the samples under test. In this case, a reference boundary voltage  $u_0$  is available, where  $u_0 = F(\sigma_0)$ ,  $\Delta u = u - u_0$ , and  $\Delta\sigma = \sigma - \sigma_0$ . Measured data in this case is real and imaginary part of mutual inductance, or amplitude and phase of the mutual inductance.

In spectral imaging, the unknown conductivity changes and data are multidimensional. Let's redefine  $\Delta\sigma = [\Delta\sigma_1, \dots, \Delta\sigma_I]$  and data  $\Delta\mathbf{u} = [\Delta u_1, \dots, \Delta u_I]$ , where  $\Delta\mathbf{u} = \tilde{\mathbf{J}}\Delta\sigma$ , for  $i = 1, \dots, I$ , and  $I$  is the number of spectral frames. It is common to recover each frame independently, but this is not optimal, as it does not exploit redundant information across frames. In this case, previous works have defined the inverse problem as follows [98]:

$$\underset{\Delta\sigma_i}{\operatorname{argmin}} \phi(\Delta\sigma_i) \text{ s.t. } \|J\Delta\sigma_i - \Delta u_i\|_2^2 \leq \delta, \forall i = 1, \dots, I \quad (3.21)$$

where  $\phi(\Delta\sigma_i)$  is a convex regularization functional that carries a priori information of the unknown conductivity distribution for a single frame.

This work proposes a spatio-spectral reconstruction framework that exploits regularization [99]. Spatio-spectral total variation (TV) is implemented as MIT images can be well approximated by a piecewise constant function and consecutive frames are expected to be similar. This allows to exploit redundant information across consecutive frames. The spatio-spectral total variation problem can be written as follows [100] [101]:

$$\underset{\Delta\sigma}{\operatorname{argmin}} \|\nabla_{x,y,z}\Delta\sigma\|_1 + \|\nabla_f\Delta\sigma\|_1 \text{ s.t. } \|\tilde{J}\Delta\sigma - \Delta u\|_2^2 \leq \delta \quad (3.22)$$

where first and second terms correspond to isotropic spatial TV and spectral TV functional, respectively, and where  $\Delta\sigma$  represents a spectrally correlated conductivity distribution and  $\tilde{J}$  is an augmented Jacobian operating on a frame-by-frame basis.

The constrained optimization problem (3.21) can be solved using the split Bregman formulation, which efficiently handled constrained optimization and L1-regularization [102] [103]. Using the Bregman iteration, the constrained problem (3.21) is converted to an iterative scheme:

$$\Delta\sigma^{k+1} = \underset{\Delta\sigma}{\operatorname{argmin}} \|\nabla_{x,y,z}\Delta\sigma\|_1 + \|\nabla_f\Delta\sigma\|_1 + \sum_{i=1}^I \frac{\mu}{2} \|\tilde{J}\Delta\sigma - \Delta u^k\|_2^2 \quad (3.23)$$

$$\Delta u^{k+1} = \Delta u^k - \tilde{J}\Delta\sigma^{k+1} + \Delta u \quad (3.24)$$

where (3.22) is an unconstrained optimization problem and (3.23) is a Bregman iteration that imposes the constraint iteratively. The cost function in (3.22) is still hard to minimize given the non-differentiability of the TV functional, but this can be easily done with a splitting technique. Including auxiliary variables allow splitting L1- and L2-functional in such a way that they can be solved in separate steps in an easy manner. Images  $\Delta\sigma$  are given analytically by solving a linear system and L1-functional are solved using shrinkage formulae. To perform the split, one can include  $d_x = \nabla_x$ ,  $d_y = \nabla_y$ ,  $d_z = \nabla_z$ ,  $d_f = \nabla_f$ , so equation (3.22) becomes

$$\begin{aligned} (\Delta\sigma^{k+1}, d_x, d_y, d_z, d_f) = & \underset{\Delta\sigma, d_x, d_y, d_z, d_f}{\operatorname{argmin}} \|(d_x, d_y, d_z)\|_1 + \|d_f\|_1 \\ & + \frac{\mu}{2} \|\tilde{J}\Delta\sigma - \Delta u^k\|_2^2 \text{ s.t. } d_i = \nabla_i \Delta\sigma \end{aligned} \quad (3.25)$$

Constraints in equation (3.24) can be handled using the Bregman iteration as above, which leads to the following iterative scheme



$$(\mu \tilde{J}^T \tilde{J} + \lambda \sum_{i=x,y,z,f} \nabla_i^T \nabla_i) \Delta \sigma^{k+1} = \mu \tilde{J}^T \Delta u^k + \lambda \sum_{i=x,y,z,f} \nabla_i^T (b_i^k - d_i^k) \quad (3.26)$$

$$d_i^{k+1} = \max(p^k - \frac{1}{\lambda}, 0) \frac{\nabla_i \Delta \sigma^{k+1} + b_i^k}{p^k}, \text{ for } i = x, y, z \quad (3.27)$$

$$p^k = \sqrt{\sum_{i=x,y,z} |\nabla_i \Delta \sigma^{k+1} + b_i^k|^2} \quad (3.28)$$

$$d_f^{k+1} = \max(|\nabla_f \Delta \sigma^{k+1} + b_f^k| - \frac{1}{\lambda}, 0) \frac{\nabla_f \Delta \sigma^{k+1} + b_f^k}{|\nabla_f \Delta \sigma^{k+1} + b_f^k|} \quad (3.29)$$

$$b_i^{k+1} = b_i^k + \nabla_i \Delta \sigma^{k+1} - d_i^{k+1}, \text{ for } i = x, y, x, f \quad (3.30)$$

$$\Delta u^{k+1} = \Delta u^k + \Delta u - \tilde{J} \Delta \sigma^{k+1} \quad (3.31)$$

Equation (3.25) is a linear system that can be solved efficiently using a Krylov solver [100] [101], [104], such as the bi-conjugate gradient stabilized method (BiCGStab) [105], which involves only matrix-vector multiplications. Number of Bregman iteration and other imaging parameters are selected empirically. Using known object size and shape, reconstruction is run initially with presumed regularisation parameters. Then parameters are adjusted so that the reconstructed image closely matches the known size and shape. These chosen parameters will be used for subsequent reconstructions with similar problems.

### 3.2.4 Neural Network

As an alternative to providing the desired interpretation, the neural network (NN) can be employed for processing forward/measurement data. Figure 3-2 shows neural network pipeline. For dense layer, where each input feature is assigned a

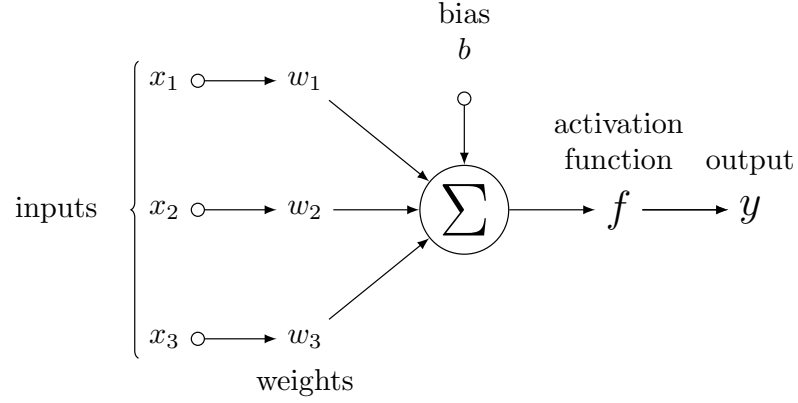


Figure 3-2: Neural network pipeline.

vector of weights that connects to activation output, this operation applies [106]:

$$z^i = W^i x + b^i \quad (3.32)$$

$$y^i = f^i(z^i) \quad (3.33)$$

here,  $W^i$  and  $b^i$  are weights and biases at  $i$ th layer respectively. The layer's input is  $x$ , and the resulting linear activation  $z^i$  is transformed by a non-linear activation function  $f^i$ . There are various activation functions such as sigmoid or hyperbolic tangent. In order to start with the approach based on experimental sensing data, the relatively simpler and faster Rectified Linear Unit (ReLU) will be used.

$$f(z) = \max(0, z) \quad (3.34)$$

On the other hand, Figure 3-3 illustrates convolutional neural network (CNN) which conducts (3.35):

$$z_n^i = K_n^i * x + b_n^i \quad (3.35)$$

where  $n$  is the index of the feature map,  $K_n^i$  is the  $n$ th filter kernel, and  $*$  is the convolution operator. In order to reduce the computation cost, the CNN layer is usually accompanied by a pooling layer for sub-sampling the feature map. Max operation finds the maximum value. For a classification problem, fully-connected layers are put in the last stages. The output layer then produces the decision.

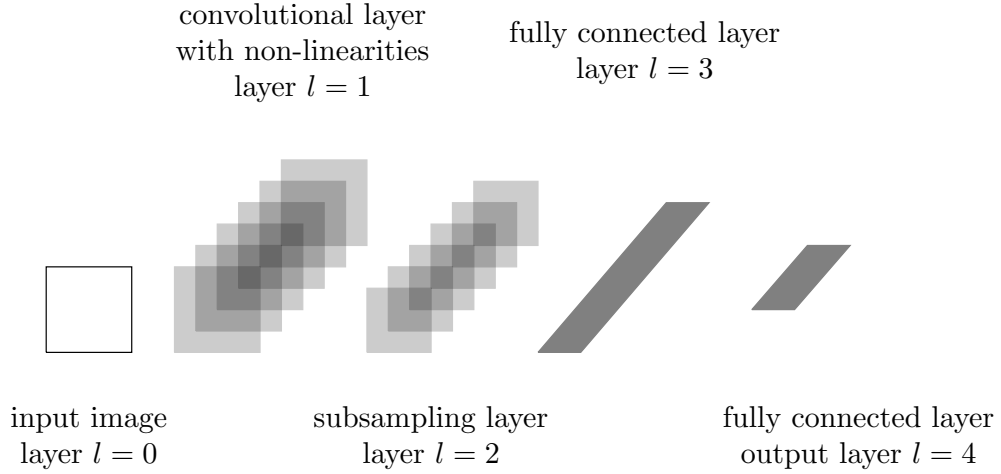


Figure 3-3: Convolutional neural network concept.

### 3.3 Measurement System

The hardware task is to enable field measurement in the sensing area. In the case of the coil sensor, mutual coupling between excitation and detection pairs is observed. Quantities of interest are the injection current and the induced voltage. A multiplexer is required to perform selective switching to virtually rotate the mutual induction of the multi-channel sensor arrays. Signal generation, switch control, and signal acquisition are the common functionalities of the tomographic measurement system.

Hardware for an MIT system have been designed in various configuration depending on the intended application. Few recent reports disclose a detailed specification. Due to relatively small signal level in receiver coils, typically gain requirement in this stage is 0–40 dB. It is common to employ ADC resolution between 14 and 16 bit. Generally the signal processing exploits oversampling of transmitter waveform to increase SNR [60]. Programmable device such as field-programmable gate-array (FPGA) is preferred for a customized hardware-level performance. Digital processing in the FPGA was reported to deliver data at 200 frames/s [107]. For low-frequency (0.1 Hz to 500 kHz) high-contrast imaging, one example of advancement in the MIT system yields 131 frames/s with a typical signal-to-noise ratio of 66 dB–95 dB [108]. Meanwhile for high-frequency (1 MHz–10 MHz) low-contrast imaging, a modular MIT system was designed with phase

demodulation error 0.0068 deg (RMSE), frequency stability  $\pm 0.1$  ppm, 6 s/frame at 16-channel, and SNR demodulation signal over 60 dB [109].

### 3.3.1 Magnitude-Based Hardware

The hardware block diagram of the MIT system based on magnitude detection at a given measurement cycle is shown in Figure 3-4

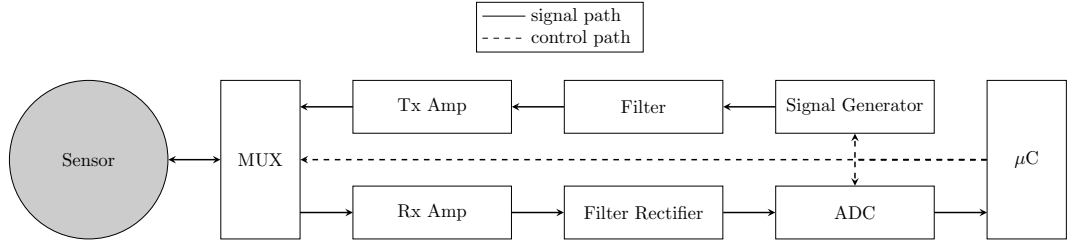


Figure 3-4: Magnitude-based hardware block diagram.

This system consists of transmitting and receiving lines. At the transmitting line, there are a signal generator (filtered), a current transmitter, and a multiplexer. At the receiving line, there are a multiplexer, a coil amplifier, gain stages, an absolute detector, filters, and analog-to-digital converters (ADC). A microcontroller is functioned to control signal generation, switching, ADCs, and process the measurement data. All circuits are built using commercial off the shelf components.

The signal generator produces a sine waveform with a fixed frequency at a given cycle. This is accomplished by using the direct digital synthesis (DDS) method [107]. The signal form is defined digitally, and the frequency is set according to phase and counter relative to the main clocking crystal oscillator. Waveform and frequency settings are instructed by the microcontroller.

The output of the signal generator has a suitable waveform, but inadequate voltage and current level for exciting the coil. Therefore, a subsequent current driver is placed. Additionally, DC offset has to be removed using a coupling capacitor. The current driver is constructed from voltage-controlled current-source (VCCS) topology [110] using an operational amplifier (Op-Amp) with a buffer in

the feedback line to get a precision output. A booster amplifier is added to produce a sufficient current level up to 100 mA for injecting the coils. Moreover, the configuration is also tailored to support the required operating frequency range.

The signal is then passed to the common port of the multiplexer. Each coil (eight in total) is connected to the 'drain' ports of the multiplexer. In this way, the excitation coil can be selected by closing the internal switch (through control ports), thus the current from the driver is injected into the selected coil. A similar manner applies to the other multiplexer in the receiving line. All eight channels are connected to both transmitting and receiving multiplexer ports accordingly. By contrast, when closing the receiving switch, the signal from the measuring coil is fed into circuits in the receiving line. For instance, coil-1 as a transmitter and coil-2 as a receiver, transmit multiplexer is controlled so that switching channel-1 is closed, while receive multiplexer channel-2 is closed (the remaining channels are open). It should be taken into consideration that the multiplexer shall have a sufficient signal range to accommodate both excitation current and detection voltage from the coil arrays.

On the other hand, the first analogue stage in the receiving line is a coil amplifier. It is usually configured as an instrumentation amplifier. The consideration here is that the measurement voltage is significantly low and suffering from an offset and/or drift, hence differential topology and high gain level are necessary. Moreover, the bandwidth should cover the operating frequency range for the MIT system.

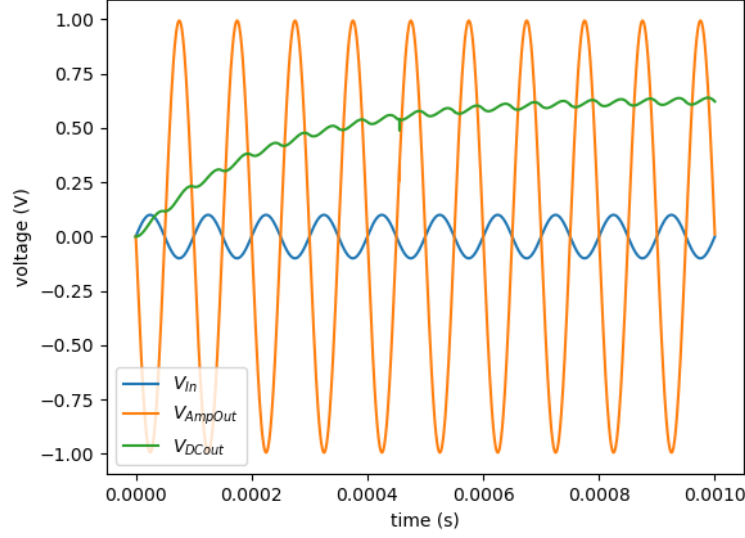


Figure 3-5: Simulation of analogue receiver circuits.

Following these gain stages, an absolute detection circuit is implemented so that the low-speed ADCs can handle the input. The peak detection is established using a precision rectifier based on Op-Amp [111], with an additional smoothing filter. However, this poses typical problems such as settling-time and attenuation and should be anticipated in processing the acquired signal. Figure 3-5 show the transient SPICE simulation of essential circuits on the receiving line. It can be seen that the input voltage  $V_{in}$  is amplified ten times to give  $V_{AmpOut}$ , and then the rectifier samples the signal amplitude into DC after 0.5 ms of settling time.

The abovementioned measurement schemes are repeated to do the coil combination cycles for complete tomographic sensing data. All digitised signals converted by ADCs are then fed into the microcontroller and saved in the buffer software. The interfacing between microcontroller and computer is established using a USB serial module.

### 3.3.2 Hardware System for Spectroscopy

Multi-frequency measurement is conducted using an impedance bridge system. Here, commercial benchtop E4980AL Precision LCR Meter (20 Hz – 300 kHz)

from Keysight Technologies is configured for mutual inductance measurement. Four ports, namely  $H_C$  (high current),  $H_P$  (high potential),  $L_C$  (low current), and  $L_P$  (low potential) are connected using custom-made test-fixture. In order to measure mutual inductance between two coils,  $H_C$  and  $L_C$  are connected to the transmitter coil, whereas  $H_P$  and  $L_P$  are connected to the receiver coil. Both  $L_C$  and  $L_P$  are shorted as a common reference. Another useful port from the LCR meter is the ground casing which can be connected with an outer shielding plate around the MIT sensors.

The main measurand of the LCR bridge is the amplitude value of impedance  $Z$  and its phase  $\theta$ , from which the other parameters are derived. Therefore, the use of this measurement method will mainly be the impedance-phase data that relates to mutual inductance between coil. Here, the calibration procedure is crucial for the accuracy of impedance and phase reading. Short calibration is used to eliminate the cabling effect; whereas open calibration is used to eliminate parasitic capacitance.

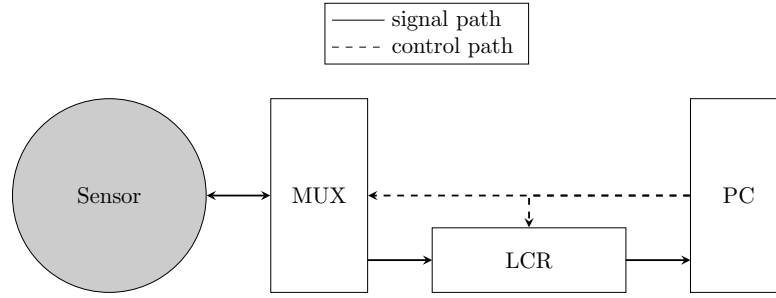


Figure 3-6: Spectroscopy hardware block diagram.

In order to conduct a multi-channel measurement (as in 3.3.1), an additional switching module is required. The manufacturer provides data acquisition (DAQ-970A Data Acquisition System) and multiplexer (DAQ-M901A 20 Channel Multiplexer Module) to combine with the LCR system. Figure 3-6 shows the setup where all instruments are synchronised and controlled by a computer (PC) using Standard Commands for Programmable Instruments (SCPI). In this way, a MATLAB script that acquires multi-channel measurement data can be incorporated into an existing post-processing program.

### 3.3.3 Complex-Valued Hardware

The third system is complex-valued measurement. This hardware is designed to extract amplitude, phase, real, and imaginary components from the sensing signals. The features are necessary for complex analysis and reconstruction.

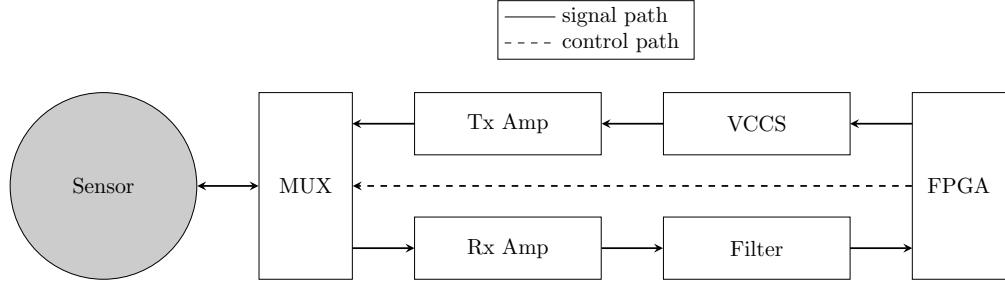
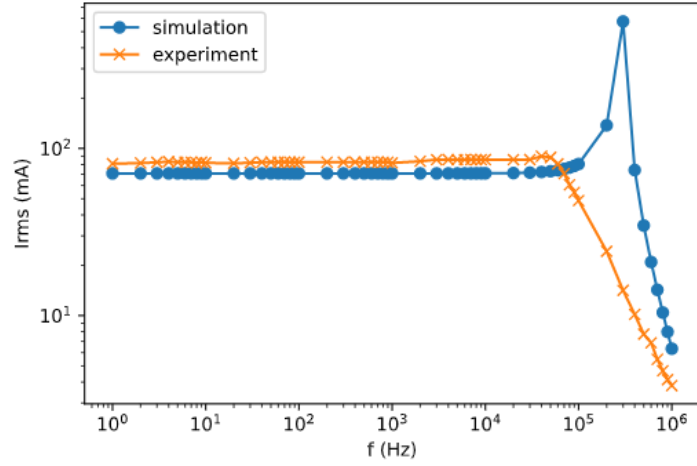


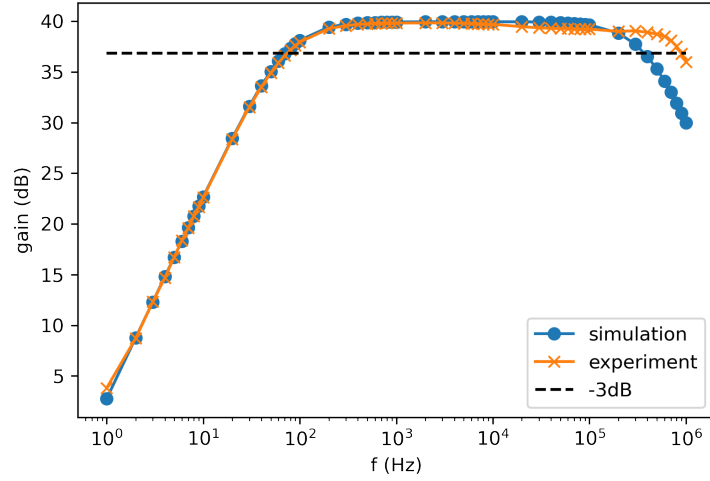
Figure 3-7: Complex-valued hardware block diagram.

Figure 3-7 shows the diagram of complex-valued hardware. The key difference is in the use of an embedded system based on an FPGA. The module has the capability of generating both source and reference signals to conduct a synchronous detection. Additionally, ADCs are integrated with a high sampling rate for direct full-wave acquisition. The module also controls the multiplexer through digital input-output (DIO) ports. A transmission control protocol (TCP) connection is established between the module and a computer for sending and receiving commands and data through ethernet.





(a) Current transmitter response



(b) Receiver circuit response

Figure 3-8: Characteristics of transmitter and receiver circuits

At the transmitter, a VCCS convert the source's sine-wave voltage into ac current. Since the module can only generate a sine-wave with a maximum amplitude of  $\pm 1$  V, a subsequent current buffer should be added. This buffer provides a boost for current to be injected into low-impedance loads such as coils. The current transmitter response from both simulation (SPICE) and test with a coil load is plotted in Figure 3-8a. In the simulation, a coil is represented as a pure inductor SPICE model. The discrepancy between the actual coil and simulated coil causes some differences in the graphs. Moreover, low-level lump model overlooks details

such as ESR and parasitics. The spike in the simulation graph might occurs due to those reasons.

On the other hand, the receiver part consists of an instrumentation amplifier for detecting an induced voltage on the coil. Besides gain function, the instrumentation amplifier also has a DC cancellation to reject an offset that may occur from the receiving signal. The stage is followed by passive filters that suppress signals below set lower cut-off (100 Hz) and upper cut-off (100 kHz) frequencies. This characteristic is shown in Figure 3-8b.

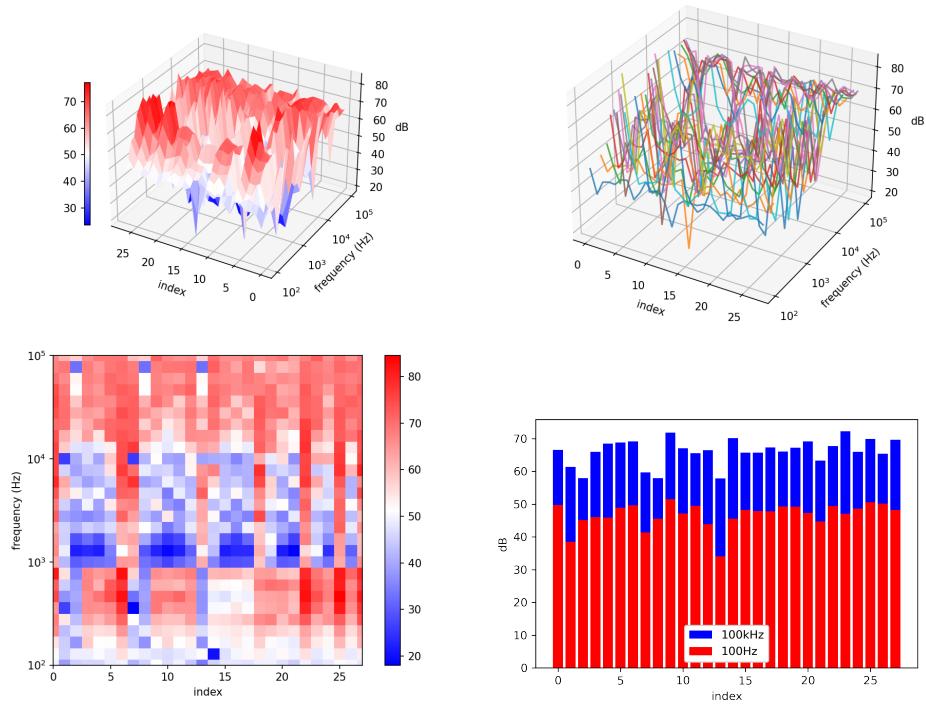
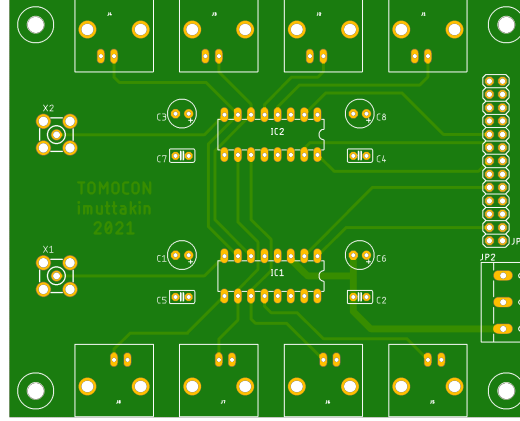


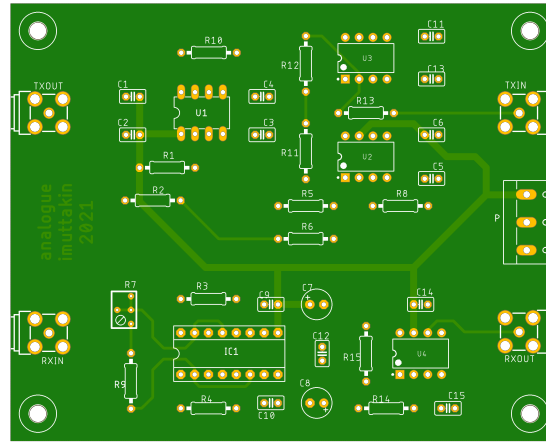
Figure 3-9: Measurement SNR (various views)

For 8-coil arrays arranged in circular, the measurement signal-to-noise ratio (SNR) is plotted in Figure 3-9. On the horizontal axis is the measurement index where  $index = 0$  is induced voltage at coil-2 due to the magnetic field generated by current injection at coil-1. The measurement  $index = 1$  is mutual between coil-1 and coil-3, and so on until  $index = 27$  which represents coil-7 and coil-8 pairing. It can be seen that the adjacent pair has the highest SNR, and the opposite pair has the lowest value. In addition, the number of signal samples also affect the SNR. The digital signal processor module has hardwired setting where

different input signal frequency will have different sample size. This is one of the reasons that causes relatively lower SNR in some operating frequencies.



(a) Multiplexer PCB



(b) Analogue PCB

Figure 3-10: Multiplexer and analogue circuit boards

Two PCBs are designed and manufactured as seen in Figure 3-10. The multiplexer is assembled in a dedicated PCB along with BNC ports for connection with the sensors and SMA ports for connection with the Tx and Rx channels. The other board is for the analogue parts containing both Tx and Rx circuits.

The Tx channel takes an input of the source signal from the embedded module, then produces an excitation current as an output. Meanwhile, the Rx channel gets a detection voltage and provides the conditioned signal as output.

The signal generation, switching control, and signal acquisition is dictated by a Python script through SCPI. This software on the PC sets the frequency operation and the number of the measurement cycle. Once the measurement is completed, the program will perform demodulation and arrange the data accordingly. As a result, amplitude, phase, real, and imaginary components are obtained for all measurement indexes.

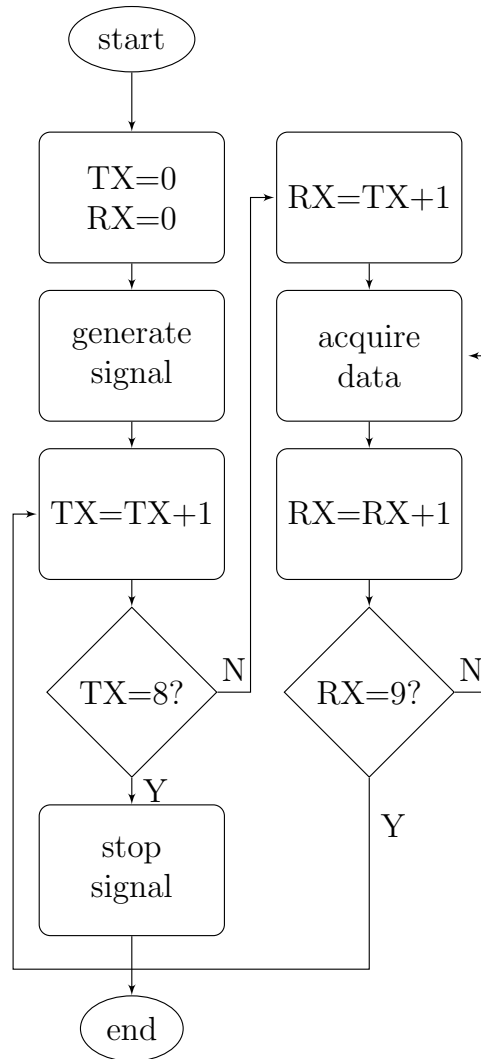


Figure 3-11: Hardware control flowchart.

Figure 3-11 shows the hardware control routine. At the start, multiplexers are disabled ( $Tx=0$  and  $Rx=0$ ) so that all switches are off. Then, the FPGA generates a waveform for both source and reference. This involves triggering two DDS channels to produce synchronous waveforms. Control signals are sent to switch on the first combination of transmitter-receiver channels. In the 8-coil sensors system, the first combination is  $Tx=1$  and  $Rx=2$ ; whereas the last combination is  $Tx=7$  and  $Rx=8$ . The source signal goes through the multiplexer and analogue circuitry to excite the selected transmitter coil. Consequently, at the selected receiver coil an induced signal occurs. This induced voltage is then passed into the multiplexer and conditioned by the analogue receiver before being retrieved by the embedded FPGA. In this acquisition process, a synchronous demodulation (or lock-in detection) is applied with the help of the other generated reference signal.

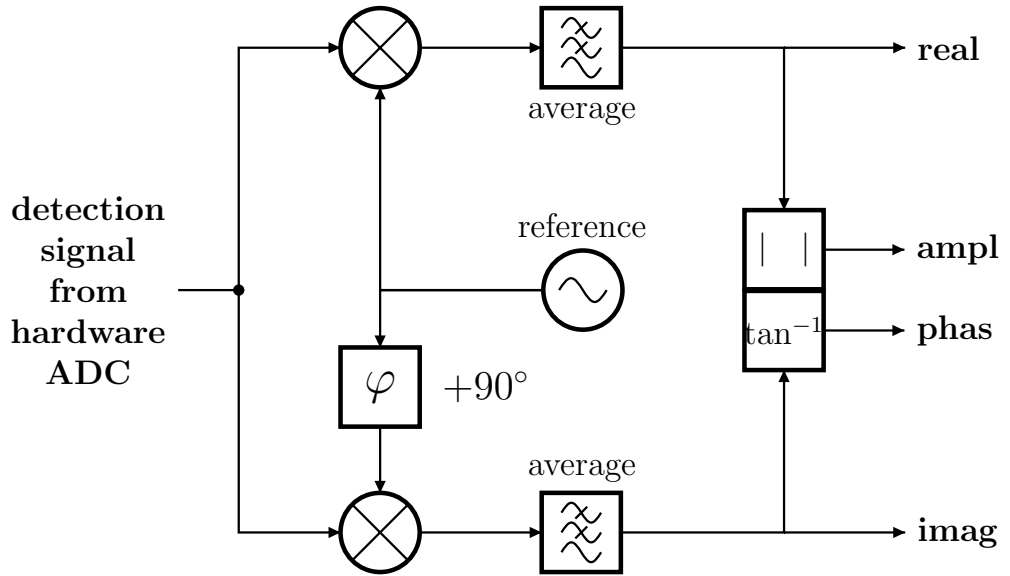


Figure 3-12: Block diagram of demodulation scheme implemented on the software

The lock-in detection follows the mechanism depicted in Figure 3-12. This scheme occurs on software parts. A reference signal  $V_{ref}$  with angular frequency  $\omega$ , amplitude  $A_{ref}$  and phase  $\theta_{ref}$  can be defined as,

$$V_{ref} = A_{ref} \sin(\omega t + \theta_{ref}) \quad (3.36)$$

whereas in the detected signal  $V_{det}$  with the same angular frequency  $\omega$ , its amplitude  $A_{det}$  and phase  $\theta_{det}$  are,

$$V_{det} = A_{det} \sin(\omega t + \theta_{det}) \quad (3.37)$$

If the detected signal (3.37) is multiplied by (3.36), the resulting wave will be,

$$V_{inp} = \frac{1}{2} A_{det} A_{ref} \cos(\theta_{det} - \theta_{ref}) - \frac{1}{2} A_{det} A_{ref} \cos(2\omega t + \theta_{det} + \theta_{ref}) \quad (3.38)$$

where  $V_{inp}$  is the obtained signal product. Passing it through a low-pass filter, it becomes

$$V_{inp} = \frac{1}{2} A_{det} A_{ref} \cos(\theta_{det} - \theta_{ref}) \quad (3.39)$$

which is a DC value proportional to both reference and detected signals. Here, the in-phase component is obtained.

In order to extract the phase difference between the reference and the detected signals, a shifted version of the reference signal is generated.

$$V_{ref} = A_{ref} \sin(\omega t + \theta_{ref} + 90^\circ) \quad (3.40)$$

Multiplying this shifted-reference with the detected signal and applying a filter to reject high-frequency components, one will have

$$\begin{aligned} V_{qdr} &= \frac{1}{2} A_{det} A_{ref} \cos(\theta_{det} - \theta_{ref} - 90^\circ) - \frac{1}{2} A_{det} A_{ref} \cos(2\omega t + \theta_{det} + \theta_{ref} + 90^\circ) \\ V_{qdr}[filtered] &= \frac{1}{2} A_{det} A_{ref} \sin(\theta_{det} - \theta_{ref}) \end{aligned} \quad (3.41)$$

The reference's signal amplitude and phase can be preset by the DDS to be  $A_{ref} = 1$  and  $\theta_{ref} = 0$ . It gives,

$$\begin{aligned} V_{inp} &= \frac{1}{2} A_{det} \cos(\theta_{det}) \\ V_{qdr} &= \frac{1}{2} A_{det} \sin(\theta_{det}) \end{aligned} \quad (3.42)$$

where  $V_{inp}$  and  $V_{qdr}$  are in-phase and quadrature components of the (filtered)

detected signal, respectively. Both magnitude  $R$  and phase  $\theta$  of the signal phasor can be calculated.

$$\begin{aligned} R &= \sqrt{V_{inp}^2 + V_{qdr}^2} \\ \theta &= \tan^{-1} \left( \frac{V_{qdr}}{V_{inp}} \right) \end{aligned} \quad (3.43)$$

This recovers the detected signal's amplitude  $A_{det} = 2R$  and phase  $\theta_{det} = \theta$ . Additionally, real part  $re(V_{det}) = V_{inp}$  and imaginary part  $im(V_{det}) = V_{qdr}$  can be directly inferred. Figure 3-13 depicts stages in the signal demodulation for opposite coil pairs at 10 kHz.

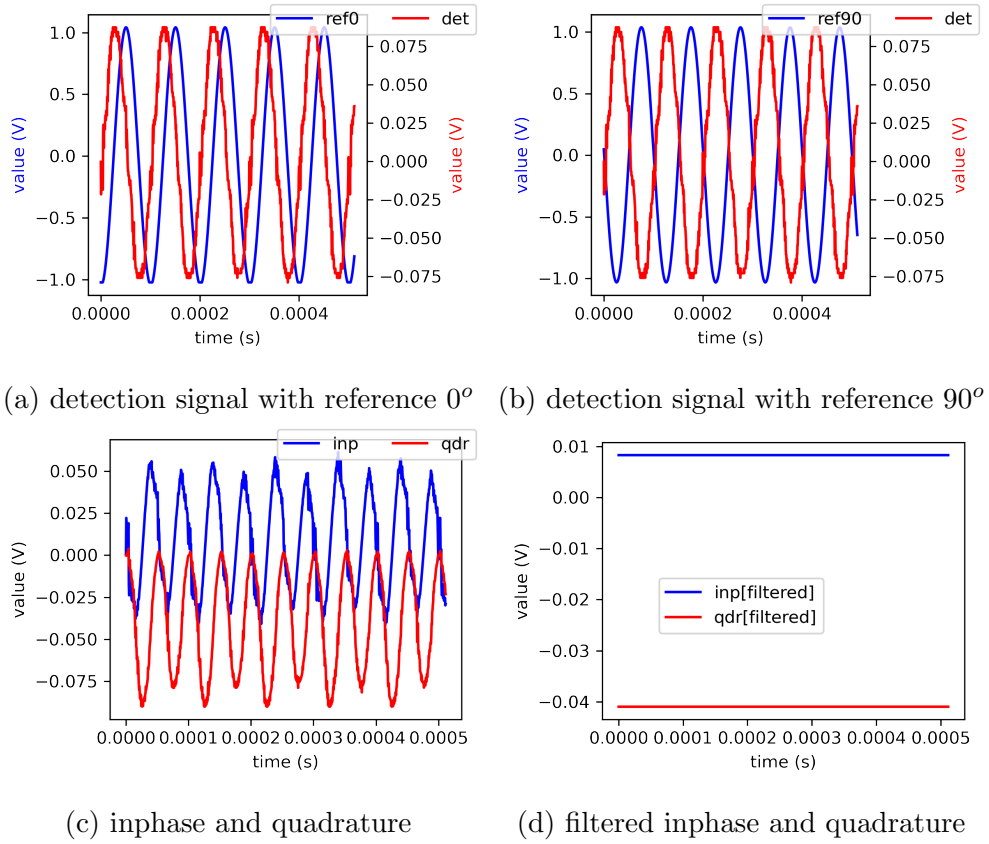


Figure 3-13: Signal demodulation

The demodulation is performed digitally in software after all the detection-sensors' raw-signals are acquired. Table 3.2 shows the timing details for hardware operation. In the beginning, the hardware needs initiation to set measurement parameters such as frequency, number of frames, etc. Another process that should

Table 3.2: Hardware Timing

Process	One Instance	Full Frame
Initiation		2.83 ms
Switching	0.57 ms	15.95 ms
Acquisition	48.86 ms	1368.08 ms
Demodulation		155.78 ms
Reconstruction		14.39 ms
	Total	1557.04 ms

be considered is channel switching. It controls multiplexing between transmitting and receiving and consumes delay to ensure the settling time of analog switches. The acquisition time comprises the generation of synchronous source-reference signals and full-wave sampling of both reference and detection signals. This takes the longest time in order to reserve a buffer window for capturing wave periods at the lowest operating frequency. The timing for digital demodulation along with data arrangement is also taken into account. The last process is reconstruction, which in this timing example, the Landweber algorithm with 100 iterations is executed.

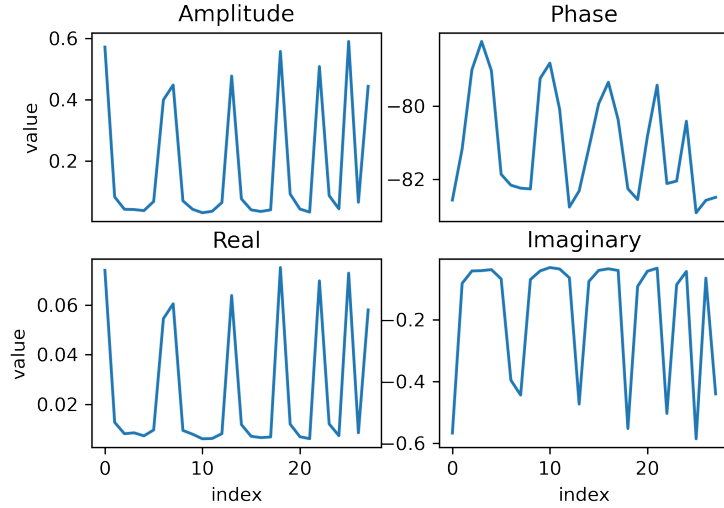
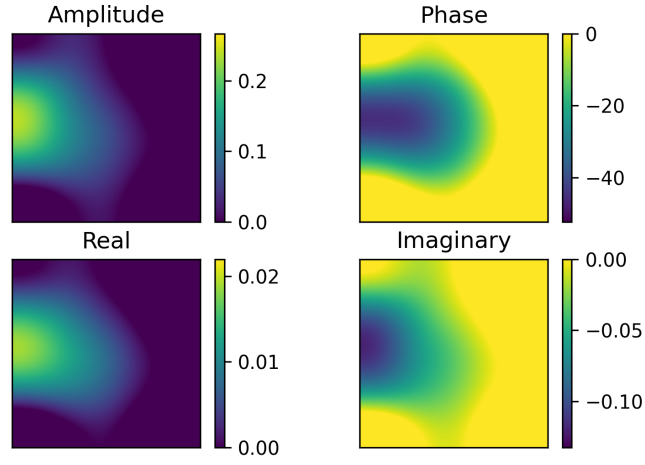


Figure 3-14: Measurement data

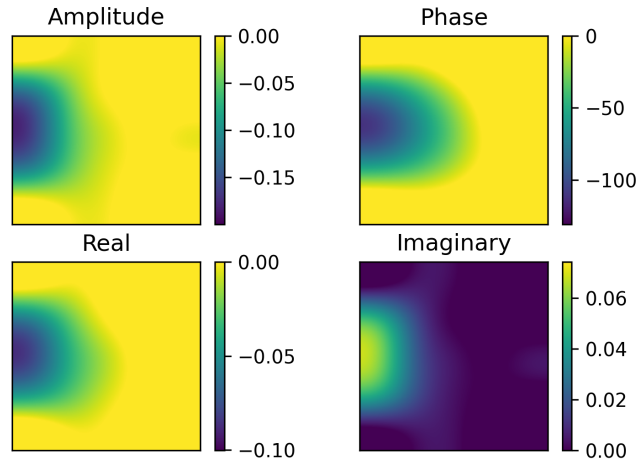
Examples of measurement data for a free-space (air) background is shown in Figure 3-14. These complex values enrich the information for further data analysis



and image reconstruction.



(a) Image of non-ferrous object



(b) Image of ferrous object

Figure 3-15: Image reconstruction from complex-valued hardware

Figure 3-15 shows examples of reconstruction results from complex-valued measurement data where the object (circle which diameter is quarter of the space) is placed on the West side. The Landweber algorithm described in Subsection 3.2.2 is used. The sensitivity matrix  $\mathbf{J}$  [5x5] is obtained experimentally by measuring small metals as perturbation at a single grid. It can be seen that the object's

location is indicated in the reconstruction. Different characteristics between non-ferrous object (Figure 3-15a) and ferrous object (Figure 3-15b) are distinctive.

Table 3.3: Hardware Comparison

Parameter	Magnitude sys (3.3.1)	Spectroscopy sys (3.3.2)	Complex sys (3.3.3)
Measurement	amplitude	$Z, \theta$	amplitude, phase real, imaginary
Main hardware	AVR 8-bit	LCR meter	ARM Cortex-A9 MPCore32-bit+FPGA
Detection range	5 V	2 V	$\pm 20$ V
Resolution	15-bit	NA	14-bit
Current source	100 mA	10 mA	10–100 mA
Frequency range	1–100 kHz	20 Hz–300 kHz	100 Hz–100 kHz
SNR	59–91 dB	55–96 dB	46–66 dB
Processing time	0.75 s	10 s	1.55 s

Table 3.3 shows a comparison between the three systems. It should be noted that SNR values are obtained experimentally using different sensors for different systems and purposes.

### 3.4 Summary

Methods for MIT and spectroscopy described in this chapter are, of course, not exhaustive. There are various algorithms that can be found in the literature. The algorithm and system described here will be used in the upcoming chapters. The Tikhonov algorithm is used in Chapter 4 and Chapter 6, whereas the spatio-spectral TV is used in Chapter 5. The Landweber is used as a test algorithm when developing the hardware. Neural network methods (Subsection 3.2.4) are used in Chapter 4 and Chapter 7. The hardware described in Subsection 3.3.1 is used in Chapter 4. The setup of Subsection 3.3.2 is used in Chapter 5, Chapter 6 and Chapter 7. The design from Subsection 3.3.3 is used in Chapter 4.

## Chapter 4

# Visualisation of Liquid Metal Flow Shape

This chapter describes MIT sensors for liquid metal visualisation. Design aspects and performance evaluation are presented to quantify the shape of conductive substance against the non-conductive region. Portable MIT sensors will be constructed and tested on GaInSn in the SEN model. Reconstruction results will be evaluated whether the feature meets the need to observe flow regime and phase distribution of steel in continuous casting. Flow shape classification method based on neural-network is also assessed for applicability in liquid metal imaging.

### 4.1 Introduction

Electromagnetic induction method is arguably the most applicable technique to visualise molten metal, since optical or nuclear means are not feasible for a real caster. Sensors have been developed and tested for liquid steel two-phase flow measurements [16] [19]. Previous researches [24] [112] have satisfactorily presented qualitative result on measurement and/or imaging liquid metal distribution in the vessel. In order to incorporate the apparatus onto a regulated process, a quantified information on both metal shape and inclusion, as well as a precise, fast measurement with a real-time reconstruction is required.

Sensors for monitoring the steel flow are needed, which are rugged, safe for plant

operation, and capable of visualising flow and clogging circumstances. As a real-world insight for interested readers, operation practices for steel cleanliness were reviewed in [113]. This work explores MIT sensors in a portable construction fitted for SEN model. The aim is to develop a measurement system which can be integrated into a control loop.

## 4.2 Continuous Casting Model

The liquid metal used in experiments is a eutectic alloy of gallium indium tin (GaInSn) which has a liquid phase in room temperature. Essential material property of GaInSn in term of electrical conductivity is 3.2 MS/m [114] which is intended for electromagnetic sensors. A small-scale facility for continuous casting model was constructed at Helmholtz-Zentrum Dresden-Rossendorf (HZDR) namely Mini-LIMMCAST (Liquid Metal Model for Continuous Casting) for experimental program on quantitative flow measurement of liquid metal [77]. This work contributes to a wider project framework reported in [115] and [116]. In order to control the process utilising data and/or image from tomographic sensors, the scheme of which is sketched in Figure 4-1.

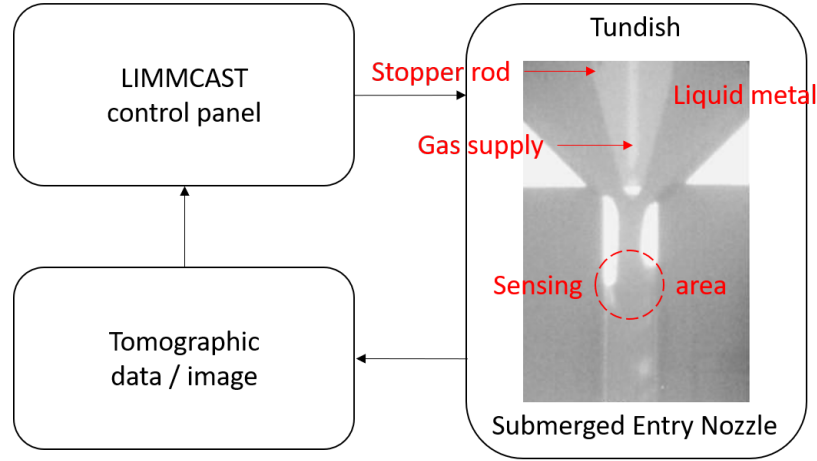


Figure 4-1: Mini-LIMMCAST scheme at HZDR.

The part of interest for this work, in particular, is SEN in which liquid metal is flowing from tundish to mould (x-ray captured Figure 4-1 right) [117]. Imaging area is focused on a section where the two-phase distribution of liquid metal and gas are present. In the Mini-LIMMCAST experiment, liquid metal velocity

in the SEN is approximately 1–2 m/s within which injected gas bubble size is estimated between 2 mm–5 mm in diameter. Therefore, the sensor should be sensitive to approximately 2.5%–20% area fraction of inclusion. As for the actual implementation, acquisition rate around 100 frame-per-second is required.

### 4.3 Sensor Design

The sensor's construction is seen in Figure 4-2. An individual part (left figure) is ferrite-cored multi-layer coil. Eight of them are assembled evenly ( $45^\circ$  axisymmetric) into a plastic housing (right figure) to form a circular array of coils circumventing the sensing space. Besides as a fitting for SEN pipe, the housing can be exploited for shielding to increase the sensors' sensitivity and reject any external interference. Structural details of the sensor are given in Table 4.1

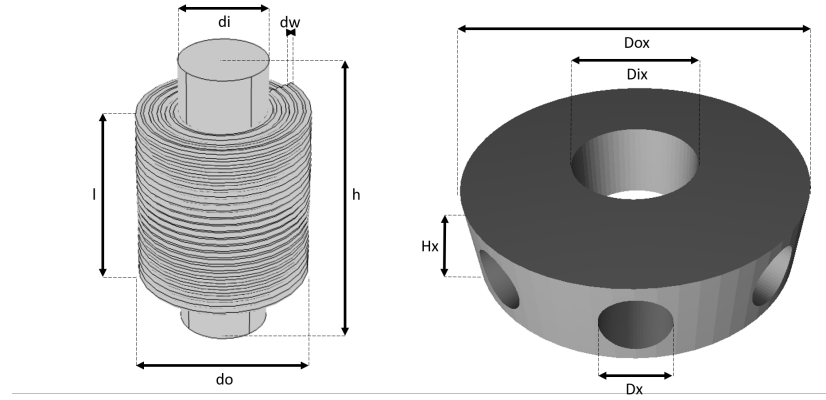


Figure 4-2: Sensor design.

In terms of measurement, the sensitivity of a ferrite-cored induction coil sensor is defined as the amount of induced voltage  $V$  per unit field  $H$  at operating frequency  $f$ , and can be calculated [118]:

$$\frac{V}{H} \approx 0.9 \times 10^{-5} \cdot f \cdot \frac{l^3}{d_w^2} \cdot d_i \cdot \frac{1}{\ln(2l/d_i) - 1} \quad (4.1)$$

From simulation (following method in [119]), it is evaluated that resultant magnetic field  $H$  (air background) on the edge of receiving coil ( $x = 7.5$  mm) is 1.2155 (A/m) at 1 kHz. An example of MIT receiving circuitry has resolution down to 0.125 mV, using combination of analog-to-digital conversion and programmable

Table 4.1: Sensor Parameter

Parameter	Symbol	Value
Wire diameter	dw	32 AWG
Coil inner diameter	di	2.5 mm
Coil outer diameter	do	5 mm
Coil length	l	5 mm
Core height	h	8 mm
Case inner diameter	Dix	15 mm
Case outer diameter	Dox	40 mm
Case slot diameter	Dx	7 mm
Case height	Hx	10 mm
Number of turns	N	100

gain amplifier [120]; while expected signal level for detection is 0.216 mV. Therefore, the designed sensor is expected to response towards the exposing field and generate sufficient level for common measuring hardware resolution.

## 4.4 Measurement Setup

The sensors are connected to MIT hardware system. The scheme is shown in Figure 4-3 (left) where 8-coils are formed surrounding SEN pipe made of PMMA with diameter of 15 mm and 2.5 mm wall thickness. Figure 4-3 (right) shows a setup in which a contained liquid metal strand (diameter of 7 mm) is placed in the centre of SEN pipe while MIT measurements are taken. Operating frequency of 130 Hz (penetrating 24 mm depth through GaInSn) is chosen. This particular operating frequency was also successfully applied in previous work on steel imaging [92].

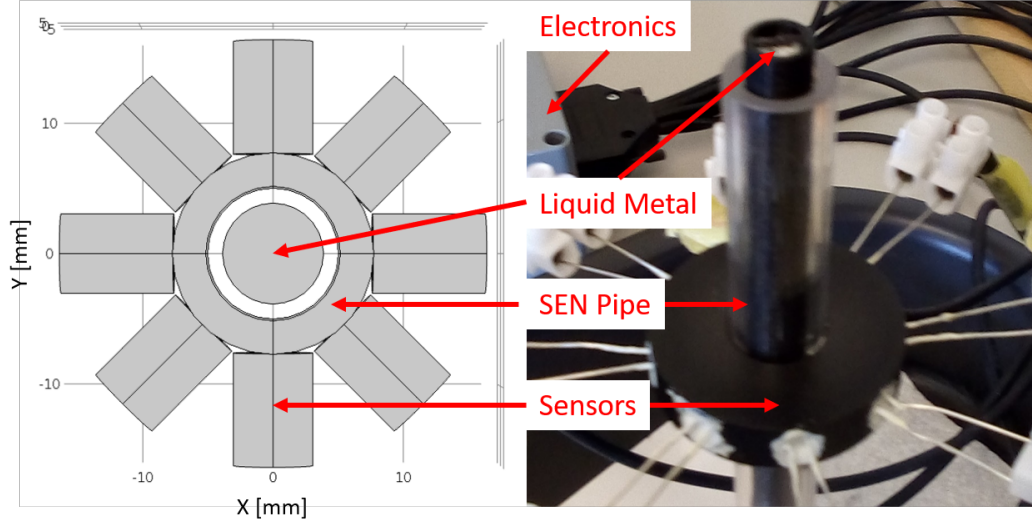


Figure 4-3: Experiment for liquid metal in SEN tube.

## 4.5 Visualisation Result

Conductivity distribution of material is obtained from measured data using image reconstruction technique. Induced voltage values are taken as a function conceived by electrical conductivity. Matrix equation can be described [19]:

$$\mathbf{V} = \mathbf{S}\mathbf{K} \quad (4.2)$$

where  $\mathbf{V}$  is voltage measurement data,  $\mathbf{S}$  is sensitivity map (representing responses of each sensors' section to particular measurement) also called Jacobian, and  $\mathbf{K}$  is conductivity values. Given the  $\mathbf{V}$  from experiment and the  $\mathbf{S}$  formulated from prior forward computation explained in Section 3.1, the pixelated conductivity  $\mathbf{K}$  can be estimated,

$$\mathbf{K} \approx \mathbf{S}^+\mathbf{V}. \quad (4.3)$$

The  $\mathbf{S}^+$  could be in form of  $(\mathbf{S}^T\mathbf{S} + \lambda\mathbf{R})^{-1}\mathbf{S}^T$  where  $\mathbf{R}$  and  $\lambda$  are the regularisation matrix and regularisation parameter (order of  $10^{-12}$ ) respectively. This method [121] to some extent is adequate for image observation, especially with high conductivity contrast and centralised distribution.

Since MIT will be applied to determine two-phase distribution of liquid metal and gas inside the SEN, tests with different filling regimes have been observed. Figure 4-4 (top of each section) shows several metal flow scenarios (assumed from Figure 4-1) molded as 3-d printed containers (PLA material) and measured by the sensor. The images are generated against either empty-air or full-metal background reference. Note that the 'empty' constitutes the SEN pipe with an empty container; whereas 'full' is the SEN pipe and a container filled with the liquid metal. Normalisation of low perturbation against high background was also explained in [122].

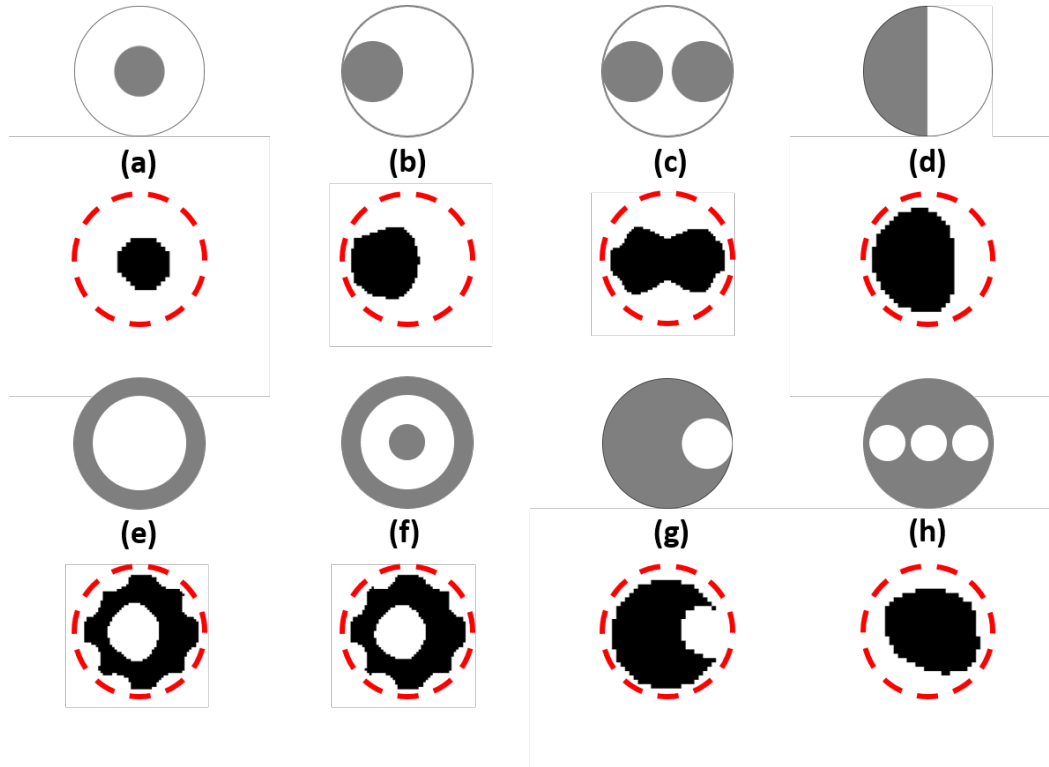


Figure 4-4: MIT imaging for metal flow scenarios in SEN.

The reconstructed images are shown in the bottom of respective sections in Figure 4-4. Red dashed-line indicates the actual boundary of the containers. From left to right, top-bottom, cross-sectional image is depicted for central-stream occupying 15% of total area (a), side-stream 20% (b), split-streams 20% each (c), stratified 50% (d), annular 50% (e), annular –wispy– with internal strand 7.5% (f), void-side 20% (g), and bubbly (three voids) each of which has area fraction 7.5% (h). Taking fully-filled metal as threshold value, there are distinct regimes



of conductive (metal) and non-conductive (gas) phase, except for difficult cases where the sensitivity is weak in the centre region. Still, the measurements have a good consistency across a hundred data for each case (measurement time of 12 seconds per frame) with an average signal-to-noise ratio (SNR) of 62.93 dB.

Evaluating the performance of MIT sensors in terms of imaging result, correlation coefficient (CC) and relative error (RE) are used, as commonly adopted for electromagnetic tomography [123],

$$CC = \frac{\sum_{i=1}^N (\hat{g}_i - \bar{\hat{g}})(g_i - \bar{g})}{\sqrt{\sum_{i=1}^N (\hat{g}_i - \bar{\hat{g}})^2 \sum_{i=1}^N (g_i - \bar{g})^2}} \quad (4.4)$$

$$RE = \frac{\|\hat{G} - G\|}{\|G\|} \quad (4.5)$$

where  $\hat{g}_i$  and  $\bar{\hat{g}}$  are  $i$ th element and average of the reconstructed image; while  $g_i$  and  $\bar{g}$  are  $i$ th element and average of the actual distribution respectively. On the other hand,  $\hat{G}$  is overall reconstructed image; whereas  $G$  is overall actual distribution.

Table 4.2: Imaging Evaluation

Shape	CC	RE
Central stream (a)	0.8888	0.2787
Side stream (b)	0.9063	0.2048
Split streams (c)	0.8693	0.2213
Stratified (d)	0.8928	0.2979
Annular (e)	0.4284	0.7472
Wispy annular (f)	0.3506	0.7012
Void side (g)	0.9015	0.3666
Bubbly (h)	0.8002	0.5702

Table 4.2 lists imaging evaluation for different cases. If the image and the actual shape are directly correlated, the value of CC will be approaching unity; whereas if the image and the actual shape are identical, the value of RE will be zero. Central-stream, side-streams and stratified cases are reconstructed quite well. The void-side case still has a decent confirmation. For internal recovery such as wispy-annular and bubbly cases, the distribution are failed to be seen, as reflected

by correlations below 0.5 and higher error values. The nature of reconstruction algorithm and the simplified subtraction/thresholding method are among reasons why image generation for some cases are less satisfactory and having artifacts at different regions depending on the object's distribution. In the future Mini-LIMMCAST experiment, metal strand and/or bubble size around 5 mm in the SEN would be the detection limit of the designed sensors.

## 4.6 Classification using Neural-Network

Integrating the visualisation into an environment such as a control system, it is desirable to reduce the dimensionality of the information. Sensors measurement data could be translated into flow shape categories through classification scheme. NN has been used for such classification problem based on input data vector. This section takes the approach for flow shape classification which takes measurement data as input and provides prediction of the associated flow shape.

The network is built from scratch while adjusting an efficient architecture for the given problem and dataset. The NN model is implemented in Keras 2.4.0 framework [124] with TensorFlow 2.3.0 backend [125]. The performance is evaluated using accuracy, i.e. ratio of correctly classified samples vs all available samples [126]:

$$acc = \frac{\sum_{m=0}^{k-1} c_{m,m}}{\sum_{m=0}^{k-1} \sum_{n=0}^{k-1} c_{m,n}} \quad (4.6)$$

where  $c_{m,n}$  are the elements of the confusion matrix. The network is also trained to minimise the loss between prediction and true labels.

The datasets are induced voltage collections of several pre-shaped flow regime variations and used to train a machine learning model. Common two-phase liquid-gas flow scenarios such as full-stream, stratified, bubbly, and annular are investigated. Detailed in Table 4.3, datasets are created and labelled for five classes, and split into training and test data. The validation set is randomly chosen from training data during the training process.

Figure 4-5 shows the classifier architecture, which is a multi-layered dense neural network. Keras model Sequential is constructed consisting of a hidden dense layers which has 128 neurons, with activation function ReLU. The input data is

Table 4.3: Flow Shape Dataset

Label	Class	Train Data	Test Data
0	Stratified	90	10
1	Full	90	10
2	Split	90	10
3	Annular	40	10
4	Bubbly	21	10

a set (28 coil pairs combination) of MIT measurement values. Vector of “logits” scores for each class are then converted into probability using a Softmax function. It provides a number of outputs according to the prediction classes.

The total number of parameters (param) is 4357, all of which are trainable. Model summary is described in Table 4.4. Loss function Sparse Categorical Crossentropy takes a vector of logits and a “True” index and returns a scalar loss for each example. The model is compiled using optimiser ADaptive with Momentum (Adam), utilising “accuracy” metrics to measure the loss and the accuracy of the model.

Table 4.4: NN Model Summary

Layer	Properties	Output Shape	Param
input	28 x 1	(28)	0
Dense1	Activation: ReLU	(128)	3712
Dense2	+ Softmax	(5)	645

This model will then be fitted adjusting parameters to minimise the loss. Figure 4-6 shows training and validation accuracy-loss along epochs. After 50 epochs on the given datasets, this model produces 4% training loss and 99% training accuracy; whereas validation loss is 0.06 and validation accuracy is 0.99. This is detailed in Table 4.5.

Training and test utilize CPU with four compute cores clocked at 2.3 GHz and 4 GB of RAM. The training time for all data within complete number of epochs lasts 16.089 s, whereas the test takes 0.5781 s. Examples of prediction on flow shapes are depicted in Figure 4-7. Ten test data are fed into the model, and the prediction bar chart is shown accordingly. The chart shows how confident the model decides that the data corresponds to each class.

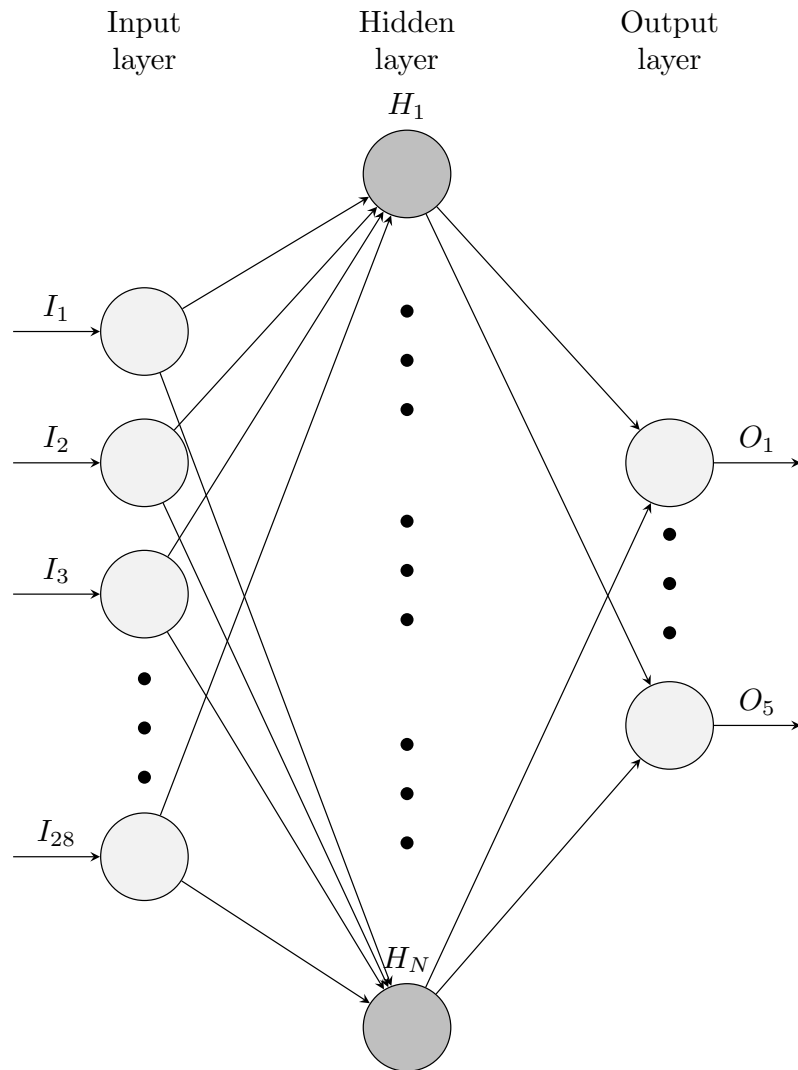


Figure 4-5: Neural network classifier model.

Table 4.5: NN Performance Evaluation

	Value
Train accuracy	0.9939
Train loss	0.0419
Test accuracy	1.0000
Test loss	0.0593
Epoch	50

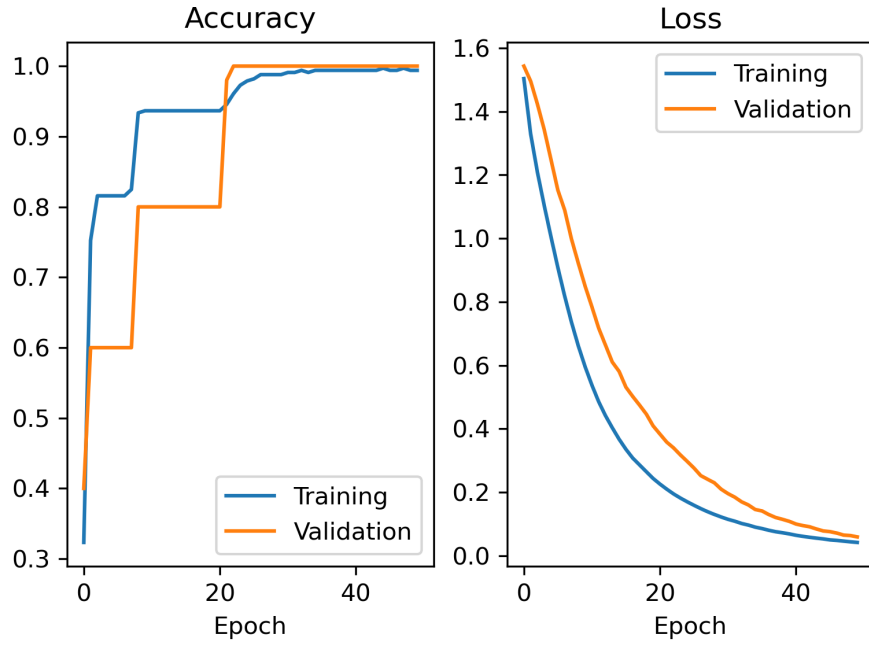


Figure 4-6: Training and validation accuracy-loss vs epoch.

The normalised confusion matrix is shown in Figure 4-8. The map represents tests, where each case has ten predictions. The classifier produces a good accuracy where all flow-shape classes are predicted correctly to the maximum scale. Refined with representative flow scenarios, the trained model could be deployed for an intelligent online control system of liquid metal flow.

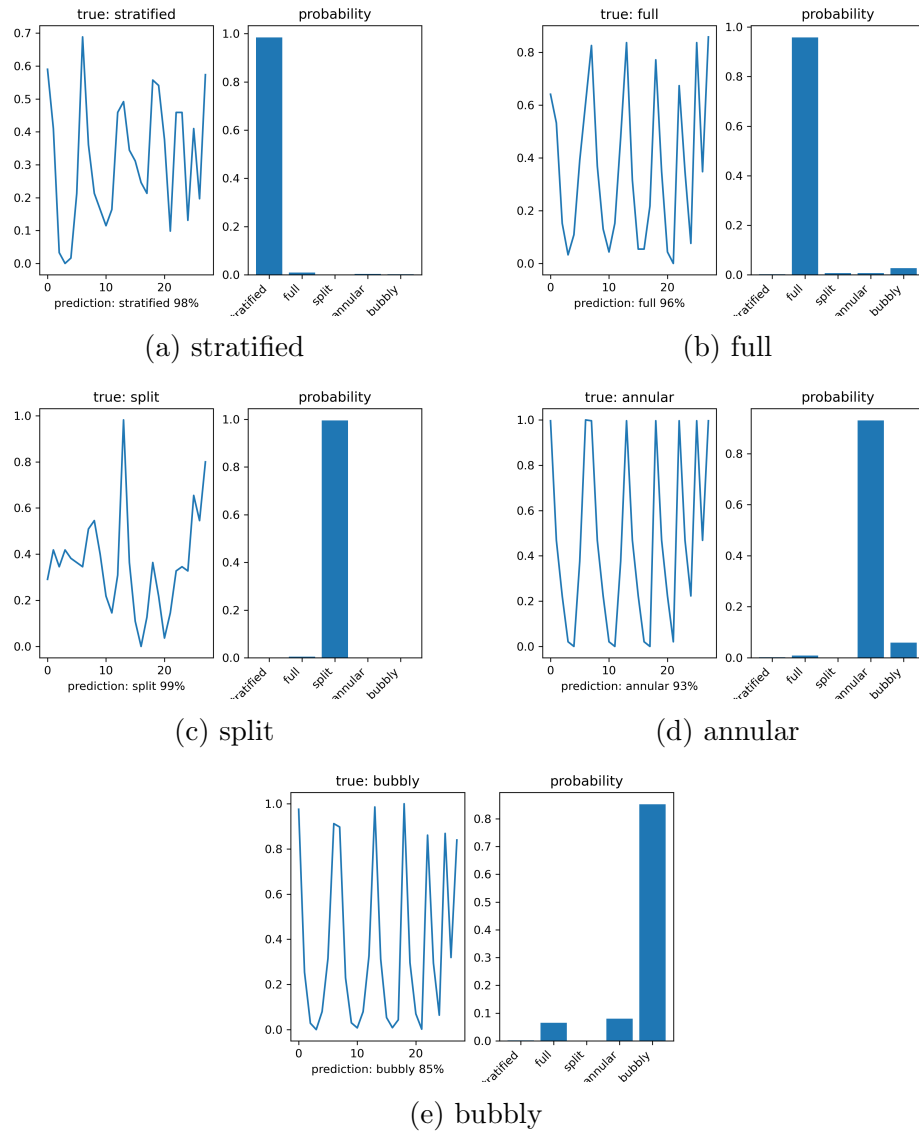


Figure 4-7: Plot prediction of flow shape

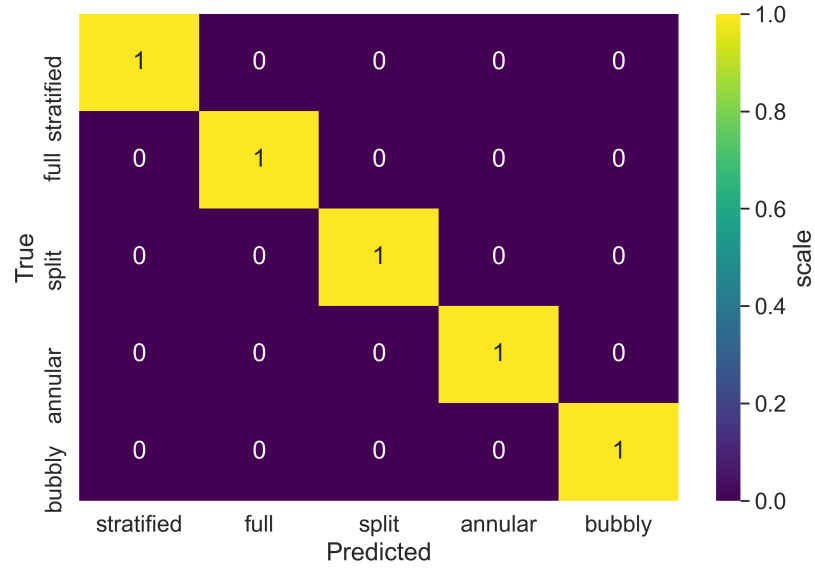


Figure 4-8: Normalised confusion matrix.

## 4.7 Conclusion

The MIT sensors have been designed and tested to visualise the static liquid metal profile inside the SEN model for steel casting. Quantitative evaluations are provided for several flow scenarios, both outer shapes and internal recoveries. Flow shapes are satisfactorily reconstructed with good correlations and low imaging errors. However, inner structures are difficult to obtain, especially for small-centralised inclusion or distributed bubbles. Future directions would be to use spectroscopy methods for accurately revealing internal distributions, frame rate improvement, and time-dependent behaviour. Neural-network classifier performs satisfactorily in detecting common flow shapes. The proposed sensor and detection methods have the potential to be implemented for the Mini-LIMMCAST facility in an integrated control experiment.

## Chapter 5

# Structural and Functional Characterisation in Metallic Materials

This chapter investigates a multi-frequency MIT using both amplitude and phase data. The image reconstruction algorithm is based on a novel spectrally correlative total variation method allowing an efficient and all in one spectral reconstruction. Additionally, this shows the rate of change in spectral images with respect to the excitation frequencies. Using both spectral maps and their spectral derivative maps, one can derive key structural and functional information regarding the material under test.

### 5.1 Introduction

Material characterisation as well as substance examination are important procedures in many sectors. A comprehensive knowledge on a sample is desired before, during, and after a process. In the case of metallic target, passive electromagnetic properties such as conductivity and permeability convey crucial information about its structural and functional traits. This leads to the employment of inspection techniques based on electromagnetic measurements.

Eddy current is widely accounted for examining a metal embodiment. Its applic-



ation for non-destructive testing has been continuously developed and adapted [127]. In addition to a direct defect observation, electrical conductivity is also measured using eddy current method [128] [129]. Commonly, a coil probe is employed to pick magnetic fields, primary from exciter and secondary from the target's response, then both amplitude and phase in the induced signal are extracted to give an indication of the target's characteristics. The coil probe is relatively more sensitive to drastic disruption in eddy current flow with high dynamic range.

Multi-frequency technique expands the capability of the single frequency technique. The wide-band signal can profile the structural depth inside metallic materials [130]. Therefore, it is able to accurately examine the properties since the use of only a single lower frequency resulting in a reduced signal-to-noise ratio in the detection. Furthermore, data at different frequencies can be correlated to characterise the object under test. Some reports studied the spectral response of pulsed eddy current [131], a multi-frequency technique for material characterisation [132], and frequency sweep and impedance normalisation method [133].

Measurement of field and impedance variations also facilitates conductivity imaging in the materials. The inversion of inductive spectra was employed to determine characteristics such as magnetic permeability, electrical conductivity, and thickness [134]. Multiple frequency data can be reconstructed simultaneously to exploit correlation among conductivity distributions at different frequencies [135]. Thus, different excitation frequencies enriches the information, improves the inverse method, and strengthens the system against experimental noises [136].

Magnetic induction spectroscopy (MIS) is a method for measuring conductivity spectrum in non-destructive and contactless technique [137]. The term was introduced in [138] which then has been followed by subsequent works to measure the conductivity spectrum using gradiometer coil sensor [139], utilising differential methods [140], and signal improvement scheme [141]. The use of inductance spectroscopy has been exploited for imaging both continuous conductivity profile [142] and permeability distribution of a layered sample [143]. Applications of magnetic induction spectroscopy have been found in biological and industrial areas.

The design of a practical MIS system was reported specifically for bioelectrical impedance spectroscopy on yeast suspension in saline, fruits, and tissue [144]. Recent spectroscopic bioimpedance measurement was described for industrial-scale agricultural produce [145]. In medical domain, gradiometer sensors were designed to perform in vivo spectroscopic measurement on human hand [146]; meanwhile electromagnetic phase-shift spectroscopy was developed to diagnose brain edema and brain hematoma [147].

On the other hand, industrial implementations vary from detection, classification, and characterisation. Spectroscopic metal detection provides rich and distinctive information about a target to help reducing false alarm rate in landmine detection [148], also for buried pipeline tracing in difficult terrain [149]. Additionally, metal recycling sector requires sorting process, for which a classification of non-ferrous metals based on MIS was developed in [150]. Particular frequency feature was proposed for imaging a welding cross-section [151]. Internal material structure examinations using inductance spectroscopy measurement were presented in many investigations such as in [152] [153] [154]. The demand for in-line monitoring of phase transformation in the steel industry is answered by multi-frequency electromagnetic instruments [155] [156] [157] [158].

Previous researches on MIS deal with hardware development [159], as well as characterising ferromagnetic materials [160]. Various image reconstruction methods for soft field tomography techniques have been reviewed in [161]. Tikhonov regularization method is commonly used in solving MIT inverse problem. This least square solution has disadvantages such as an overly smoothed image so that boundaries between samples become obscure. The use of an L1-norm regularization, e.g. total variation (TV), can improve the MIT image quality. It is a more suitable method for both sharp edges and high contrast. However, this method faces difficulty in low-contrast recovery. The iterative technique has been proposed to fix the low-contrast recovery problem [162]. It provides a sequence of solutions which allows recovering the contrast lost. In this work, the author aims to inspect metallic samples with functional and structural variations. The algorithm is proposed for spectrally correlative imaging as magnetic induction tomography spectroscopy (MITS). Spatial maps of conductive spectrum and its derivative are presented.

## 5.2 Experimental Setup

A multi-frequency data collection is proposed to cover wide range of frequency spectrum. The experimental setup is depicted in Figure 5-1.

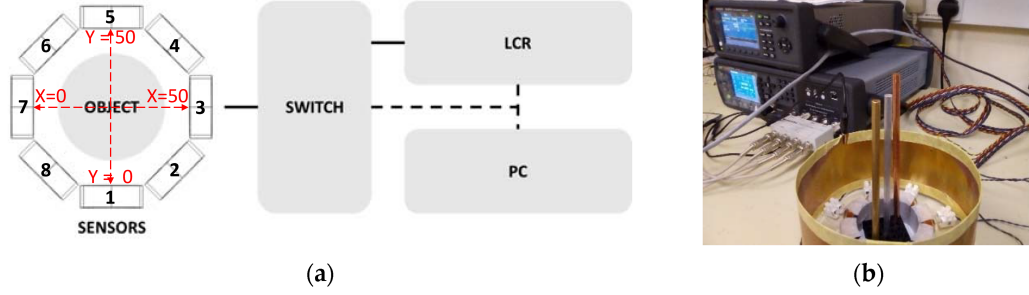


Figure 5-1: Measurement setup: (a) sketch of the sensor array and object in the sensing region, switch, LCR meter, and PC connection (signal solid-line; control dashed-line); (b) photograph of the system.

The sensors comprise eight coils arranged encircling the sensing space with diameter of 50 mm. An individual sensor is off-the-shelf induction coil with self-inductance value of 0.1 mH and  $0.3 \Omega$  intrinsic resistance. Amplitude and phase measurements of mutual impedance between sensors (transmitting - receiving coils) are acquired by LCR meter (frequency range 20 Hz - 300 kHz). For 8-coil arrays, switch module is introduced to accommodate 28 independent coil-pairs measurements. Synchronous operation between mutual coil selection (switch) and current-source with potential-sense (LCR) is controlled by instrument programming interface on PC. It takes approximately 10 minutes to collect a complete cycle of measurement.

Background measurement is taken for free space (air) condition in the sensing region as a reference. The amplitude spectrum is formed as normalised mutual impedance of an object ( $Z$ ) against free space ( $Z_0$ ); whereas phase spectrum is the difference between measured phase in the presence of an object ( $\theta$ ) and that of free space ( $\theta_0$ ), shown in Figure 5-2, Figure 5-3 and Figure 5-4. Measurements from nearby coil pairs have relatively higher values than those from far pairs. The coil numbering can be referred from Figure 5-1.

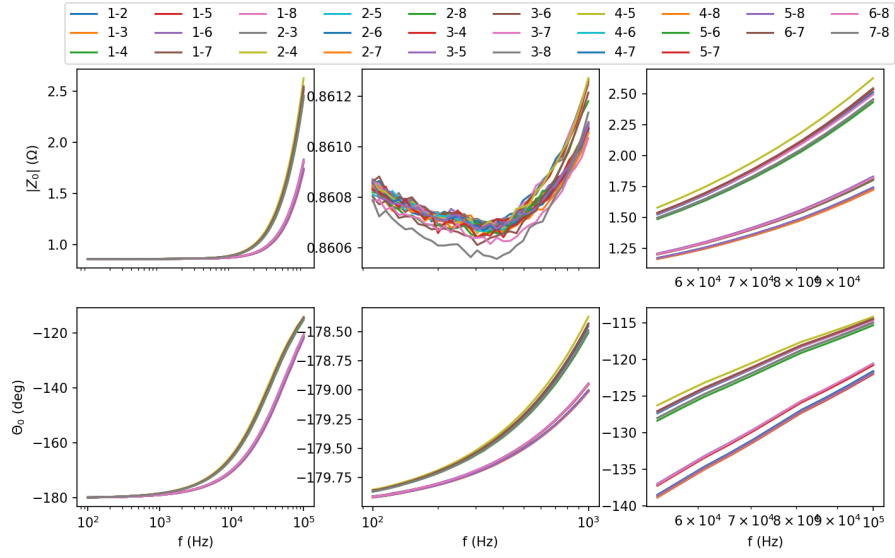


Figure 5-2: Free space background measurement of amplitude (top) and phase (bottom) for 28 coil-pair combinations, with zoomed view at low and high frequencies for both graphs.

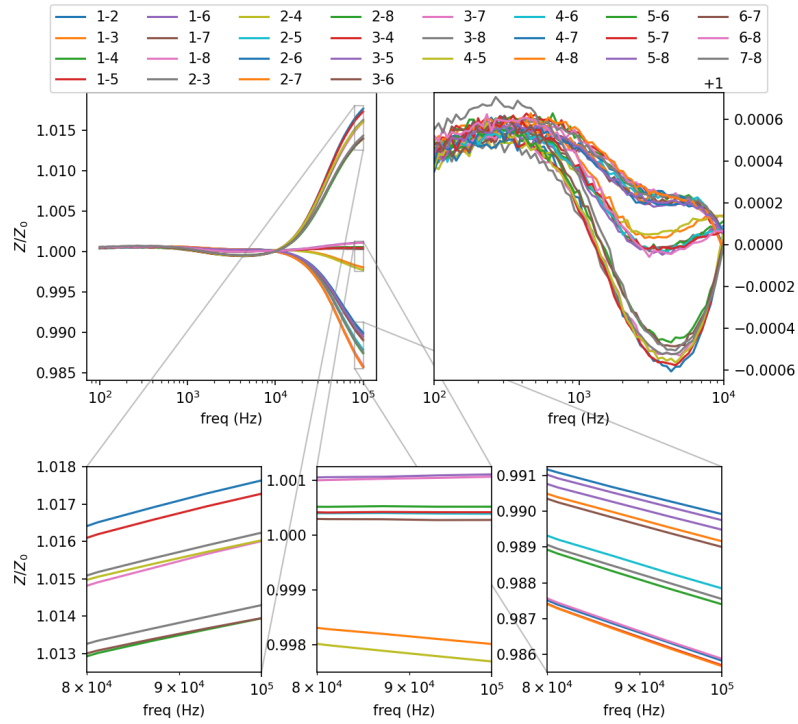


Figure 5-3: Amplitude spectrum of a test (GaInSn with diameter 1 inch placed at the centre) sample plotted against background.

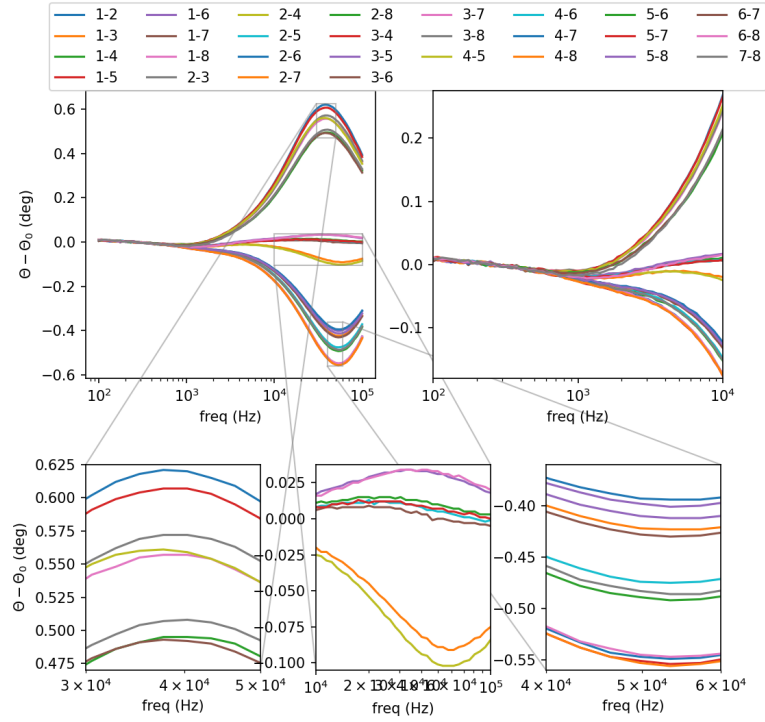


Figure 5-4: Phase spectrum of a test sample (GaInSn with diameter 1 inch placed at the centre) plotted against background.

For simplicity, norm values of 28 measurements are presented to show spectral plots of the upcoming investigated cases. Fundamental plots are given for several cases: conductivity, size, and structure variations.

Figure 5-5 shows spectral plot for different metallic samples whose conductivity are varied. Each sample is 0.25 inch in diameter and placed at the centre (Position can be referred from Figure 5-1). From the highest to the lowest are copper (58.4 MS/m), aluminum (26.3 MS/m), brass (16.1 MS/m), and Galinstan (3.2 MS/m). Left vertical axis is normalised amplitude for solid-line plot; while phase difference for dashed-line plot is on the right axis. The inclinations (for amplitude) and peaks (for phase) are distributed following the respective conductivity values.

Figure 5-6 shows spectral plot of aluminum rods with different diameter (small = 0.25 inch, big = 0.5 inch). Both amplitude and phase curves have larger scales for a larger object's size.

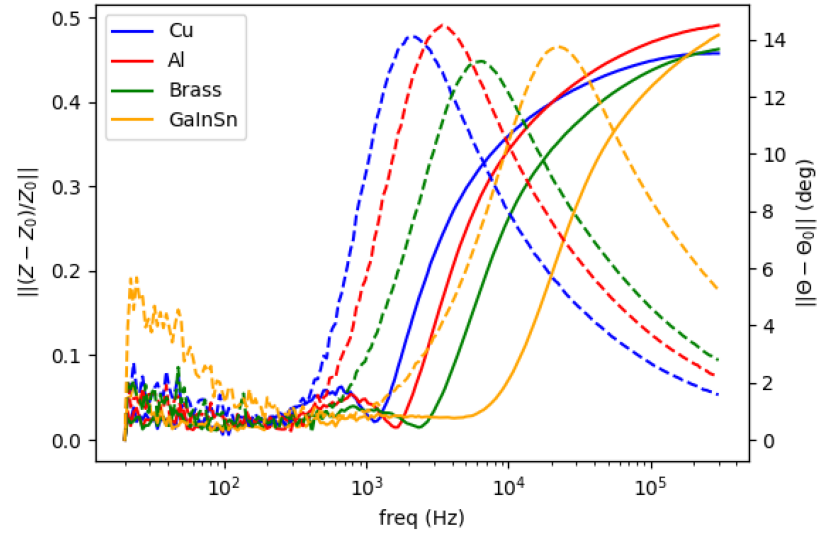


Figure 5-5: Spectral plot for metallic samples (conductivity variations). Solid line for amplitude ratio (left vertical-axis); dashed line for phase difference (right vertical-axis).

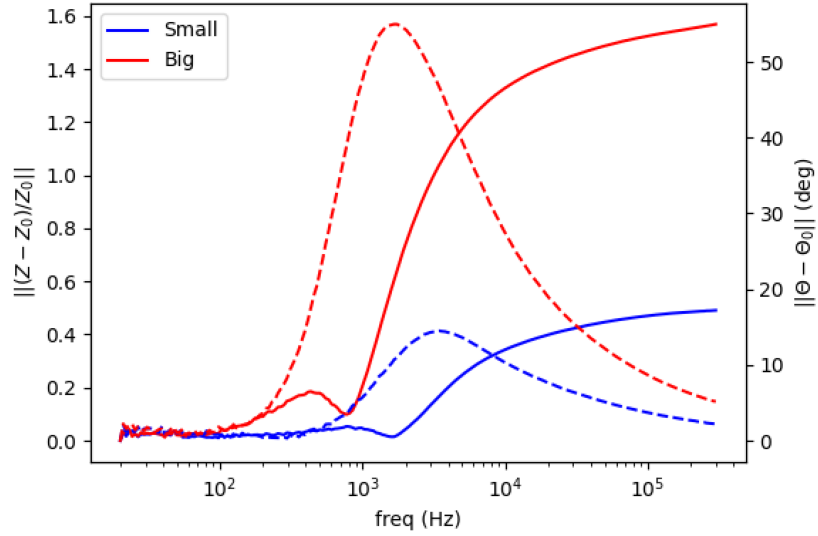


Figure 5-6: Spectral plot for size variations. Solid line for amplitude ratio (left vertical-axis); dashed line for phase difference (right vertical-axis).

Figure 5-7 shows spectral plot of aluminum samples with different structures: pipe (hollow cylinder with outer diameter 0.5 inch and inner diameter 0.4 inch), pipe (as previous) with 0.25 inch aluminum rod inside, and solid aluminum rod 0.5 inch. There are no significant differences in amplitude curves, whereas in

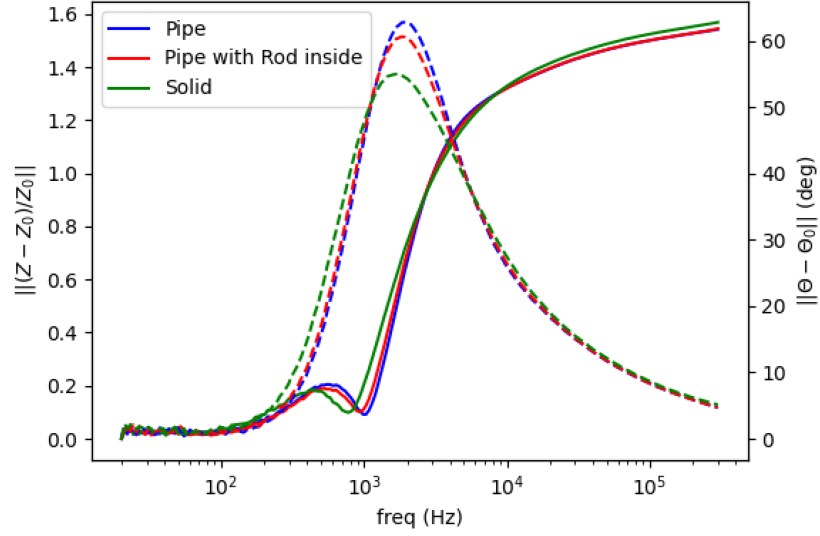


Figure 5-7: Spectral plot for metallic structure. Solid line for amplitude ratio (left vertical-axis); dashed line for phase difference (right vertical-axis).

phase curves, peaks' signatures reveal distinct fashions according to the objects' structures. They might be caused by interaction between fields resulting from eddy current in the pipe and fields from eddy current in the rod.

Observing the aforementioned cases, spectral characteristics can be further treated into frequency derivative to classify metallic materials. These are shown in the following Figures 5-8–5-10. There  $ndata$  is  $\|(Z - Z_0)/Z_0\|$  for amplitude data and  $\|\theta - \theta_0\|$  for phase data. The derivative is used to reveal the frequency location where the data reach its extrema. This frequency location will be treated as spectral signature of object under test.

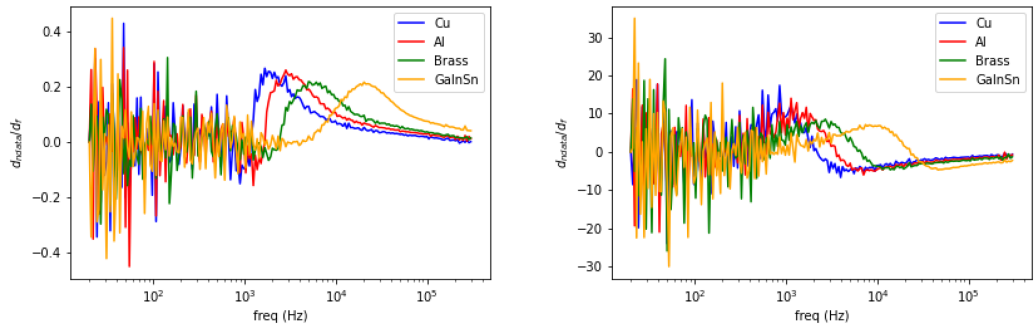


Figure 5-8: Spectral derivative for metallic samples with conductivity variations (left: amplitude, right: phase).

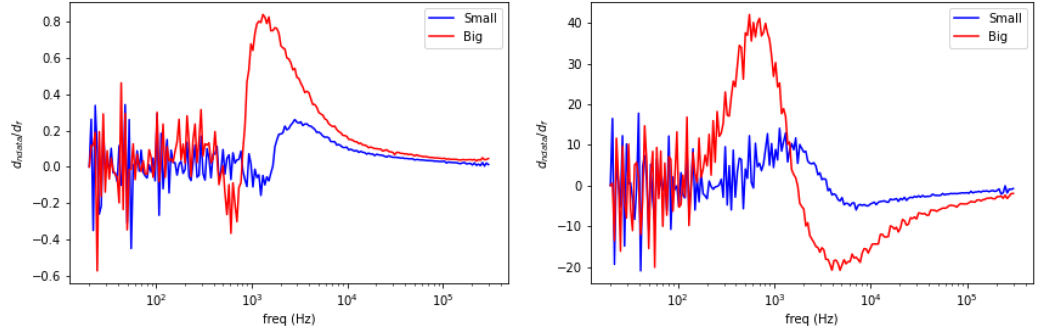


Figure 5-9: Spectral derivative for size variations (left: amplitude, right: phase).

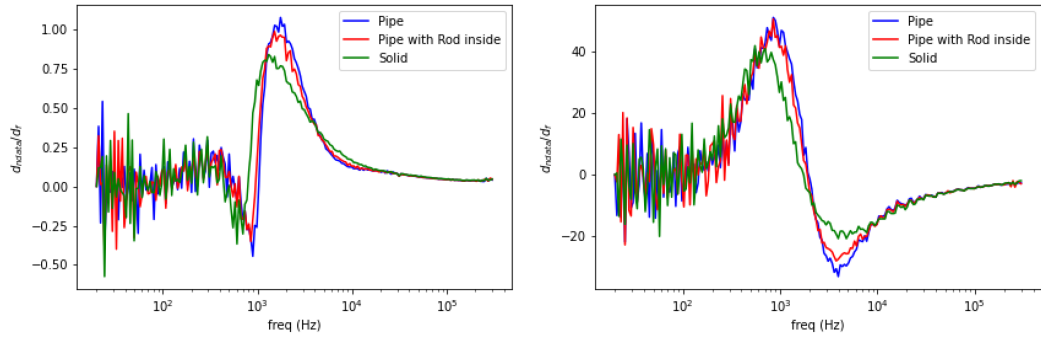


Figure 5-10: Spectral derivative for metallic structures (left: amplitude, right: phase).

The spectral data at every frequency are reconstructed into images using an algorithm described in Subsection 3.2.3. This produces three-dimensional spectral image (2D spatial image plus 1D frequency axis). In order to simplify the presentation, 2D image will be evaluated along the diameter across the centre (line position  $Y=0$  to  $Y=50$  in Figure 5-1). Therefore, it turns into 1D image values (as vertical axis) and 1D frequency values (as horizontal axis).

### 5.3 Results and Analysis

Images were reconstructed for different circumstances of metallic materials: a single conductive sample, different samples at different positions, and nonconductive inclusion in a conductive body. For each condition, a contrast is observed in both measurement data and its spectral derivative. Spatial reconstruction along the frequency is also given. Due to either measurement setup or ambient



disturbance, the noise will be present in the data (especially at low frequency). Therefore, 'smooth' function in MATLAB is applied to reduce the noise within a data set.

### 5.3.1 Single Metal Sample

Figures 5-11, 5-12, 5-13 and 5-14 show the spectral profiles and the derivative of spectral profile with respect to the frequency for various metal samples. All samples are of the same size and located at the centre of the imaging area. The 'position' axis can be referred to pixel position  $Y=0$  to  $Y=50$  in Figure 5-1. These are the images using phase data from mutual inductance. The maxim phase profile coincides with when the derivative profile goes down to 0. The frequency for which the phase profile is its maximum and the derivative tends to 0 is an indicator of the electrical conductivity of the test sample.

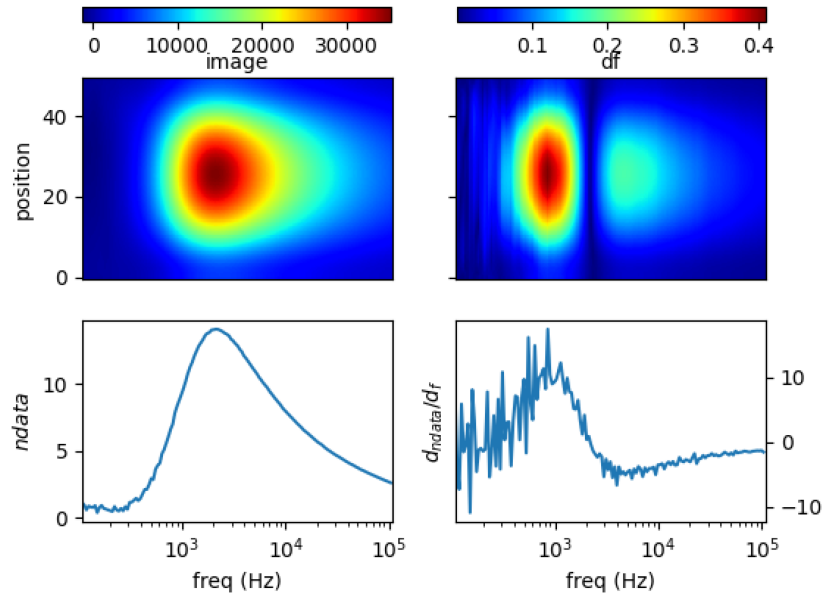


Figure 5-11: Spectral profile and its derivative (data and reconstructed image values) for copper ( $\sigma = 58.4$  MS/m) rod 0.25 inch. Images on top are produced by reconstructing raw data plotted below.

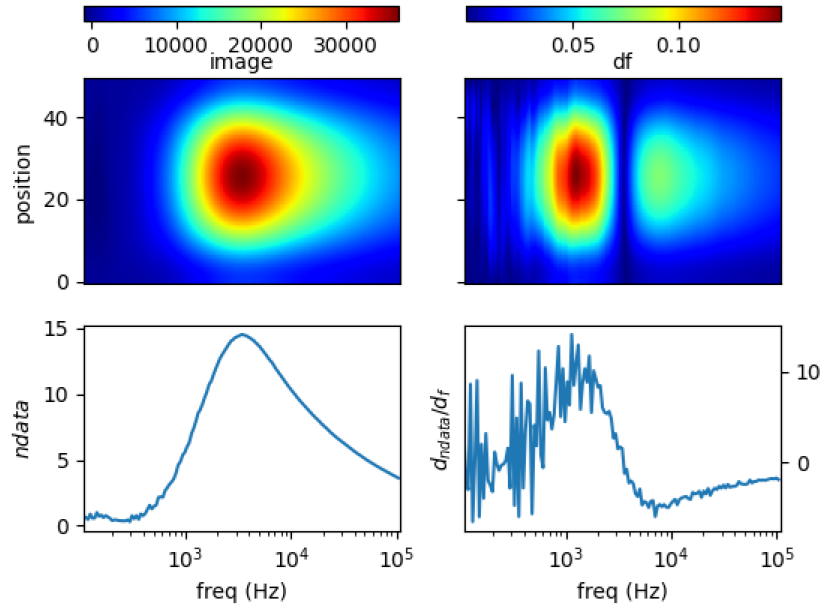


Figure 5-12: Spectral profile and its derivative (data and reconstructed image values) for aluminum ( $\sigma = 26.3$  MS/m) rod 0.25 inch. Images on top are produced by reconstructing raw data plotted below.

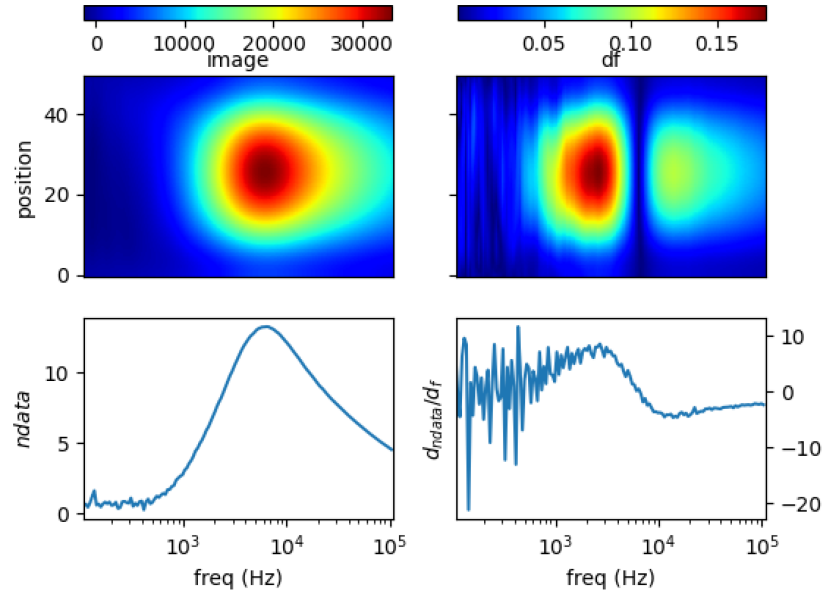


Figure 5-13: Spectral profile and its derivative (data and reconstructed image values) for brass ( $\sigma = 16.1$  MS/m) rod 0.25 inch. Images on top are produced by reconstructing raw data plotted below.

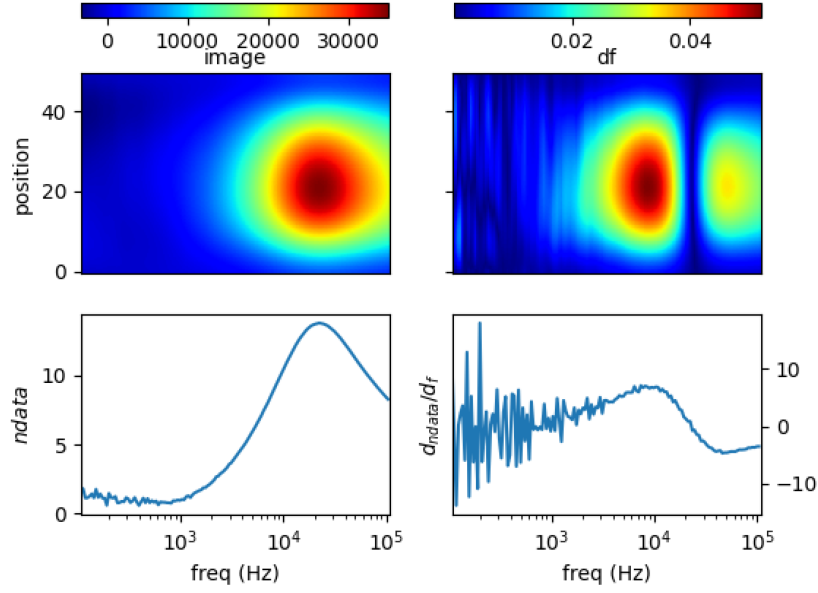


Figure 5-14: Spectral profile and its derivative (data and reconstructed image values) for liquid GaInSn ( $\sigma = 3.2$  MS/m) in 0.25 inch tube. Images on top are produced by reconstructing raw data plotted below.

Norm of measurement data ( $ndata$ ) and spectral derivative ( $dndata/df$ ), with the respective spatial reconstruction from data ( $image$ ) and spectral derivative ( $df$ ) are given. For reconstruction figures (top), vertical axis is spatial cross-section (pixelated) where position=0 is the location of sensor coil 1; and position=50 is that of sensor coil 5. The horizontal axis represents frequency points associated with the horizontal  $\log(freq)$  axis of the bottom figures.

It can be seen for different samples with different conductivity levels, there are value shifts in phase spectrums. The signatures' locations are marked in spectral derivative data/images, where zero values indicate the extremes of the norm data or the respective reconstructed images.

### 5.3.2 Different Samples at Different Locations

The distribution of different samples at different locations is evaluated. Figure 5-15a shows a more conductive sample (copper) at position=10 and less conductive sample (brass) at position=40. In the reconstructed image, there are two distinct regions depicting the objects, one starts at lower frequency (for higher conduct-

ive), whereas the other (for lower conductive) lies at higher frequency. In the spectral derivative there is pronounce line cutting-through 'position' that shows the location of both samples, initiating from a more conductive sample at bottom position, then it turns to a less conductive sample at top position.

Figure 5-15b shows three samples (two at both edges, one at centre) the lowest conductive sample (brass) at position=10, moderate conductive sample (aluminum) at position=25, and the highest conductive sample (copper) at position=40. In the reconstructed image, there should be three different regions representing the objects. However, due to non-uniformity in the sensitivity (highest at near sensors, lower at central region) and further affected by regularisation, the object in the middle is obscure. For instance, regularisation controls the sharpness of the image, so that with improper parameters the resulting image might expand or shrink beyond the actual object's boundary. Still there is an inclined line in the spectral derivative that shows the gradation from low conductive (bottom position), mid-range (centre), to high conductive (top position).

### 5.3.3 Non-Conductive Inclusion in Conductive Liquid

Particular case likely to be found in the practical applications is the presence of non-conductive substance in a conductive body. An eutectic GaInSn alloy ( $\sigma = 3.2 \text{ MS/m}$ ) was prepared in a 1 inch diameter tube. A wood cube ( $s = 1 \text{ cm}$ ) is immersed on the side of the tube (position=10 relative in sensing region). This makes up a conductive body with inner void. Figure 5-16 shows spectral reconstruction and its derivative. It is obvious in the image, there is low value centering around 40 kHz which indicates the void. This corresponds to a zero-valued line occurs between high-valued contours in the spectral derivative.

Three plastic rods (diameter = 0.25 inch) are inserted in the liquid metal tube, located at centre and both edges (position 10, 25, and 40) to construct multiple structural void in a conductive body. In Figure 5-17, spectral image reveals an elongated low-valued region from spatial position 10 to 40. This should indicates the three inclusions, yet the sensitivity and regularisation effect fail to separate those voids. Accordingly, in the spectral derivative, there is a distinct zero-valued line at around 40 kHz cutting along the spatial position.

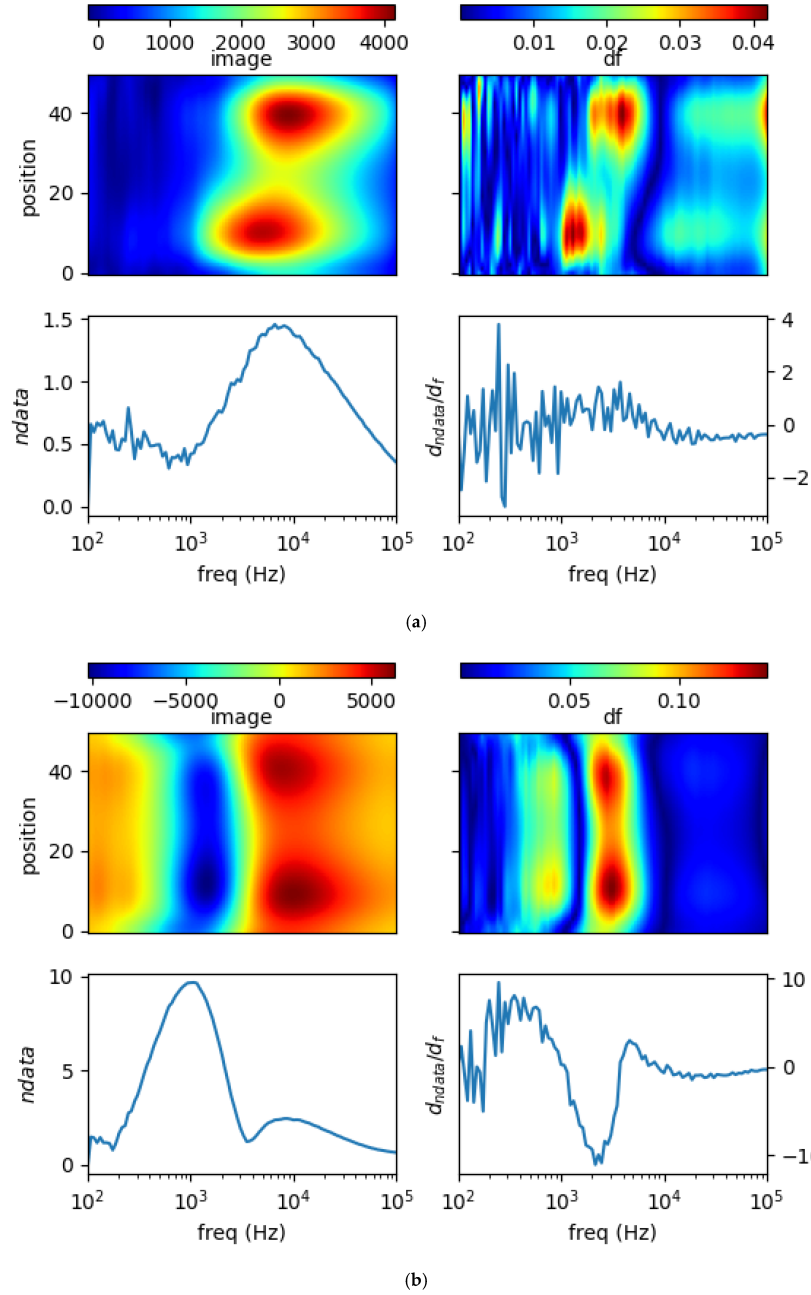


Figure 5-15: Spectral profile and its derivative (data and reconstructed image values) for (a) Copper ( $\sigma = 58.4$  MS/m) rod 0.25 inch at pos=10 and brass ( $\sigma = 16.1$  MS/m) rod 0.25 inch at pos=40; (b) Brass ( $\sigma = 16.1$  MS/m) rod 0.25 inch at pos=10, aluminum ( $\sigma = 26.3$  MS/m) rod 0.25 inch at pos=25, and copper ( $\sigma = 58.4$  MS/m) rod 0.25 inch at pos=40. Images on top are produced by reconstructing raw data plotted below.

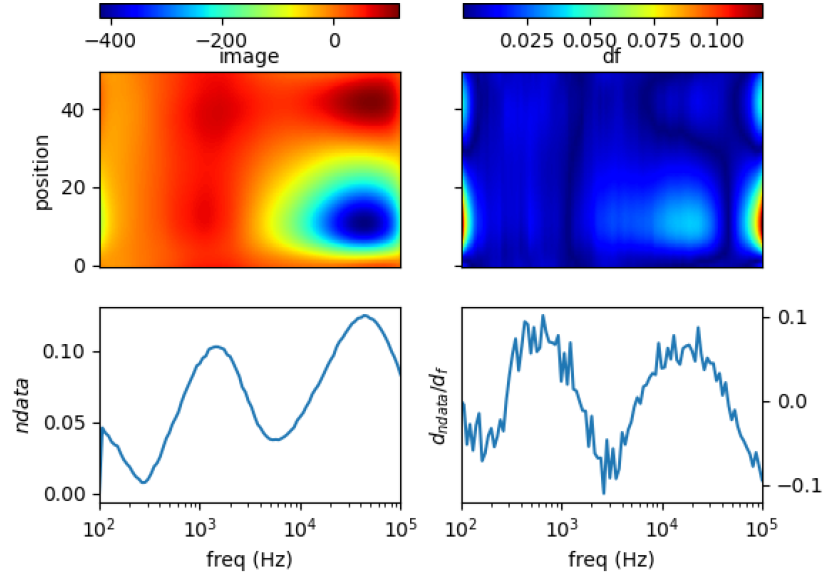


Figure 5-16: Spectral profile and its derivative (data and reconstructed image values) for wood cube 1 cm<sup>3</sup> at pos=10 in liquid GaInSn 35 mL 1 inch tube. Images on top are produced by reconstructing raw data plotted below.

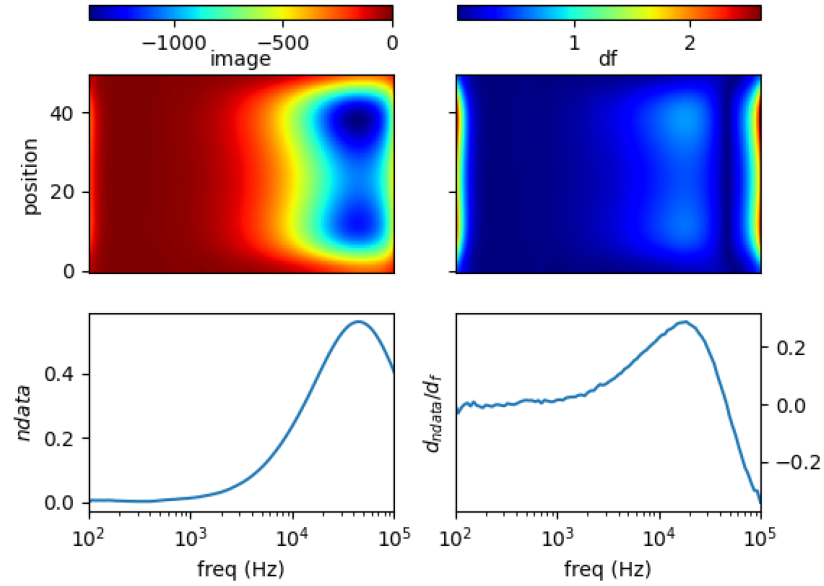


Figure 5-17: Spectral profile and its derivative (data and reconstructed image values) for plastic rods 0.25 inch at pos=10, pos=25, pos=40 in liquid GaInSn 35 mL 1 inch tube. Images on top are produced by reconstructing raw data plotted below.

### 5.3.4 Spectral Derivative for Structural and Functional Classification

Taking curve characteristics in Section 5.2, spectral gradient is applied to correlate metallic object circumstances with the respective image spectrums. The following Figures 5-18--5-20 show spectral gradient of amplitude ( $Z$ ) and phase ( $\theta$ ) reconstruction.

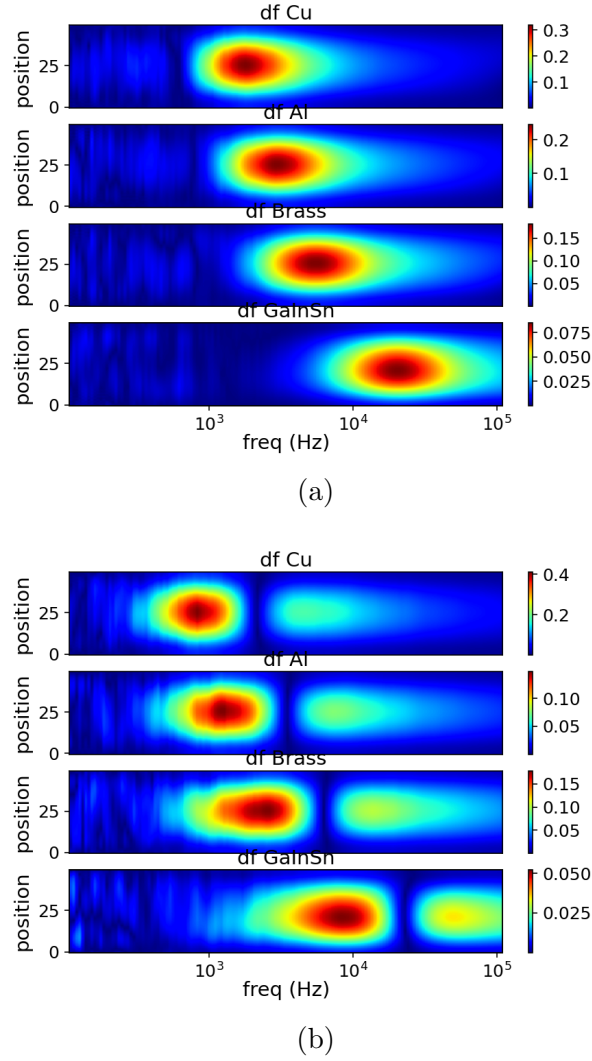
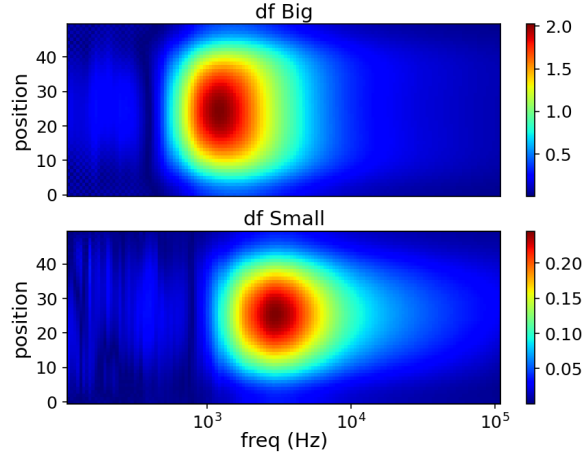
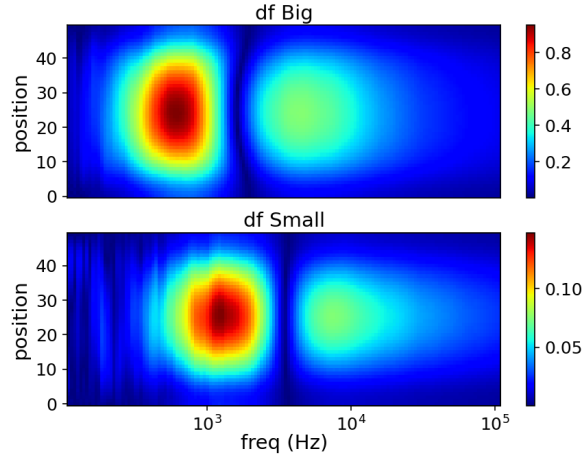


Figure 5-18: Spectral gradient impedance images  $df$  of (a) amplitude  $Z$  and (b) phase  $\theta$  for metallic samples with conductivity variations. Bottom to top are GaInSn, brass, aluminum and copper.

Figure 5-18 illustrates spectral derivative for amplitude and phase reconstructions from single sample with different conductivity levels (GaInSn, brass, aluminum, and copper) at fixed position ( $Y=25$ ). Both amplitude and phase can be indication of different conductivity following particular location along horizontal (frequency) axis. Peak values are the indicator on amplitude spectrum; whereas zero-valued lines across spatial (vertical) axis are the marker on phase spectrum.



(a)



(b)

Figure 5-19: Spectral gradient impedance images  $df$  of (a) amplitude  $Z$  and (b) phase  $\theta$  for metallic samples with size variations. Bottom to top are aluminum  $d = 0.25$  inch, and aluminum  $d = 0.5$  inch



Spectral gradient for aluminum rod with different diameter (small = 0.25 inch, big = 0.5 inch) at the centre region is plotted in Figure 5-19. While it is not straightforward from locus spectrum, the size variations can be inferred from the area of high-valued pixels. Larger area is associated with a larger sample and vice versa.

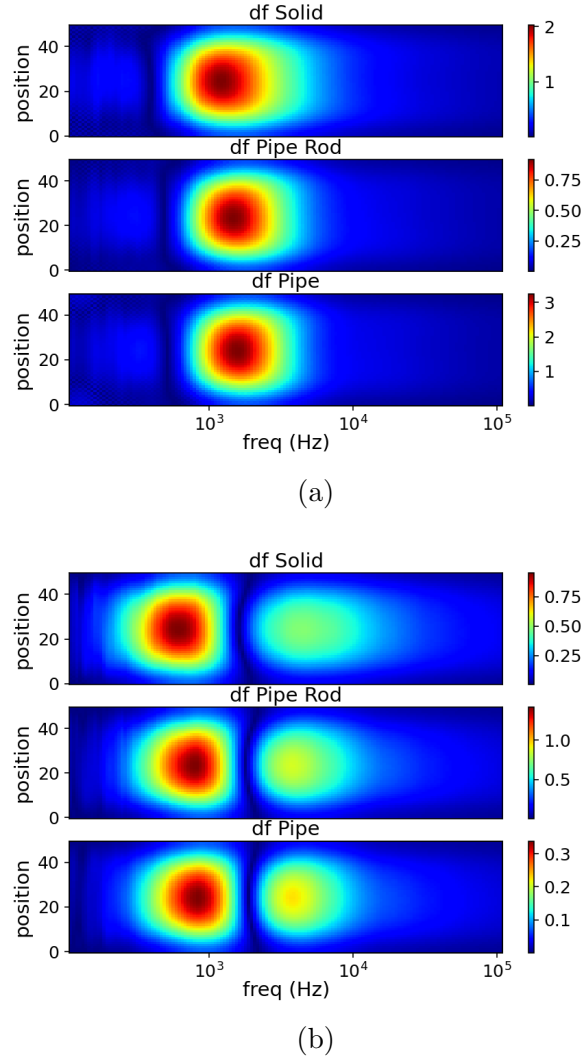


Figure 5-20: Spectral gradient impedance images  $df$  of (a) amplitude  $Z$  and (b) phase  $\theta$  for metallic samples with structure variations. Bottom to top are aluminum pipe id = 0.4 inch od = 0.5 inch, aluminum pipe id = 0.4 inch od = 0.5 inch with aluminum rod d = 0.25 inside, and aluminum rod d = 0.5 inch

Three different structures are arranged from the same material (aluminum): pipe

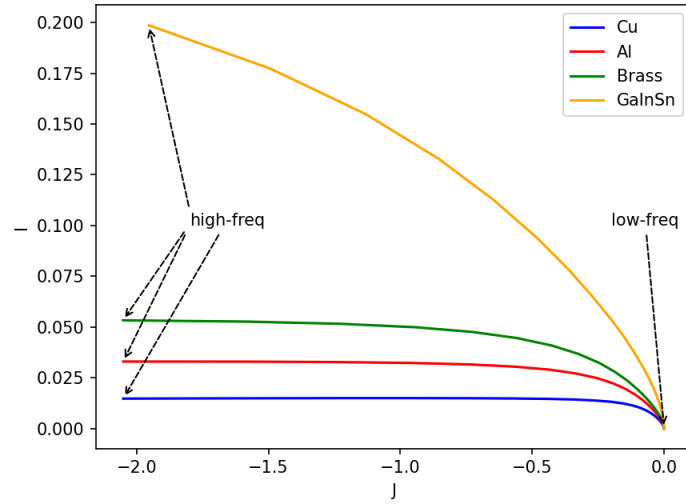
(hollow cylinder with outer diameter 0.5 inch and inner diameter 0.4 inch), pipe with 0.25 inch solid rod inside, and solid rod 0.5 inch. In the experiment, they are fixed at the centre ( $Y=25$ ) of sensing region. Figure 5-20 shows the respective gradient of amplitude and phase spectrum.

### 5.3.5 Complex Plot of Normalised Impedance from Reconstruction

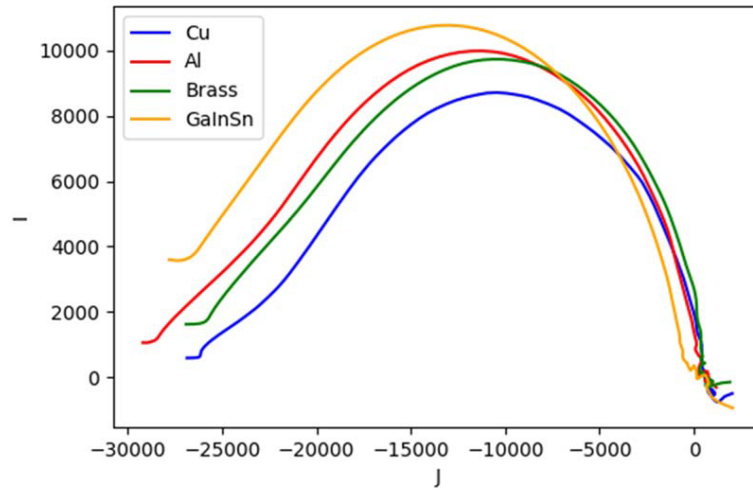
Analogous to Cole-Cole model [163] and dielectric spectroscopy [164], complex plots are also generated using reconstruction values to represent the behaviour. Region (group of pixels) making up the object is chosen for every investigated case where real and imaginary parts of the image are taken into account. Mean of pixel values in the region produces the following complex plots.

Real and imaginary parts of measurement data are collected for a number of frequencies. The data are then reconstructed producing real and imaginary images. Since object's location in the sensing space ( $X, Y$ ) is known, object's region in the resulting image ( $50 \times 50$  pixels) can be determined. Pixels values of that region are then taken for analysis. Real and imaginary image values can be formed as a complex plot. Due to the measurement data are relative against reference/background, the complex values represent normalised impedance.

Figure 5-21a illustrates how the plot is configured. These reference values are taken from measuring coils in COMSOL simulation (see setup in Section 3.1) using objects with different conductivity. The graph indicates different levels for different conductivity. Low-frequency point is annotated and usually lies near or about the origin  $(0, 0)$ ; whereas high-frequency point lies on the second quadrant. It is expected that complex plots for the studied cases follow similar trend.



(a)



(b)

Figure 5-21: Complex plot of normalised impedance for metallic samples with conductivity variations: (a) simulation reference (b) experiment

It can be seen from Figure 5-21b that metallic samples with different conductivity levels have similar shapes with different foci and vertices in the impedance plane. Here one can allocate the horizontal axis  $J$  for imaginary value; the vertical axis  $I$  for real value. The plot starts from lower frequency near the origin (0,0) and curves to high frequency at the other end.

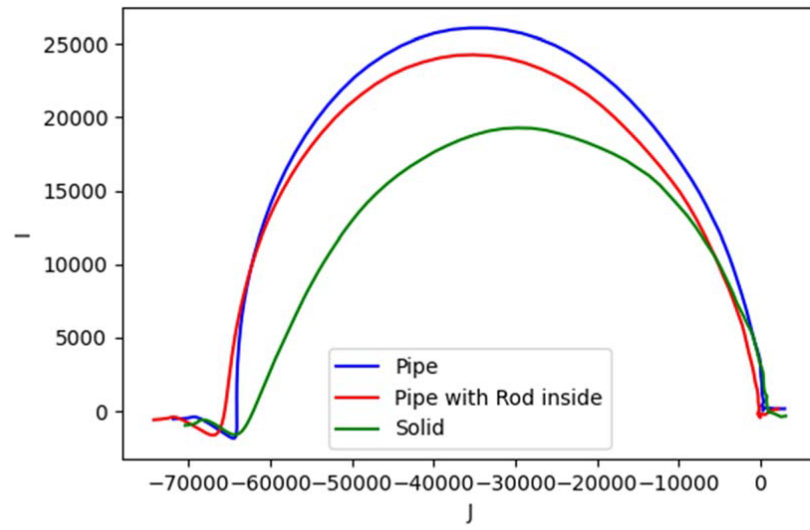


Figure 5-22: Complex plot of normalised impedance for metallic structures.

Figure 5-22 represents structural circumstances of the aluminum body. The complex plots have the same shapes with increasing vertices. Solid structure has the lowest vertex and the nearest focal point relative to the origin; while pipe structure has the highest vertex. The vertex level of pipe with rod is between that of solid and pipe, but it has the farthest focal point.

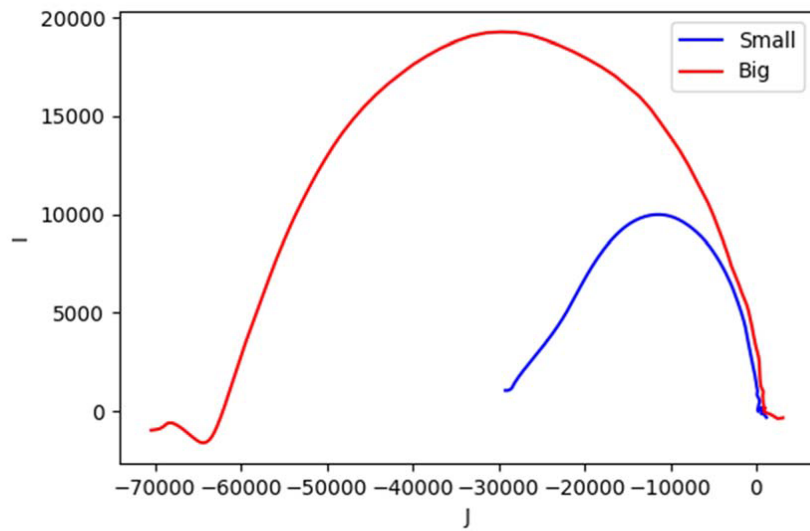


Figure 5-23: Complex plot of normalised impedance for size variations.

As for size variations (aluminum with diameter of: small = 0.25 inch, big = 0.5

inch), Figure 5-23 shows an obvious difference on the curves' size.

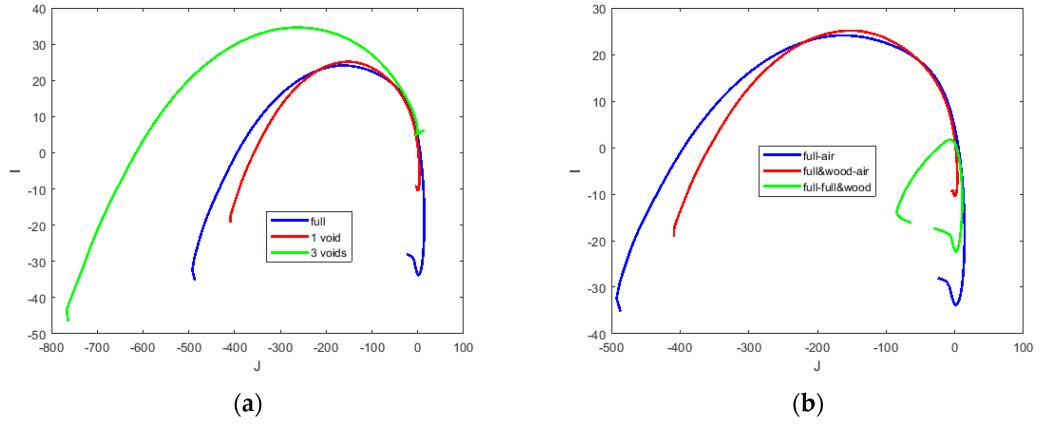


Figure 5-24: (a) Complex plot of normalised impedance for inclusions; (b) focusing on 1 void but various background data

The complex plot for conductive liquid GaInSn with void distribution is depicted in Figure 5-24a. It is shown that although the curves' shape are similar due to the embodiment of liquid metal, the level and inclination are varied for a single void and three distributed voids respectively. This corresponds to the setup in Subsection 5.3.3. Focusing on 1 void a wooden cube inside of liquid metal, one can depict the cole-cole plot in three set of data, one pure metal from air background, one wood and liquid metal from air background, and finally liquid metal when the reference data is liquid metal including wooden block. Figure 5-24b shows various plots in these three situations.

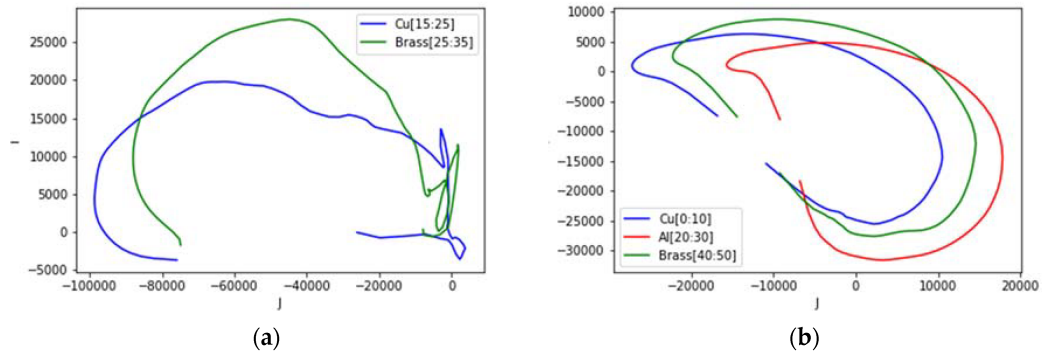


Figure 5-25: Complex plot of normalised impedance for different samples at different locations

The circumstances in Subsection 5.3.2 are plotted in Figure 5-25, taking the position of the sample in sensing region and evaluating their values in the confined area. For two different samples (5-25a), the plot shows each curves that follow the trend in Figure 5-21 (copper and brass). However for three samples (5-25b), the curves are tilted to the side, still each focal and vertex are consistent with the trend for samples with different conductivity levels.

## 5.4 Discussion

This chapter shows the introduction to a spectrally correlative MITS using both amplitude and phase data. Image reconstruction is plotted along a wide bandwidth with sufficient resolution, and its frequency derivative is exposed. Samples with conductivity, size, location, and internal structure variations have been investigated.

Using experimental apparatus based on LCR meter, high-frequency measurement is sufficiently accurate. However, noisy data occur at lower frequency due to the setup imperfection. This causes non-smooth complex plot in the beginning of traces. Nevertheless, by considering overall traces from low-to-high frequency, the result still can identify the object's circumstance. The data can be used to identify metal types and sizes given that a reference condition or object is available to be measured.

When a lower conductive sample such as GaInSn is mixed with a non-conductive sample, the signature frequency is pushed to a bit higher. Therefore, if lower conductive metals are of interest, the measurement must go to a higher frequency range to capture that effect. As opposed to more conductive contrast (i.e. aluminum structure variations), the result shows that is not the case as aluminum is much more conductive relative to the inner structure (air).

Although the author used a TV (in fact a spectral TV), which normally gives a sharp and clear image, in this iterative TV process the author did not aim for a very sharp (near binary) image. The reason for that is if one gets a very sharp boundary, one starts losing quantitative consistency with measured data. So hence the TV is a good choice that gives a good balance between the image quantitative information and shapes. Image quantitative information is key in

this study as they form the basis of the complex plots. Having said that, for future study more work needs to be done on hyperparameter tuning as when dealing with complex data and images. Also for this wide frequency range, it is challenging to assign a parameter set that works very well in all these ranges. In this study, one had to maintain these parameters uniform so that one could produce reliable quantitative values. The same can be said for the measured data, future studies will need to evaluate the noise performance for different frequencies, which may vary for real and imaginary parts.

## **5.5 Conclusion**

The work proposes the spatio-spectral method to characterise a metallic object in terms of electromagnetic and structural properties. The algorithm is explained and supporting experimental works are described. The author has also presented complex plots from reconstruction which comprehensively indicate functional and structural behaviors in the metallic materials. This research is contributive in the context of eddy current, imaging, and induction spectroscopy of materials as significant information for characterisation techniques.

## Chapter 6

# Conductivity and Temperature Sensing

This chapter presents a perspective in evaluating electromagnetic tomography reconstruction through a spectral eddy current imaging arrangement. Embarking from an established analytical basis, the spectroscopic relation of a metallic conductive body to its physical properties is revealed via multi-frequency mutual impedance measurement. Characteristics are evident, from either modelling or experiment, on certain frequency ranges that discriminate the object's circumstances. Both the amplitude ratio and phase-contrast image spectrum show information on the conductivity and structure of a target considered pivotal for industrial applications. Two test cases will be investigated: liquid metal structure determination, and contactless temperature evaluation of a remote/hidden medium/object.

### 6.1 Introduction

Industrial sectors demand decisive information for supervision, quality assessment, as well as regulating a process. Inductive measurement has several desirable advantages, such as remote sensing technique, non-intrusive, sturdy operation, etc. In addition, multiple frequencies data contain important characteristics of the measurand, particularly a conductive body. Distinctive patterns are known



for conductivity level and target's size [165], [166]. As a consequence, this instance has inspired various implementations.

The spectrum of electromagnetic induction was applied for identification of buried conductive and/or permeable landmines independent on the depth or orientation. Therefore, the identification is only based on spectral shapes where the object's signature can be obtained [167], [168]. The recent implementation of magnetic spectroscopy for mine detection was also proposed in [169]. Furthermore, the method was referred for classifying non-ferrous metal waste to be recovered based on its purity [150]. On the other hand, inversion of induction spectroscopy measurement into conductivity distribution image form was among interesting research. The work disclosed in [142] offers an ability to extract depth and internal profile of the target.

For liquid metal flow, multi-frequency inductive measurement could provide an identification necessary to determine non-conductive distribution embedded in conductive steel jet. The presence of gas bubbles (deliberately injected to prevent clogging and remove impurities) disrupts the induced eddy current more profoundly in higher frequency. The test reported in [16] correlated a frequency crossover point that discriminates between annular and bubbly liquid metal flow. This peculiar feature has not been exploited further to distinguish different flow regimes.

Correspondingly, the observation of temperature profile of hot steel inside the billet has been attempted. Internal map of electrical conductivity which is related to the measurement of the solid, mushy and liquid layers was reported [92]. The study synchronises the MIT and the thermal map from the actual process parameters. This paves prospective research on temperature reconstruction based on conductivity detection through magnetic induction. Moreover, the possibility will enhance the development and application of temperature measurement technologies [170].

The response of conductive objects toward magnetic field excitation over different frequencies is picked up as induction spectroscopy data. This work makes use of those facts to propose tomographic images based on electromagnetic induction and illustrate them in spectroscopic fashion exposing electrical properties and

physical circumstances of a target for further interpretation. Spectral imaging can provide useful features to leverage more advance practices.

## 6.2 Method

The ratio of absolute mutual impedance (presence of conductive object against air background) plots a sigmoid shape along the frequency to converge at an asymptote; whereas phase change curves down to an extreme point before bouncing back towards zero as frequency increases. The straightforward explanation is associated with skin-depth phenomena, that is the eddy currents tend to buoy towards the surface and ultimately stick there at a higher frequency. Consequently, the response field is invariant to the object's conductivity (penetration depth is negligible) and staying in-phase with the excitation field.

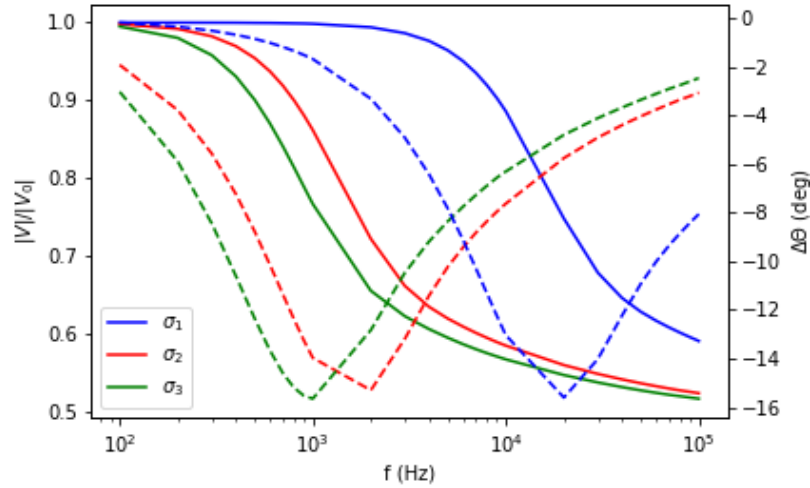


Figure 6-1: Behaviour of conductive body as function of induced voltage and frequency. Amplitude (—) and phase (- -); conductivity  $\sigma_1$  (blue) =  $0.1\sigma_2$  (red) =  $0.05\sigma_3$  (green).

Modelling in COMSOL is utilised to solve electromagnetic field problem of coil combinations [171], and simulated to preliminarily confirm the aforementioned. A pair of coils (solenoid) are modelled as the exciter-detector arranged opposite (axial distance 15 mm) to each other. A cylinder sample (diameter 7.5 mm) is placed in between coils, in such a way that the cylinder's axis is perpendicular to

the coils' axis. The exciter coil is injected by a unit ac current in frequency sweep mode (100 Hz – 100 kHz), and the induced voltage at the detector coil is recorded for each frequency. The reference voltage ( $V_0$ ) is the induced voltage when the measurement is taken without the conductive sample (air background); whereas  $V$  is induced with the presence of the sample. Figure 6-1 shows amplitude (left y-axis, solid line plot) and phase (right y-axis, dashed line plot) of induced voltage when the cylinder object's conductivity is varied ( $\sigma_1 = 3$  MS/s,  $\sigma_2 = 30$  MS/s, and  $\sigma_3 = 60$  MS/s) relative to air ( $\sigma_0 = 0$ ).

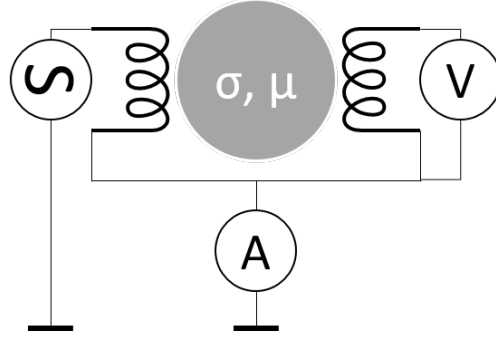


Figure 6-2: Mutual impedance measurement scheme.

The measurement scheme is depicted in Figure 6-2 [172]. Pair of transmitter and receiver coils (2200R, Murata Power Solutions,  $L = 220 \mu\text{H}$ ) are arranged to face each other (separating distance of 20 mm, with effective sensing space of 15 mm) in which an object will be placed midway between them. The transmitting coil is excited by a current source to generate a magnetic field that will be picked up by the receiving coil. The induced voltage at terminals of receiving coil can be sensed as a function of the primary field from the transmitter as well as a secondary field depends on any perturbation exists in the sensing area. Eddy currents will occur on conductive samples from which some information about the object in question are carried by the secondary field relative to the primary field.

In the experiments, the transmitter coil is injected with 10 mA source in frequency sweep procedure; while the receiver coil is being sensed by measuring bridge (E4980AL Precision LCR Meter, Keysight Technologies). The four-probe method is used to directly measure a mutual impedance between coils [173]. Both amplitude and phase are acquired which represent resistive and inductive com-

ponents. The effect of parasitic capacitance is suppressed by prior calibration and a commonly grounded screen placed in the outer perimeter of the sensors.

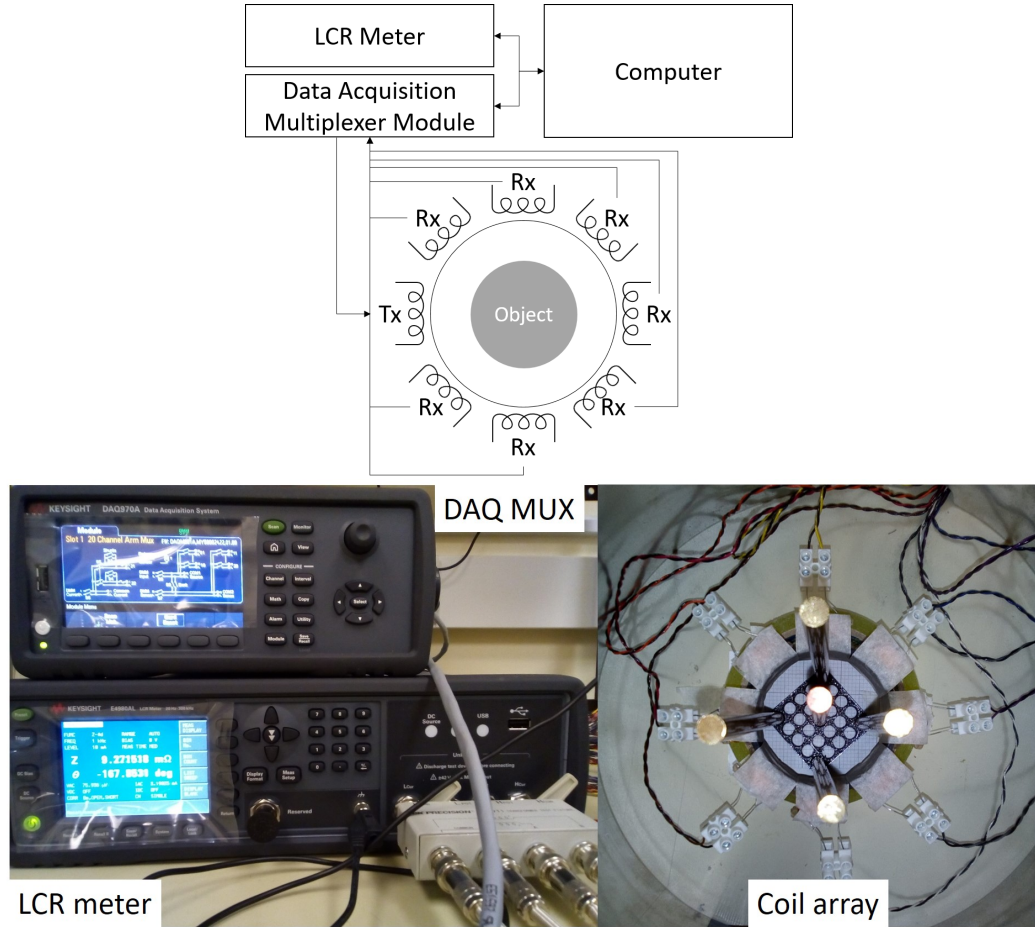


Figure 6-3: Multi-channels setup for tomographic projection system.

The two-coil system in Figure 6-2 is extended into multi-channel measurements setup (Figure 6-3) via computer-controlled data acquisition (DAQ970A Data Acquisition System, Keysight Technologies) and multiplexer (DAQM901A 20 Channel Multiplexer Module, Keysight Technologies) providing a projection system for the tomographic purpose. The setup is capable of scanning up to 28 –the combination of 8 coils taken 2 (a pair) at a time without repetition– independent rotational measurements; each of which acquires impedance values over frequency scope from 20 Hz to 300 kHz.

The direct induction effect is eliminated by taking amplitude ratio and phase difference of measurement with an object to a respective free-space measurement.

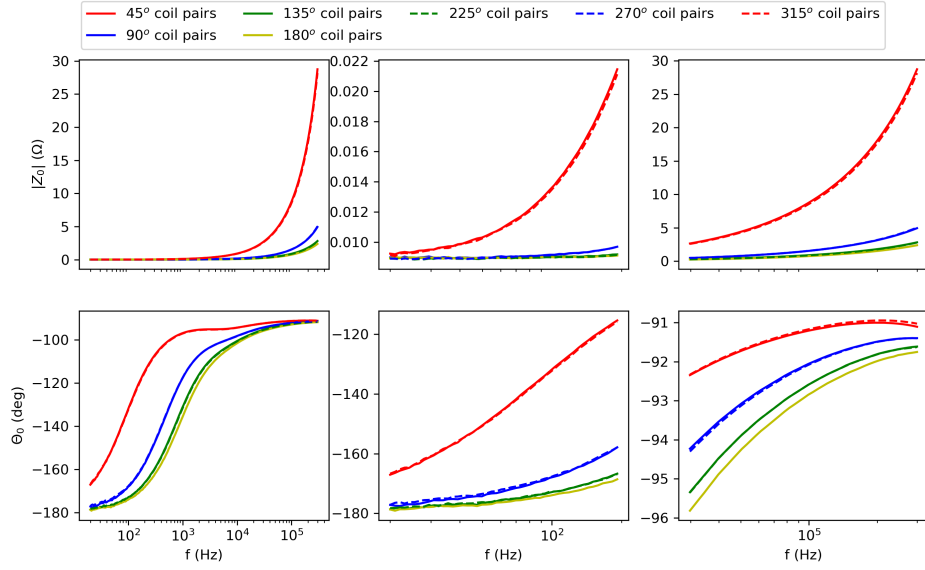


Figure 6-4: Reference measurement of amplitude (top) and phase (bottom) for 28 Tx-Rx pairs with zoomed view at low and high frequencies for both graphs.

Figure 6-4 depicts the reference measurements for seven basic coil pairings. Measurements from nearby Tx-Rx pairs (see Figure 6-3) have relatively higher values than those from far pairs.

An example of MIT image is shown in Figure 6-5. The spatial region is divided into 50x50 pixel with effective circular area of 1976 pixels. Experimentally seen in Figure 6-3, five metal samples are placed in the sensing space ( $d_{sample} = 6.25$  mm;  $D_{space} = 60$  mm), four of them (grey) have lower conductivity ( $\sigma = 16$  MS/m) than an object in the middle (black,  $\sigma = 58$  MS/m). Positions refer to the sensing space (Figure 6-3) which is mapped into pixel image shown in Figure 6-5. Pixel values are unitless normalised values representing conductivity level qualitatively. The algorithm described in Subsection 3.2.1 is used here. As expected in soft-field tomography, region near the sensors poses a higher sensitivity compared to central region, and reflected on the resulting image.

Single-frequency measurement at 10 kHz (averaging ten datasets) is taken. This example is intended to show an overview of spatial (cross-section) image. In the subsequent spectral imaging, where reconstruction is being done for each frequency separately, the pixel values from  $X_{position} = 1$  to  $X_{position} = 50$ , across

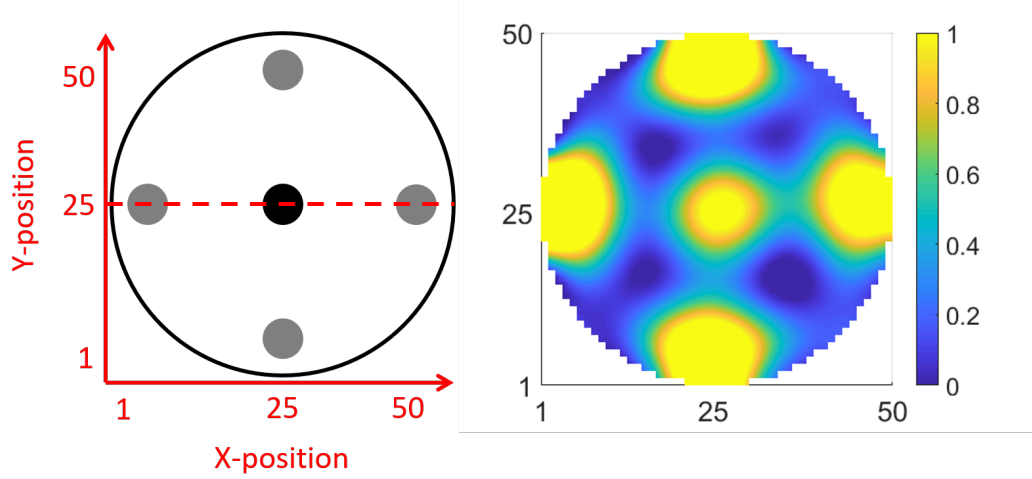


Figure 6-5: Spatial arrangement of objects in the sensing region; and example of MIT image from experiment with five metal rods.

$Y_{position} = 25$  plane are evaluated (indicated by dashed red-line). This constitutes spatial 'position' axis (vertical) against frequency axis (horizontal) in the 'surface plot' of the spectrum.

## 6.3 Spectroscopy

### 6.3.1 Mutual Impedance on Conductivity Level

Mutual impedance spectrum against air background measured from 20 Hz to 300 kHz (200 data points in logarithmic fashion) is shown in Figure 6-6. Different samples with different conductivity produce sigmoid pattern where the inclination shifts to the left as conductivity increases.

Phase spectrum against air background is similarly swept in the frequency range (Figure 6-7). Different samples with different conductivity produce bell pattern where the extreme valley shifts to the left as conductivity increases.

Both plots are produced from opposite coil measurement (setup Figure 6-2) and consistent with modelling result (Figure 6-1), taking into account a variation of conductivity values listed in Table 6.1.

Conductive samples are commercially available and comply with their standards

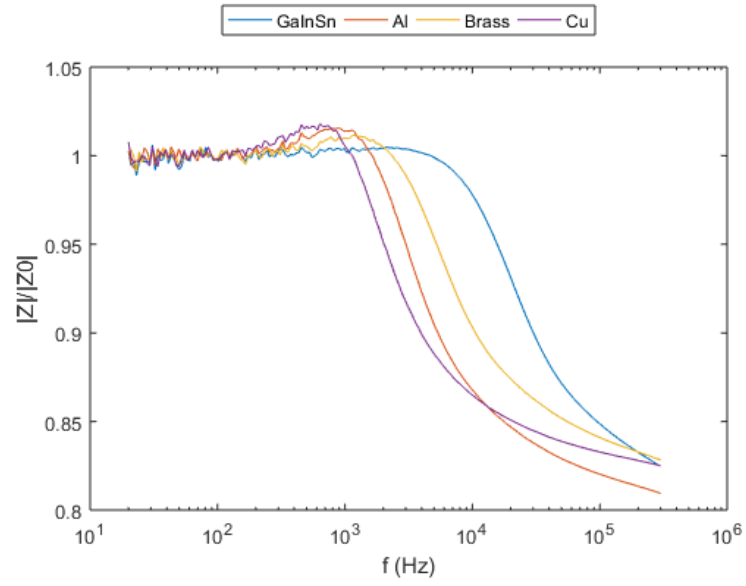


Figure 6-6: Mutual impedance spectrum conductive samples 0.25 inch placed at the centre of the sensing space.

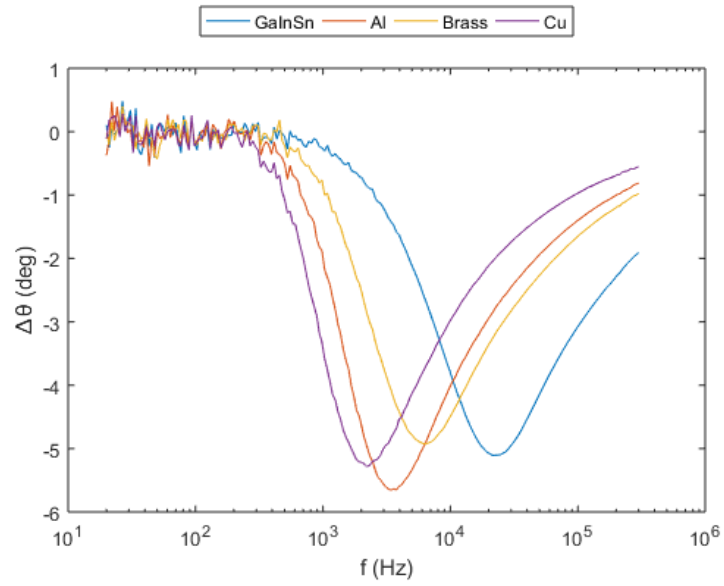


Figure 6-7: Phase spectrum conductive samples 0.25 inch placed at the centre of the sensing space.

Table 6.1: Conductivity of Tested Objects

Sample	$\sigma$ (S/m)
Liquid GaInSn	$0.32 \times 10^7$
Brass	$1.61 \times 10^7$
Aluminum	$2.63 \times 10^7$
Copper	$5.84 \times 10^7$

and specifications, i.e. GaInSn eutectic alloy [114], brass rod (BS2874/CZ121M (1986); BS EN 12164/CW614N), aluminum (Al) rod (BS1474 HE30 TF (1987); BSEN 754-5 608 2T6), and copper (Cu) rod (BS2874/C101 (1986); BS EN 12164 CW 004A).

### 6.3.2 Mutual Impedance on Conductive Structure

The similar setup in Subsection 6.3.1 is implemented for three different conductive structures. Plastic (PLA) containers are prepared to hold liquid metal GaInSn in full, annular (50% area is hollowed in the centre), and bubbly (three voids each occupies 25% area distributed inline axially).

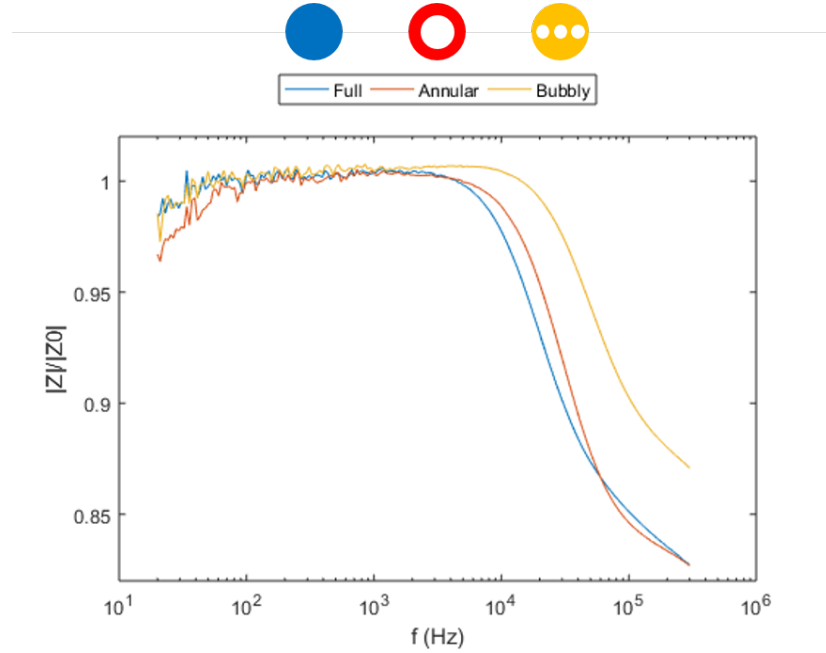


Figure 6-8: Mutual impedance spectrum conductive structures.

Figure 6-8 shows that the same material with different structures produces a



sigmoid pattern. The curves for full and annular condition are close to each other and having intersection point at a certain frequency. Meanwhile, for bubbly case, the tendency in the curve is as though there was a decrease in conductivity, and the asymptote has a higher value.

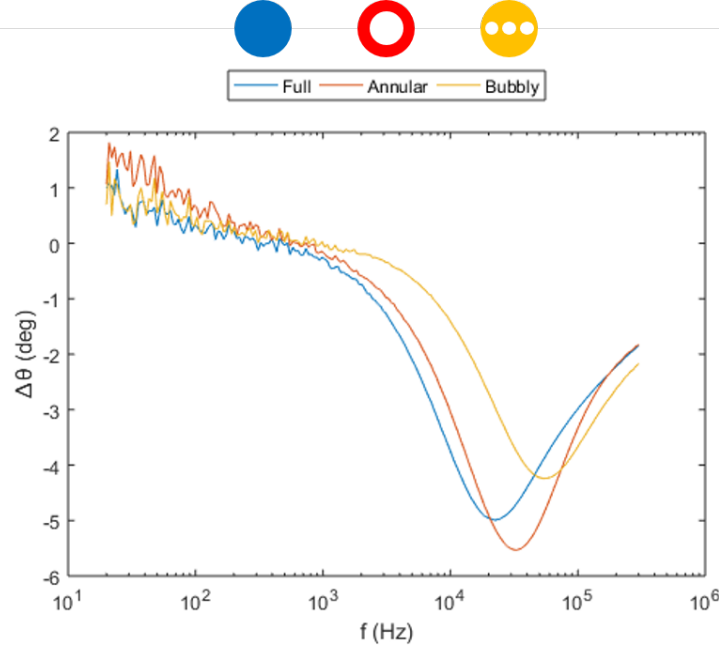


Figure 6-9: Phase spectrum conductive structures.

Phase spectrum is shown in Figure 6-9. Same material with different structures produces a bell pattern. The extreme valleys shift as though there was a decrease in conductivity level. The position of the valleys in y-axis also changes, while annular structure goes lower; bubbly structure goes higher.

### 6.3.3 Spectral Imaging of Mutual Impedance

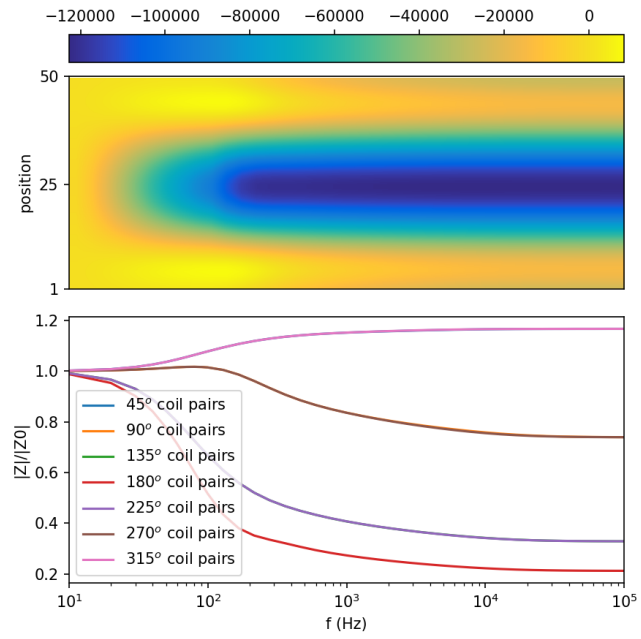
Mutual impedance and phase spectrum measurements are collected for seven coil-pairs in a circular array consisting of eight coils. The coil array is arranged enclosing the object in the sensing area (see Figure 6-3). For a cylindrical object, full tomographic sensing is obtained by virtually rotating the coil array  $45^\circ$  counter-clockwise in each step. Therefore, a sufficient number of independent measurements are acquired to be reconstructed as an image for every frequency data.

The images are reconstructed using the technique (Tikhonov) described previously in Chapter 3. Simply, single-step reconstruction with neighbouring matrix and regularisation parameter of order  $10^{-12}$  are used in this work. Resulting images are then piled to construct a whole spectral image. In this way, the horizontal direction of the image represents frequency; whereas vertical direction is spatial location. An example of aluminum rod half-inch of diameter produces mutual impedance and phase spectrum as shown in Figure 6-10 and Figure 6-11 respectively. Surface plot (top) in the figures is the spectral image, while semi-logarithmic plot (bottom part) is the associated measurement data. Each line plots measurement between transmitter-receiver coils paired to a certain degree. Both surface and semi-log plots share the same frequency axis.

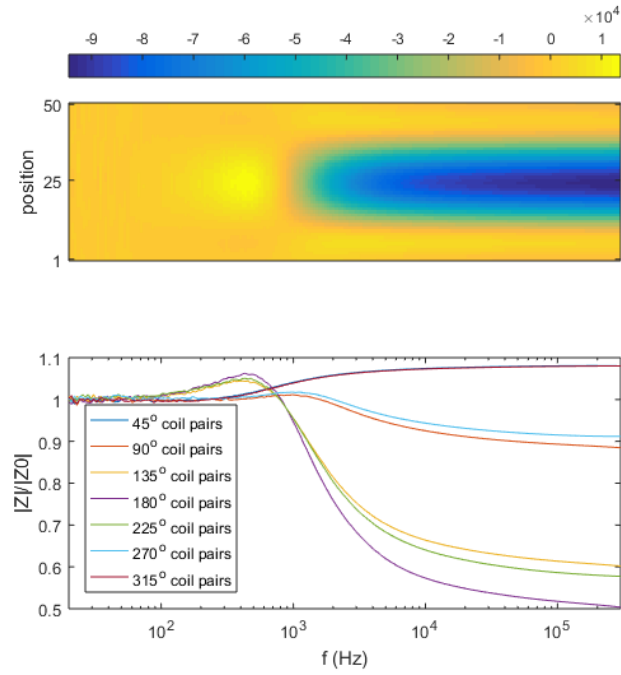
The positions refer to scheme in Figure 6-3. Part (a) of the figures are based on COMSOL simulation (see setup in Section 3.1), and part (b) are based on experiment. There the trend is similar. Although in the simulation, received voltages from equally spaced coil pairs (e.g.  $45^\circ$  and  $315^\circ$ ) are exactly match; whereas in the experiments they have slightly different values. Furthermore, the frequency location is different. This might be caused by the difference between conductivity value set in simulation and actual conductivity of the object in the experiment.

Mutual impedance for seven coil-pairs gives familiar sigmoid patterns where inclinations lie on certain frequency indicating conductivity characteristics found in measurement (see Subsection 6.3.1). The amplitude spectral reconstruction shows image patterns (centre area at pos=25 where the object is placed) starting from a high-contrast value (at low frequency) and finishing with low-contrast value (at high frequency).

Similarly, phase change for seven coil-pairs produces bell shapes where extrema occur on specific frequency from which conductivity level can be inferred. The phase spectral image depicts high-contrast value (at the beginning), then down to low-contrast value (midway), and end-up back with high-contrast value. In other words, there is a gradient change of images along with the frequencies. Note that all colormap scales/values are qualitative resulting from the inverse calculation (affected by parameters and Jacobian), hence the interpretation of which is another subject for the future work.

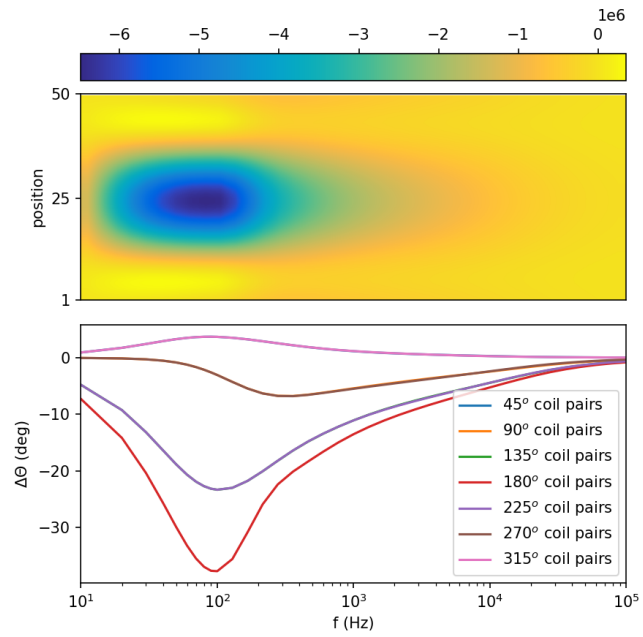


(a) Simulation

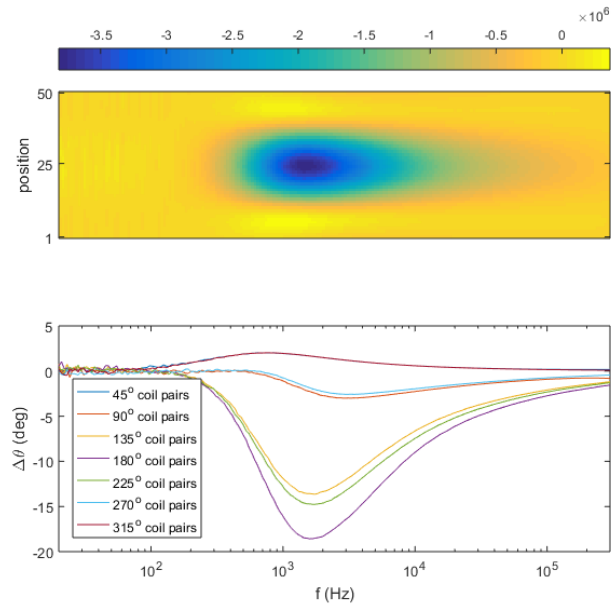


(b) Experiment

Figure 6-10: Mutual impedance spectrum aluminum rod 0.5 inch. Top: spectral image at spatial position against frequency. bottom: measurement plot. Both share common horizontal frequency axis.



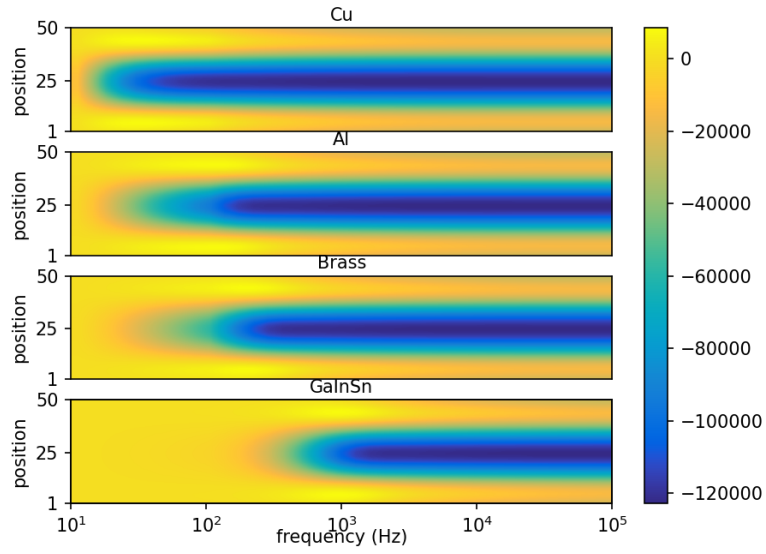
(a) Simulation



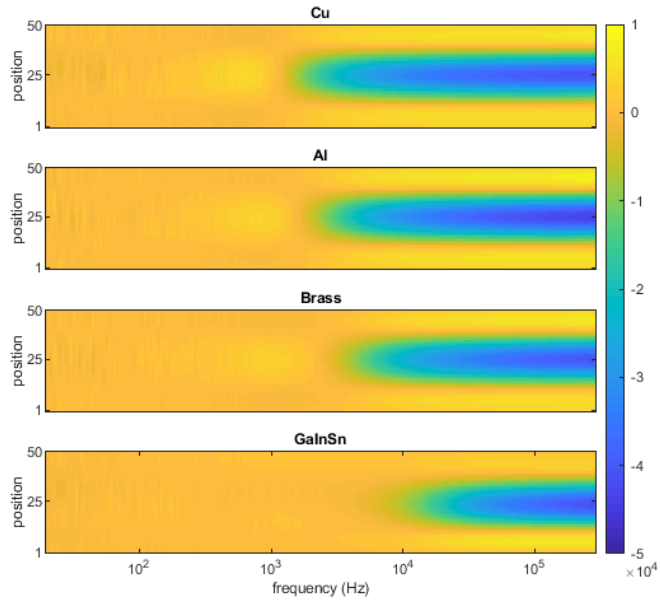
(b) Experiment

Figure 6-11: Phase spectrum aluminum rod 0.5 inch. Top: spectral image at spatial position against frequency. Bottom: measurement plot. Both share common horizontal frequency axis.

In order to obviously show the fingerprints of each object's circumstances, mutual impedance spectrums are compiled in a single plot. They are arranged as follows: four individual images of four different samples are taken, with the sample with the highest conductivity at the top and the sample with the lowest conductivity at the bottom ( $\sigma_{Cu} > \sigma_{Al} > \sigma_{Brass} > \sigma_{GaInSn}$ ). In the measurement, the object is located at the central location (pos = 25) in the sensing space. All plots share the same frequency (horizontal) axis. Figure 6-12 and Figure 6-13 show shifting colour contrast to lower frequency as conductivity level increases.

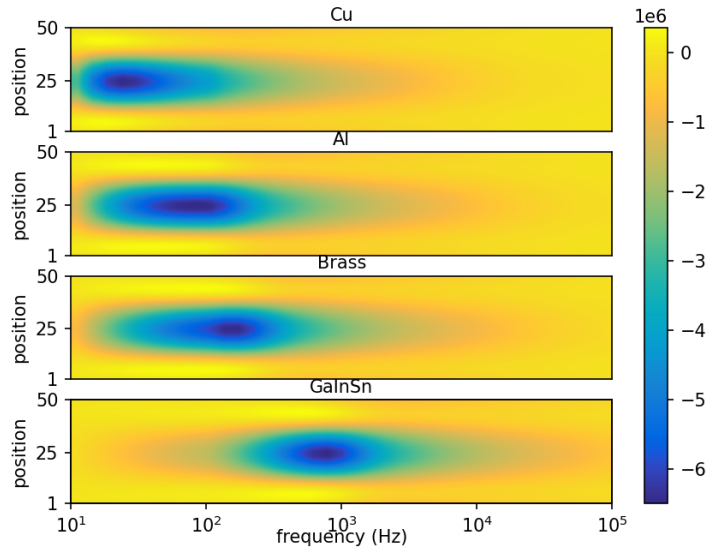


(a) Simulation

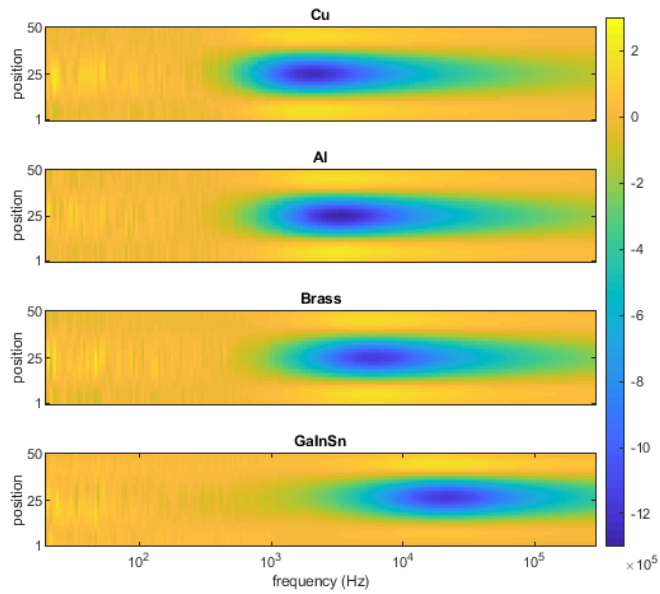


(b) Experiment

Figure 6-12: Mutual impedance spectrum imaging conductivity. Individual samples ( $d = 0.25$  inch) are exposed. Each plot (top-to-bottom): Cu ( $\sigma = 58.4$  MS/m), Al ( $\sigma = 26.3$  MS/m), Brass ( $\sigma = 16.1$  MS/m), GaInSn ( $\sigma = 3.2$  MS/m). All plots share common horizontal frequency axis.



(a) Simulation



(b) Experiment

Figure 6-13: Phase spectrum imaging conductivity. Individual samples ( $d = 0.25$  inch) are exposed. Each plot (top-to-bottom): Cu ( $\sigma = 58.4$  MS/m), Al ( $\sigma = 26.3$  MS/m), Brass ( $\sigma = 16.1$  MS/m), GaInSn ( $\sigma = 3.2$  MS/m). All plots share common horizontal frequency axis.

## 6.4 Application

The aforementioned techniques are applied in the following two scenarios. Subsection 6.4.1 explains a case of liquid metal inclusion which is of interest in the steel casting process. For the conventional method, field distribution in the case of complex structure is less definite [174]. Another describes contactless temperature measurement utilising the conductive body as an agent through which the magnetic induction method is capable of sensing the temperature change and mapping its distribution according to conductivity variation. Electromagnetic methods for thermography are well-known such as infrared and magnetic resonance [175]. While an electrical resistance device and capacitance thermometry offer invasive technique, the inductive method provides a non-contact solution.

### 6.4.1 Inclusion in Liquid Metal

Experiments are conducted using liquid metal (GaInSn) as a conductive sample that is detectable by multi-frequency impedance and phase measurements. Figure 6-14 shows the measurement setup. The coil arrays are made from eight air-cored solenoids (8 mm height, 25 mm outer diameter, 10 mm inner diameter, 23 AWG wire, 100 turns) encircling 60 mm diameter of the sensing area. A grounded aluminum sheet (150 mm height, 250 mm diameter, 1 mm thick) is placed around the perimeter. As a result, the ambient noise, especially in lower frequency is reduced.

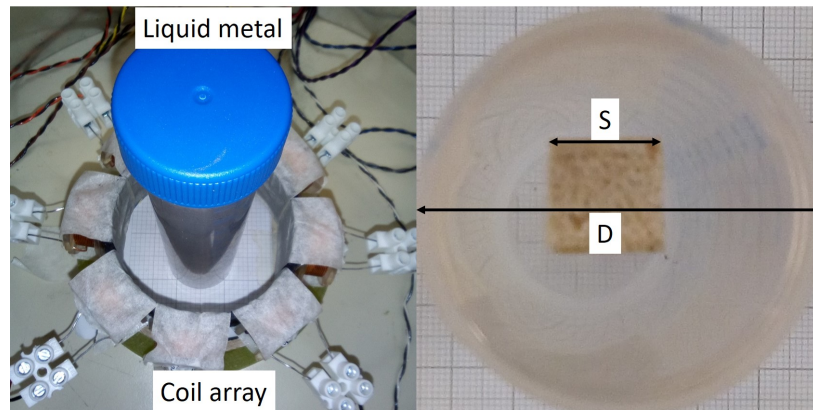


Figure 6-14: Experiment setup for liquid metal inclusion.



Firstly, impedance and phase are measured for 1 inch of diameter ( $D$ ) plastic tube fully-filled with the liquid metal and plotted against air background. The plot is then considered as the reference for subsequent measurements where a non-conductive inclusion is introduced in the liquid metal body. It is assumed that the insertion of non-conductive material will disrupt the eddy current distribution which occurs freely on the full liquid metal circumstance. Therefore, the overall conductivity of the body is expected to change and a shift should be apparent around extreme points in the mutual impedance and phase graphs.

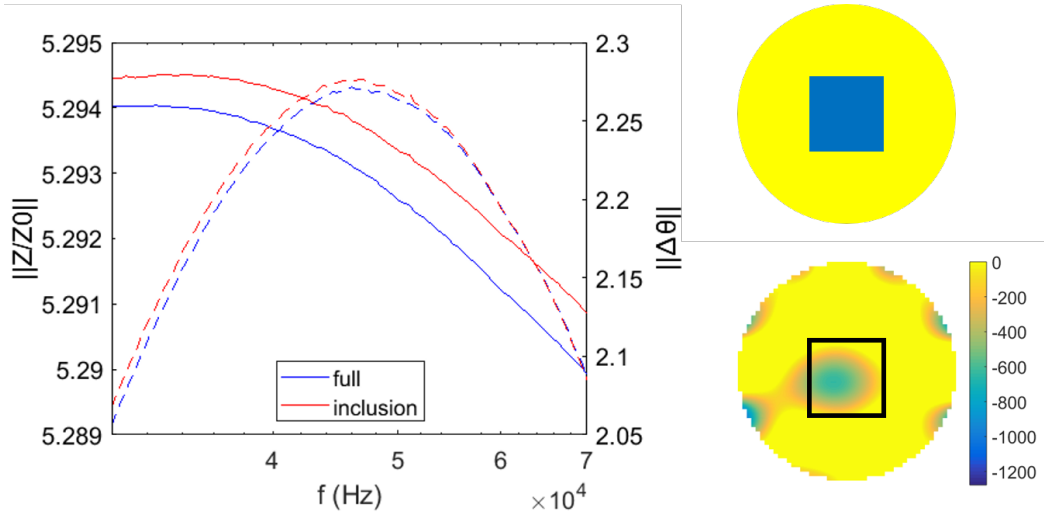


Figure 6-15: Mutual impedance liquid metal inclusion. Left: impedance plot (—) on left axis; phase plot (- -) on right axis. Right: inclusion true distribution (top) and reconstructed image (bottom).

A squared wood (balsa) with size of 9.5 mm ( $S$ ) is immersed in the test. It can be seen from graph in Figure 6-15 (left) that an inclusion will shift the plot. Since the inclusion's precise location is unknown due to opacity of the liquid metal, all mutual combination between 8-coil arrays are measured, and norm values are taken. Note that this method does not necessarily require low-frequency measurement to penetrate conductive samples in order to detect an inclusion inside them. As a result, the frequency region can be contained into a range of interests based on the fundamental plot for liquid metal GaInSn.

Cross-section true and constructed images are shown in Figure 6-15 (right). The colour bar represents unitless normalised values representing conductivity level relatively. Image reconstruction produces good consistency along the spectrum

of interest. Therefore, mean values are applied here to illustrate inclusion's image (non-conductive) and its location (black line border) inside the liquid metal. Quantitative analysis in spatial imaging is used to evaluate the liquid metal correlation coefficient (0.63) and area error of 0.16 which are in an acceptable agreement with the true distribution.

### 6.4.2 Temperature Sensing

Certain phenomena are dependent on temperature, hence exploitable for instrumentation. Making use of the renowned physical properties that is the resistivity of a material is a function of its temperature, multi-frequency mutual impedance and phase can also be employed for indirectly sensing the change in the temperature of a medium surrounding a conductive body. This is applicable when the conductive body and the medium exchange heat, unisolated towards one another.

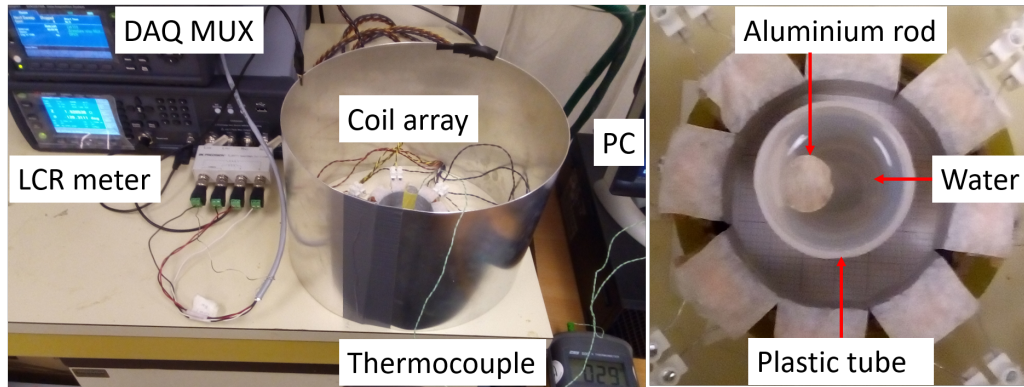


Figure 6-16: Experiment setup for temperature sensing.

The experiment setup is shown in Figure 6-16, with the same coil array and sensing space as described in Subsection 6.4.1. A metal sample (Al rod) is prepared in a container filled with water, in the centre of coils. Mutual impedance and phase between coil combinations are measured. Water temperature is varied from cold to hot condition and measurements are taken in cycles, keeping the object intact in the sensing region. The temperature is tested using a thermocouple (CHY 500 K) before and after each mutual impedance measurements cycle in order to avoid the influence of magnetic fields on the thermocouple probe and vice versa. It takes approximately 10 minutes to collect a complete cycle of measurement.

Multi-frequency graphs are plotted (norm, against air background) showing distinct shifts for different temperatures in Figure 6-17 (left). Note that the plot composes from two setups, i.e. cold (up to 20 °C) and hot (from 25 °C). Having different background measurements and the relative position of the metal sample in the water medium, a slight change in trend is anticipated.

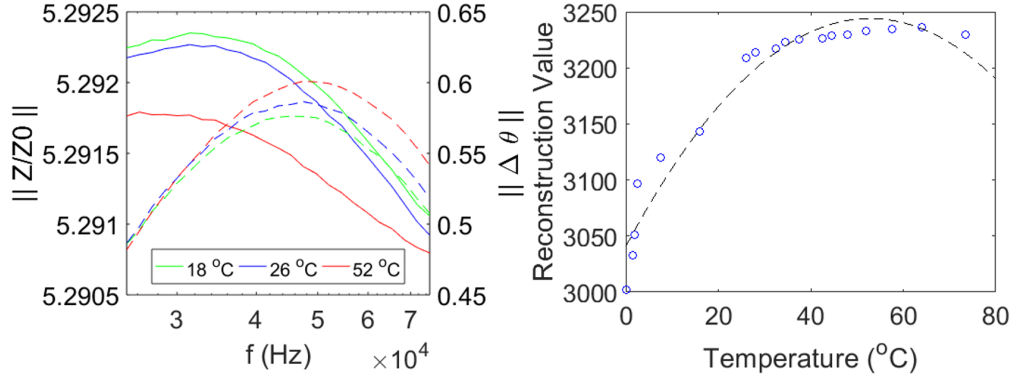


Figure 6-17: Mutual impedance temperature sensing. Left: impedance plot (—) on left axis; phase plot (- -) on right axis. Right: reconstruction value against temperature.

Both impedance and phase plots indicate the change of the sample's conductivity confirming the change of water's temperature. The frequency range where extreme values and pronounce shifts lie can be taken as measurement reference for more complex detection scheme. Operating norm on 28 measurement values can produce resulting value greater than 1. It should be noted that experiments with water-only were conducted beforehand with negligible values compared with the presence of a metal object.

The data are then converted into imaging domain for assessing the correlation between reconstruction value and temperature change, giving the trend shown in Figure 6-17 (right). This can be derived as:

$$y = p_1x^2 + p_2x + p_3 \quad (6.1)$$

where the quadratic fit coefficients are:  $p_1 = -0.072838$ ,  $p_2 = 7.6959$ ,  $p_3 = 3040.8$ ; whereas norm of residuals = 72.736. The reconstruction values are calculated from the mean of unique numbers across the image sections. Equation (6.1) is also affected by regularisation parameters of the image reconstruction, thus can

be used as calibration function.

A complete two-dimensional tomographic heat mapping is attempted through an experiment using the similar metal samples in different locations with some temperature variations between them. The setup in Figure 6-18 (left) shows two half-inch aluminum rods placed in sensing space. An object (obj-1) next to coil-1 was heated beforehand; meanwhile, the opposite obj-2 (near coil-5) is at room temperature.

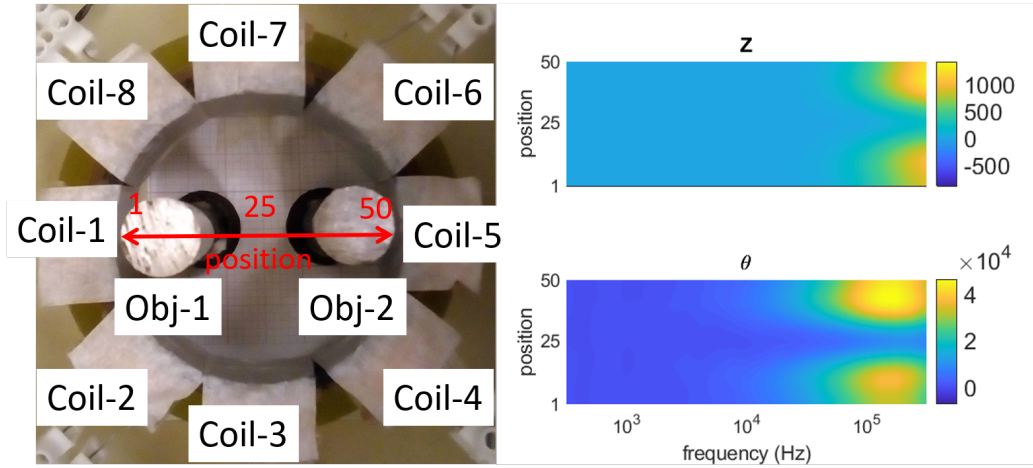


Figure 6-18: conductive objects distribution and the impedance-phase spectrum. Left: spatial location in the sensing space [1 50]. Right: surface plot of position (vertical axis) vs frequency (horizontal axis).

The reconstructed impedance and phase spectrum is shown in Figure 6-18 (right). Three decades of frequency are swept (in log) for respective measurements and put into (a shared) horizontal axis. The location in the sensing region (along the red-line [1–50]) is allocated to the vertical axis. It can be seen that the images become more pronounced at higher frequencies, having different colormap level which indicates the temperature difference.

Referring to the spectral information from two conductive objects in different circumstances (position and temperature), a subsequent test is conducted keeping track of the temperature of both objects. Once both object reach room temperature, the respective measurement data are treated as reference data (in addition to air background measurement). Phase spectrum for several conditions are given in Figure 6-19. It depicts the distribution of conductive object in different tem-

peratures relative to a condition at room temperature. There are 25 frequency points between 300 Hz – 300 kHz in logarithmic space.

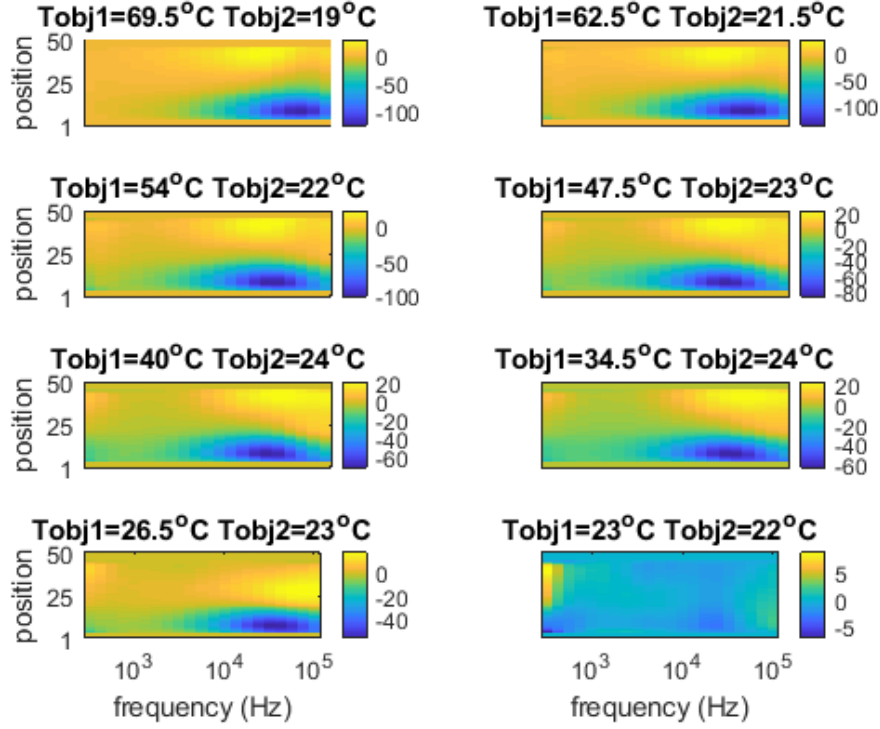


Figure 6-19: Spatial and spectral color map.

The arrangement of the experimental setup and its respective surface plot are similar to that in Figure 6-18. Plots on the right-column share the same vertical 'position' axis with those on the left-side; and all share the common horizontal 'frequency' axis of the bottom-row plots. Position = 1 represents location near coil-1 (where object-1 is placed having temperature of  $T_{obj1}$ ); whereas position = 50 is location near coil-5 (where object-2 is placed having temperature of  $T_{obj2}$ ). There are distinct illustrations (scaled individually) of temperature change related to conductivity change of the objects due to heating. A larger temperature difference between samples (reconstructed area) produces a wider color-scale range respectively.

Quantitative analysis taking the mean value of reconstructed heat map along the evaluated spectrum provides a reasonable trend in Figure 6-20. Temperature

difference ( $\Delta T = T_{obj1} - T_{obj2}$ ) of  $1\text{ }^{\circ}\text{C}$  gives the value of 0.152; meanwhile at the other end, value of 13.65 is obtained for  $41\text{ }^{\circ}\text{C}$  of difference in temperature. The graph is derived from pixel values of temperature difference image in respect with a reference condition. While electromagnetic tomography is mainly non-linear relation of measurement data and reconstructed image, the image-to-image operation can return a relatively linear fashion.

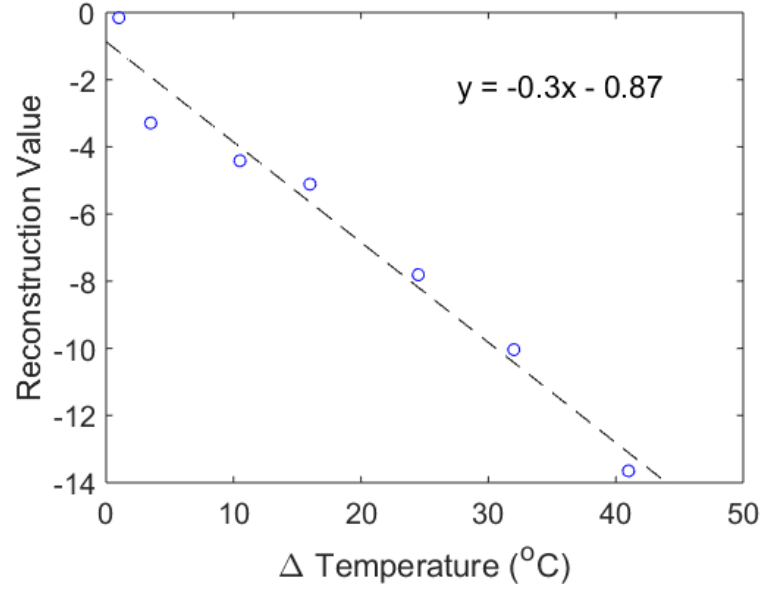


Figure 6-20: Reconstruction value vs temperature difference in heat map.

Another test case is the detection of pipe's temperature in which a heated fluid is contained (Figure 6-21). A copper pipe (42 mm outer diameter, 40 mm inner diameter) is placed in the sensing region. It is filled with water whose temperature is varied. Mutual impedance measurements are taken in cycles while monitoring the water temperature.

Phase data along the spectrum of 100 Hz – 100 kHz are reconstructed and evaluated according to water's temperature, using room temperature state as reference. Imaging value is correlated with thermocouple reading as shown in Figure 6-21 (right) and fitted in the following:

$$y = p_1x + p_2 \quad (6.2)$$

where the linear coefficients are:  $p_1 = -5.2561$ ,  $p_2 = -32.972$ ; whereas norm of

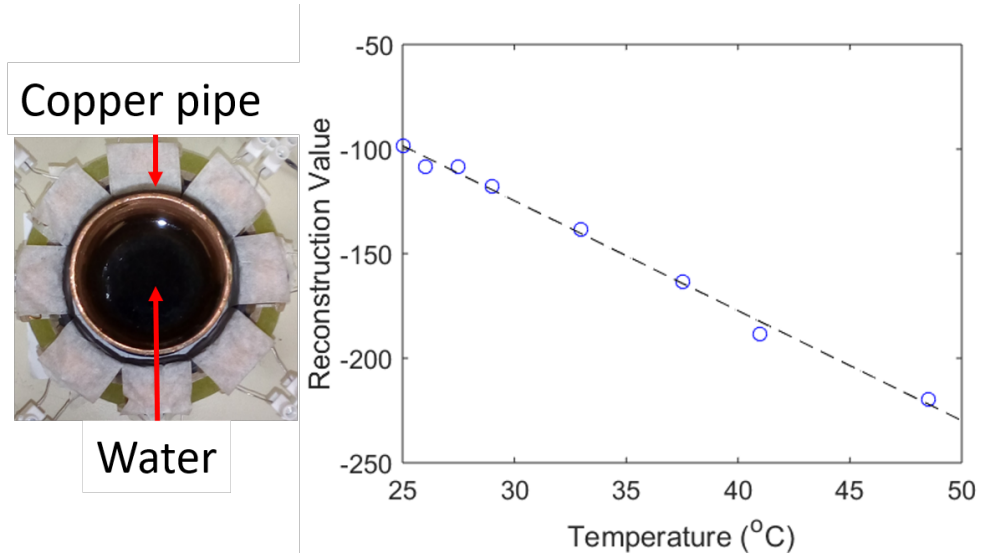


Figure 6-21: Experiment setup for temperature sensing in pipe.

residuals = 8.7962. For this particular situation, heating of the coil is considered due to a small gap between the pipe's surface and the coil array. Experiment cycles are timely conditioned to allow stable heat distribution. In terms of image reconstruction, the area near to coil has a higher sensitivity and should be carefully evaluated. Nevertheless, (6.2) provides an acceptable trend.

The quadratic polynomial temperature fit of Figure 6-17 is to be used for relatively wide temperature measurement range (in this case 0–80 °C) inside an object (assumed due to some physical effects in the aluminum sample); while the linear fit would be properly applied for temperature distribution (heat mapping) or a relatively narrow variation of surface temperature. Still, particular measurement situations are assessed.

## 6.5 Discussion

This work offers a non-invasive and non-intrusive measurement technique to investigate non-conductive inclusion inside a conductive body. It paves way for potential applications on conductivity level or metal classification and could be extended to gas bubble content determination in liquid metal flow. Using eddy current based spectroscopic imaging data and appropriate calibration, the investigation for a first time demonstrates a novel thermal mapping system. This is

a wireless and inductive based temperature mapping device that can have great potential applications where none of the existing thermal measuring devices could work noninvasively.

State-of-the-art of contactless technique for measuring and determining temperature distribution in industrial application is infrared thermal imaging [176]. Commercial thermal cameras are available with typical sensitivity about  $0.05\text{ }^{\circ}\text{C}$  (within the range  $-40\text{ }^{\circ}\text{C}$  to  $550\text{ }^{\circ}\text{C}$ ), a specified accuracy of  $\pm 5\text{ }^{\circ}\text{C}$ , and spatial resolution approximately  $1\text{ mm/pixel}$  ( $320\times 240$  elements at  $1\text{ m}$  object to camera distance) [177]. However, infrared thermography (IRT) requires optical access to the object's surface. On the other hand, the main advantage of the proposed method is that it can be used against an opaque structure. Although the sensitivity is limited to  $1\text{ }^{\circ}\text{C}$  (based on the test between  $0$  to  $80\text{ }^{\circ}\text{C}$  measured by thermocouple with resolution  $0.1\text{ }^{\circ}\text{C}$  and accuracy  $\pm 1\text{ }^{\circ}\text{C}$ ), the spatial resolution can reach about  $1.2\text{ mm/pixel}$  ( $50\times 50$  elements enclosing the object). Note that both techniques still need calibration, parameters setting, and (sometimes for IRT) inversion process which are comparatively not straightforward. Utilising a difference imaging, this noninvasive inductive temperature sensing is suitable for condition monitoring (temperature uniformity) in, for instances, pipe under-cladding, metal implant, or buried conductive materials.

The change of conductivity due to the change of temperature in materials is an established principle. Here the author offers some technical solutions using procedures which have been shown in the experiments. The use of magnetic induction spectroscopy and its imaging results for accomplishing such task provides rich information. However, some disadvantages should be anticipated. Tests have been conducted for relatively low-ranged temperature estimation, and the resolution would be affected by imaging quality from which the temperature values are extracted. Soft-field tomography imaging such as electromagnetic tomography is an ill-posed problem, hence the reconstruction is challenging. Besides spatial constraint, the temporal ability of the conductivity reconstruction should be considered for catching the continuous transient change in temperature variability for typical industrial settings. In addition, more uncertainties occur compared with 1-dimensional measurement methods. The proposed technique has advantages of a remote measurement, enhanced with temperature mapping without the need



to either physical or optical access required by conventional means. Albeit limited, this method would still find suitable applications once the aforementioned aspects are accounted.

## 6.6 Conclusion

Mutual impedance and phase spectra have been observed for metal objects with different conductivity levels using MIT. Depicted in a spectroscopic fashion, the perplexity of electromagnetic tomography reconstruction is reposed when the imaging spectrum pronounces substantial information about the physical properties of an object. A distinct shift in the amplitude, accompanied by gradient location in the phase are valuable insight upon which more sophisticated work can be built. Some foreseeable implementations are phase distribution of a conductive substance in a concealed vessel, e.g. steel flow in continuous casting, as well as temperature-dependent conductivity mapping inside a physically and/or optically inaccessible region. The magnetic induction sensing system is inherently immune to surrounding contamination, robust in construction, and cost-effective for industrial deployment. For the first time, the author demonstrated it is possible to derive the temperature and temperature distribution of a known metal using spectroscopic eddy current data. This will open up a new type of thermal mapping sensing device for many industrial and other applications that require fully noninvasive thermal mapping.

# Chapter 7

## Interior Void Classification in Liquid Metal

Previously, a cross-section of flow shapes has been visualised using the MIT technique. This chapter exposes an interior void classifier based on multi-frequency mutual induction measurements. The datasets are induced voltage collections of several non-metallic inclusions (NMI) patterns in liquid metal static tests and are used to train a machine learning model. The model architectures are a fully connected neural network (FCNN) for 1D; and a convolutional neural network (CNN) for 2D data. Refined with representative flow scenarios, the trained model could be deployed for an intelligent online control system of the liquid metal process.

### 7.1 Introduction

The level of void and/or non-metallic inclusions needs to be estimated in many liquid metal applications. In continuous steel casting, the presence of NMI, occurring at the primary stage and then more crucial at the casting process (multiphase flow of molten metal and argon gas from tundish to mould), affects the steel cleanliness. Another application that necessitates the observation of porosity of metal in its liquid phase is foam manufacturing [178]. The porosity of the liquid metal will determine the final solid porous metal. Liquid metal is also used for cooling a nuclear reactor [179] [180]. In the liquid metal-cooled reactor, it is desired to

detect and characterise the voids due to their influence on heat exchange.

The MIT system produces mutual induction values as boundary measurements which are then transformed into a cross-sectional image of conductivity distribution. This capability is further enriched by employing frequency-sweep on each measurement resulting in spatio-spectral information. The structure of a conductive body can be explored using the aforementioned spectroscopy [45]. However, spatial resolution is limited especially for recovering small and dispersed interior non-conductive disturbances. Exhaustive algorithm or post-processing is the usual treatments, still, they could not satisfy demands from some industrial applications.

In Chapter 4, the author investigated common two-phase liquid-gas flow scenarios such as full-stream, stratified, bubbly, and annular. These basic flow shapes have been reconstructed with conventional MIT [44]. Accordingly, adaptation of AI become more common in the metallurgy sector [181] [126]. ML approaches for analysing the continuous casting process was surveyed in [182]. Thus, data-driven method and system are prospective for field implementation to extract useful information in helping production. This follow-up work attempts to produce a classification of liquid metal inner structure based on multi-frequency mutual induction measurements data.

## 7.2 Machine Learning Method

Among several techniques in employing ML for classification problems reviewed in [183], the following work trains the network from scratch while adjusting an efficient architecture for the given problem and dataset. In the previous chapter, NN and CNN functions were explained. Here, two methods are investigated: traditional dense FCNN for classifier using one-dimensional (1D) data, and CNN for classifier using two-dimensional (2D) data. Both are implemented in Keras 2.4.0 framework [124] with TensorFlow 2.3.0 backend [125].

Mutual induction measurements are conducted using a two-port method with LCR meter and additional switching module (Keysight Technologies) for sequentially selecting a pair out of an 8-coil array at a time. This measurement system has an SNR between 60–90 dB, where measurement at low-frequency opposite-

coil has the lowest SNR; and high-frequency adjacent-coil has the highest SNR. The detailed configuration was described in [46]. For the following work (see Figure 7-1), all 28 (pair-combination) mutual induction coils are measured and swept from 100 Hz to 100 kHz (logarithmic scale with 28 points).

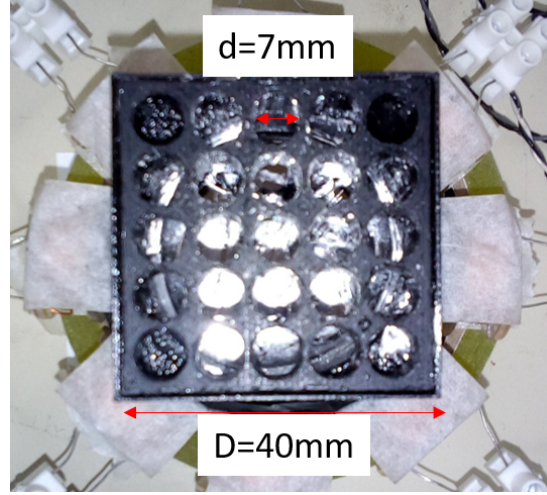


Figure 7-1: The liquid metal column with grid for wood inclusion

Pixelated data vector was commonly used as either main or additional input for improving traditional image classification performances [184]. This form of pseudo-image can be built from an array of sensors' reading on the first axis and another measurement dimension on the second axis. An example of a classifier model which is built on limited training images was reported by [185]. Nevertheless, this dataset will be a valuable framework in developing tomographic sensing interpretation using ML [186] [187].

### 7.3 FCNN Classifier

In the FCNN classifier, the data are built from mutual induction measurement between every coil pair. There are eight coils so that  $C_2^8$  gives 28 data of mutual combination. This is observed at multiple frequency points.

$$\mathbf{M}_{f,n} = \begin{bmatrix} m_{1,1} & \dots & m_{1,28} \\ \vdots & \ddots & \vdots \\ m_{28,1} & \dots & m_{28,28} \end{bmatrix} \quad (7.1)$$

The measurement data structure in (7.1) details frequency points  $f$  with  $n$  mutual induction values. For instance,  $m_{1,1}$  is mutual induction between coil-1 and coil-2 at the first frequency point,  $m_{1,28}$  is mutual induction between coil-7 and coil-8 at the first frequency point,  $m_{28,1}$  is mutual induction between coil-1 and coil-2 at the last frequency point, and  $m_{28,28}$  is mutual induction between coil-7 and coil-8 at the last frequency point. Particularly, the phase-shift between the driving signal from transmitting-coil and the detected signal at receiving-coil is taken to represent the sensing information. The measurement is relative values against the reference where liquid metal is full (without any inclusion).  $\theta$  are phase-shift values for an investigated case, whereas  $\theta_0$  are phase-shift values for a reference condition. By this definition, the studied data are 28 of  $\Delta\theta = \theta - \theta_0$  values at 28 frequency points.

$$val(f) = \sqrt{\sum_{i=1}^{28} \Delta\theta_i(f)^2} \quad (7.2)$$

Equation (7.2) is applied on each frequency point for all 28 phase-difference values, thus  $val(f)$  is the value at frequency  $f$ . As a result, a normalised one-dimensional data plot is obtained as shown in Figure 7-2. Here,  $index=1$  corresponds to a data point at  $f=100$  Hz,  $index=10$  corresponds to a data point at  $f=1$  kHz, and so on. Previous work [45] used the same normalisation so that the measurement data can be treated as an indicator for structural characteristic of metallic materials.

A wood (balsa) occupies a single grid in the liquid metal (GaInSn) column. Five classes are studied: 1 wood (central grid), 2 woods (East-West), 3 woods (East-centre-West), 4 woods (North-South East-West), and 5 woods (North-South centre East-West), as shown in Figure 7-3. Each case is measured in separate sessions and accompanied by the respective reference measurement. Datasets are created and labelled for five classes, and split into training (80%) and test (20%) data. The validation set is randomly chosen from training data during the training process.

Figure 7-4 shows the FCNN architecture. Keras model Sequential is constructed consisting of a hidden dense layers which has 32 neurons, with activation function

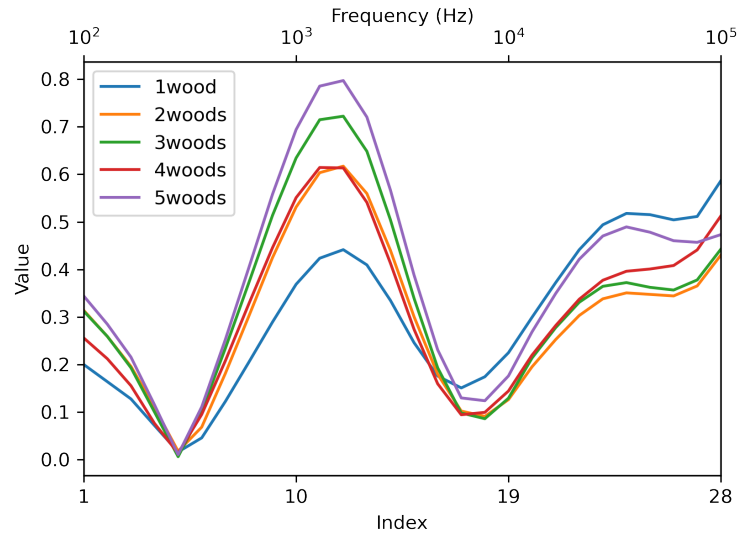


Figure 7-2: The plot of 1D data for a number of wood inclusions

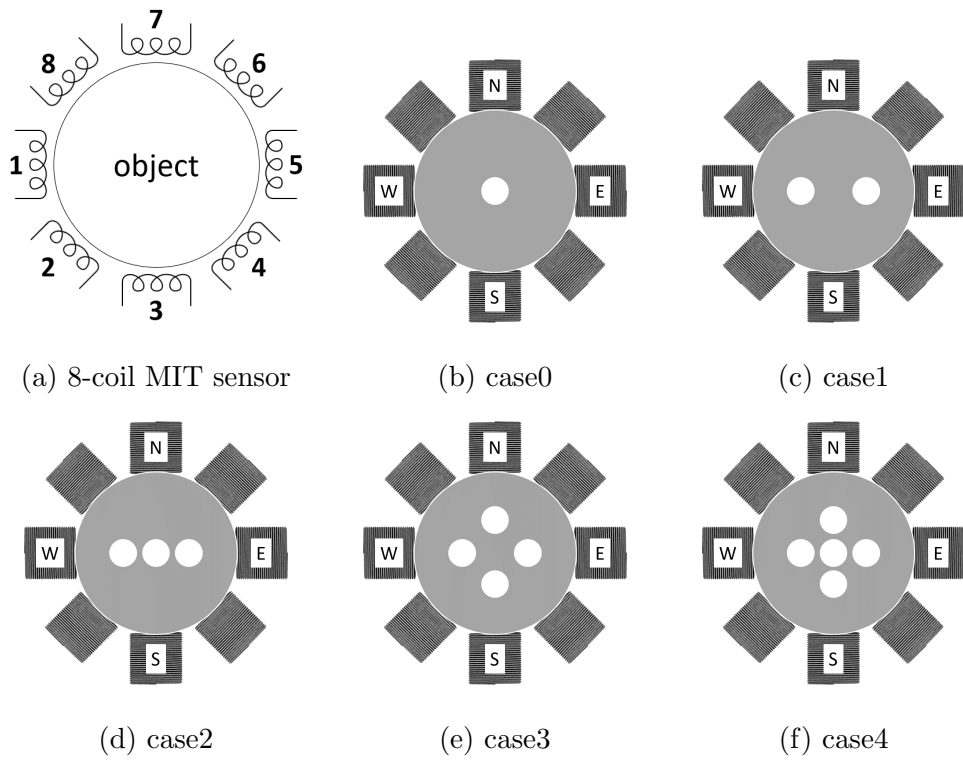


Figure 7-3: Wood inclusions in liquid metal cases with relative positions to sensors' arrangement

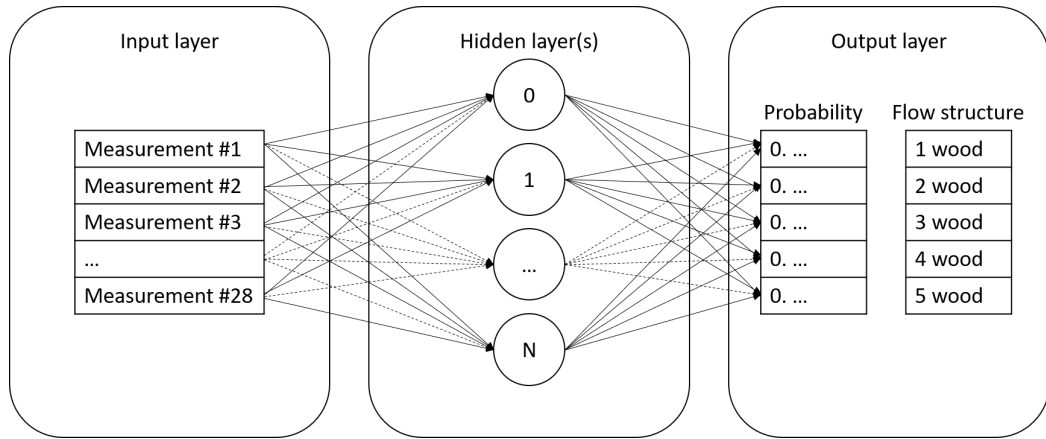


Figure 7-4: The FCNN architecture: a neural network with features, hidden layers, and predictions

ReLU. Dropout regularisation layers with a rate of 0.2 are added in an attempt to prevent overfitting. Vector of “logits” scores for each class are then converted into probability using a Softmax function. Loss function Sparse Categorical Crossentropy takes a vector of logits and a “True” index and returns a scalar loss for each example. The model is compiled using optimiser ADaptive with Momentum (Adam), utilising “accuracy” metrics to measure the loss and the accuracy of the model. This model will then be fitted adjusting parameters to minimise the loss. The total number of parameters (param) is 2149, all of which are trainable. Model summary is described in Table 7.1.

Table 7.1: FCNN Model Summary

Layer	Properties	Output Shape	Param
input	28 x 1	(28)	0
Dense1	Activation: ReLU	(32)	928
Dropout1	Rate: 0.2	(32)	0
Dense2	Activation: ReLU	(32)	1056
Dropout2	Rate: 0.2	(32)	0
Dense3	+ Softmax	(5)	165

Figure 7-5 shows training and validation accuracy-loss along 250 epochs. At the beginning (1s 28ms/step) train loss is 1.6931, train accuracy is 0.2200, validation loss is 1.6403, and validation accuracy is 0.2000; at the end (0s 5ms/step) train loss is 0.4075, train accuracy is 0.8800, validation loss is 0.3122, and validation

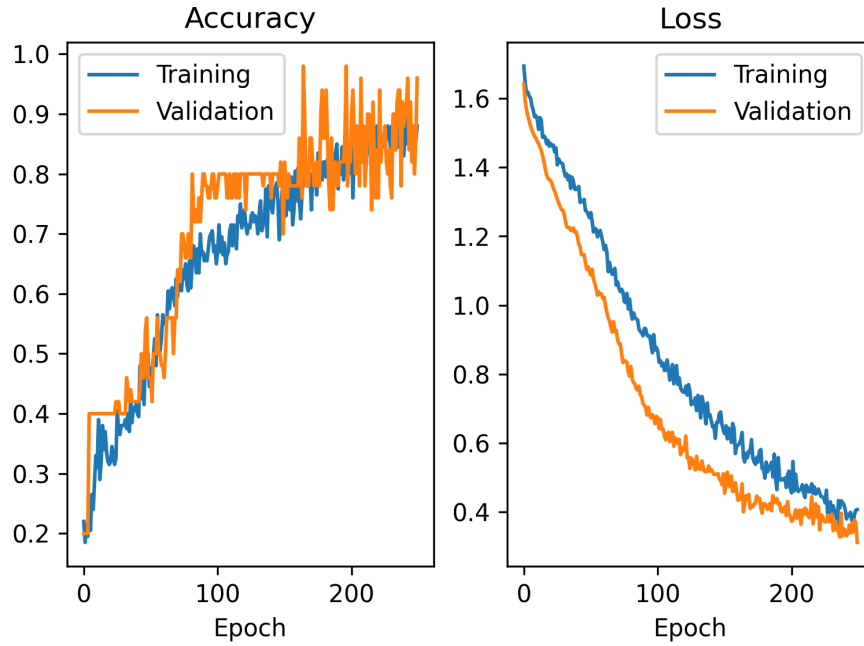


Figure 7-5: FCNN training and validation accuracy-loss vs epoch

accuracy is 0.9599. Training and test utilize CPU with four compute cores clocked at 2.3 GHz and 4 GB of RAM. The training time for all data within complete number of epochs lasts 21.9545 s, whereas the test takes 0.2811 s. Performance is checked on test set, giving: test loss 0.31 and test accuracy 0.95.

Examples of prediction on woods/voids are depicted in Figure 7-6. Ten test data are fed into the model, and the prediction bar chart is shown accordingly. The chart shows how confident the model decides that the data corresponds to each class. The confusion matrix is shown in Figure 7-7. The map represents tests, where each case has ten predictions. The classifier has a good accuracy, although four-woods case produce prediction errors. Experimentally, 4woods and 5woods are only differentiated by a central inclusion which is inherently difficult to measure.



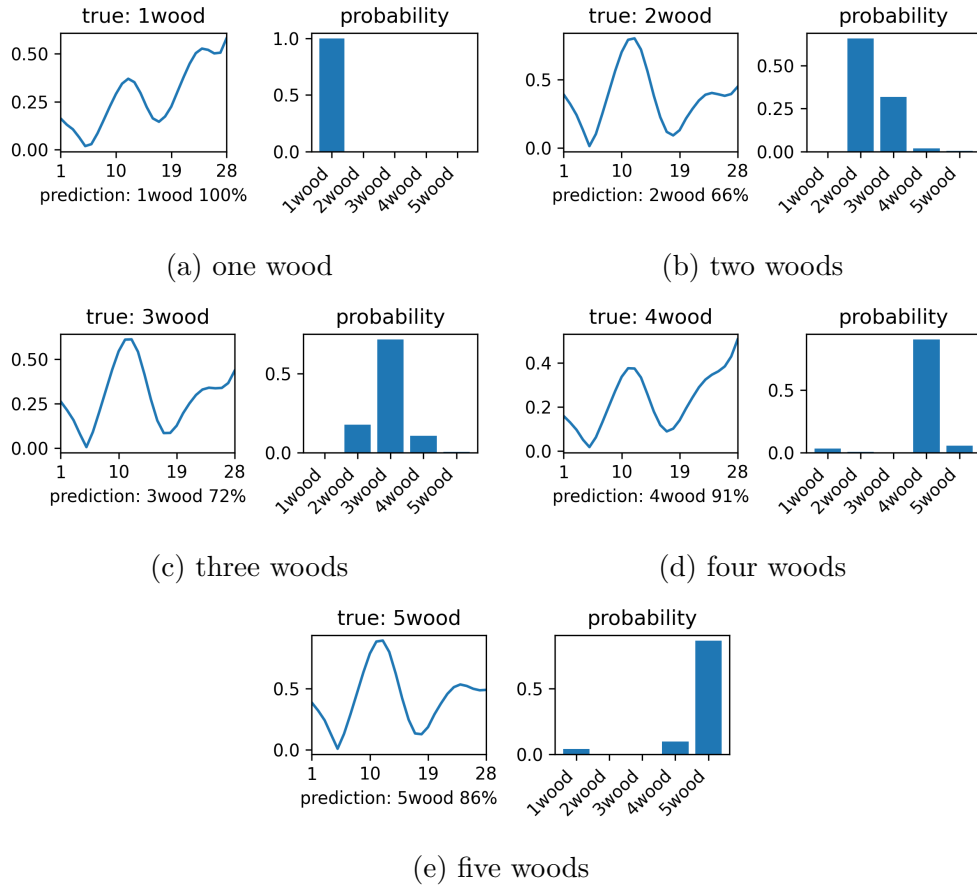


Figure 7-6: The prediction result from the FCNN model. Left: the plot of a sample data case. Right: the probability chart

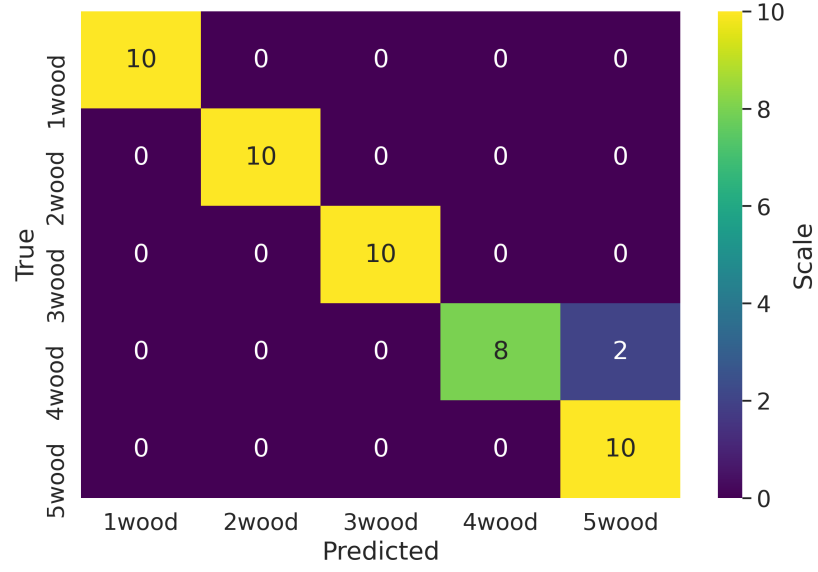


Figure 7-7: The confusion matrix of prediction tests by the FCNN model

## 7.4 CNN Classifier

Two-dimensional data in the form of multi-frequency mutual coil combination are constructed as pseudo-image. The data arrangement follows the structure in (7.1). This makes a 2D analysis approach is suitable, such as applying a CNN model.

Mutual coil pairs measurements lie on the horizontal axis; whereas frequency points on the vertical axis. Mutual inductance combinations are 28 (from eight coils), so to shape the image into 2D form, the same number of frequency points is set to 28. The measurement frequency is swept in logarithmic fashion from 100 Hz up to 100 kHz. An example of a pseudo-image is shown in Figure 7-8.

The pseudo-image is 28x28 pixels and the values are scaled between [0 1]. Each value represents  $\Delta\theta$  which is a phase-difference measurement of a liquid metal case ( $\theta$ ), against a free-space (air) background reference ( $\theta_0$ ). In addition to cases depicted in Figure 7-3, up to nine inclusions are given, and a full liquid metal (no inclusion) condition is incorporated. Therefore, there are ten classes to investigate. Datasets are split into training (80%) and test (20%) data. Validation set is randomly chosen from training data during the training process.

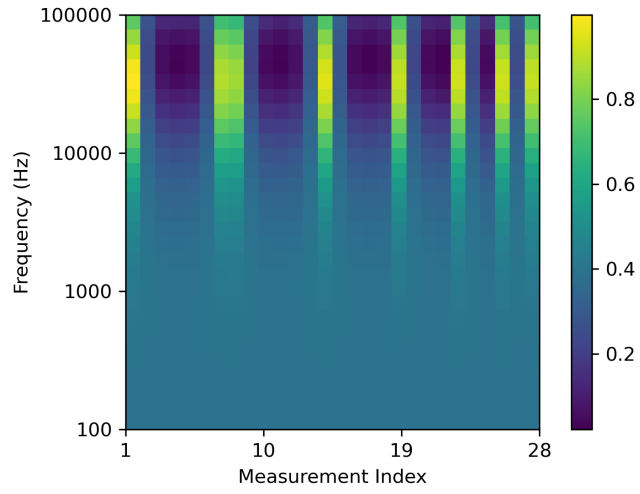


Figure 7-8: The layout of pseudo-image which represents multi-frequency mutual induction measurement data

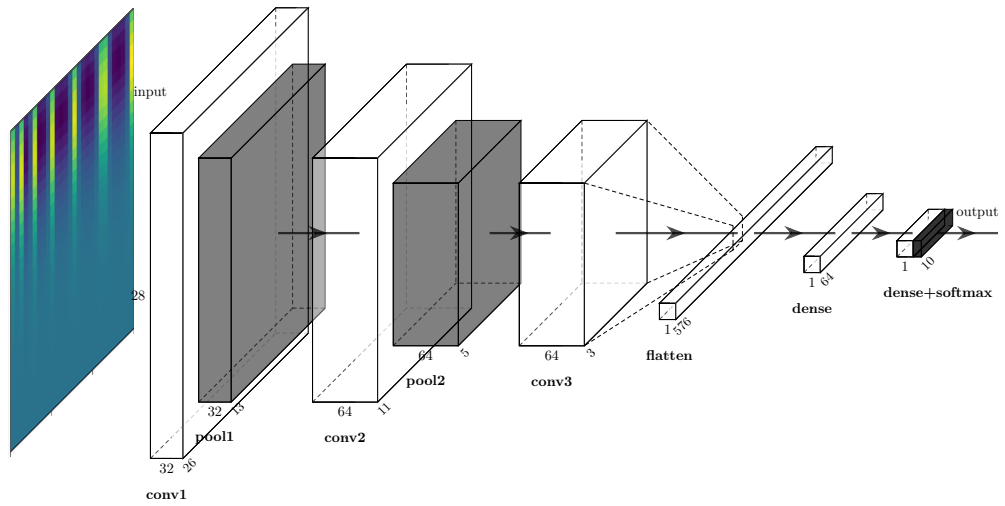


Figure 7-9: The CNN model

Sequential layers consist of Conv2D, MaxPooling2D, and Dense are stacked for the model, as illustrated in Figure 7-9. The diagram gives the information about the input shape, which is a pseudo-image in 2D 28x28 pixels and one 'colour' channel. Subsequent layers are convolution and pooling before the tensor is flattened for the traditional dense neural network. Finally, the last layer provides a number of outputs according to the prediction classes. Table 7.2 describes the architecture in detail, where total (trainable) parameters are 93322.

Table 7.2: CNN Model Summary

Layer	Properties	Stride	Padding	Output Shape	Param
input	28 x 28 x 1	-	-	(28, 28, 1)	0
Convolution1	Filters: 32 Kernel: 3 x 3 Activation: ReLU	1 x 1	Valid	(26, 26, 32)	320
MaxPooling1	Kernel: 2 x 2	-	Valid	(13, 13, 32)	0
Convolution2	Filters: 64 Kernel: 3 x 3 Activation: ReLU	1 x 1	Valid	(11, 11, 64)	18496
MaxPooling2	Kernel: 2 x 2	-	Valid	(5, 5, 64)	0
Convolution3	Filters: 64 Kernel: 3 x 3 Activation: ReLU	1 x 1	Valid	(3, 3, 64)	36928
Flatten	-	-	-	(576)	0
Dense1	Activation: ReLU	-	-	(64)	36928
Dense2	+ Softmax	-	-	(10)	650

Figure 7-10 shows training and validation accuracy-loss along 250 epochs. Training and test utilize CPU with four compute cores clocked at 2.3 GHz and 4 GB of RAM. The training time for all data within complete number of epochs lasts 297.1258 s, whereas the test takes 0.4219 s. Performance is checked on test set, giving: test loss 0.18 and test accuracy 0.96.

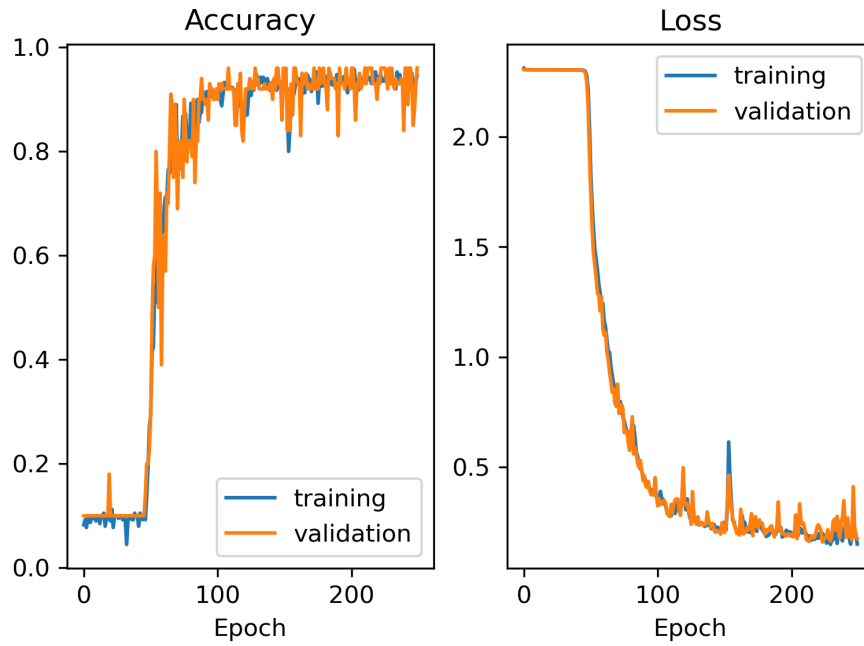


Figure 7-10: CNN training and validation accuract-loss vs epoch

Examples of prediction cases are depicted in Figure 7-11 where confidence percentage is shown at the bottom of each illustration.

The confusion matrix is mapped in Figure 7-12. For clarity, the labels associated with inclusion numbers are presented on the axes. Almost all test samples are predicted accurately, except for full case (no inclusion) where the classifier mispredicts symmetrically distributed of one and five voids/woods (NMI).

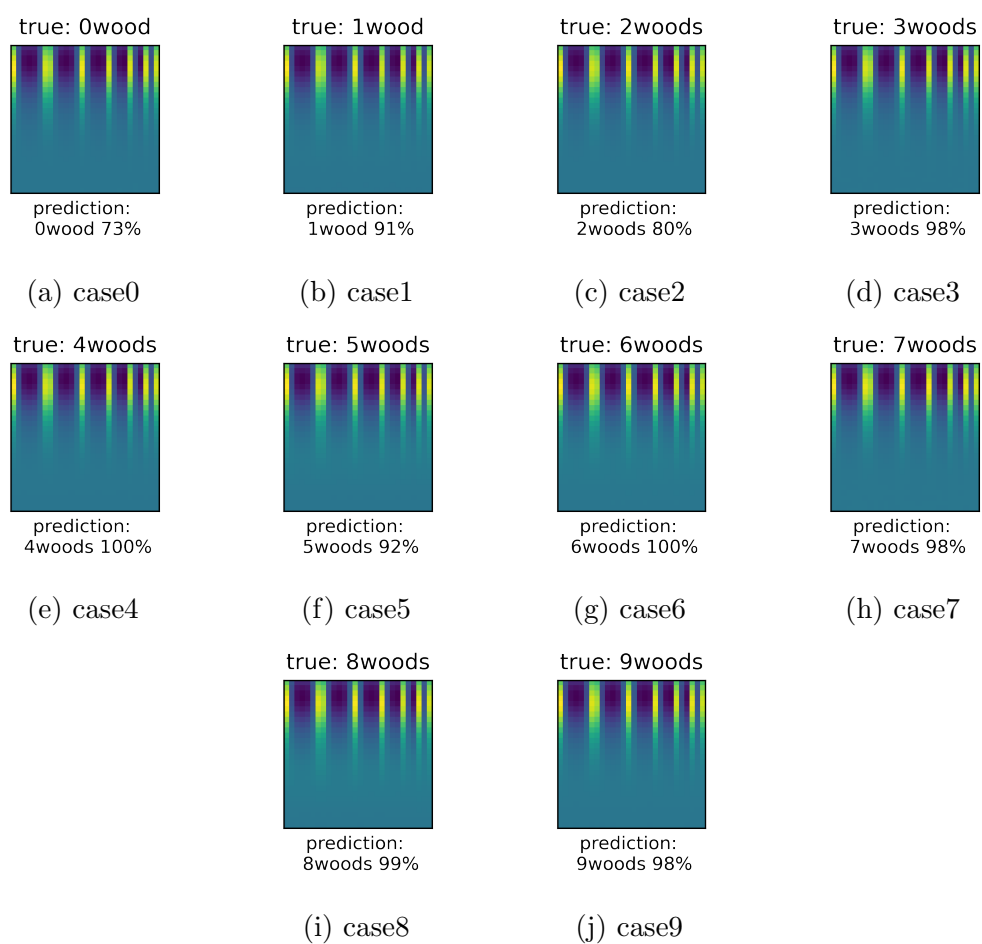


Figure 7-11: The prediction result from the CNN model: the pseudo-image of a sample test data with its respective label and probability

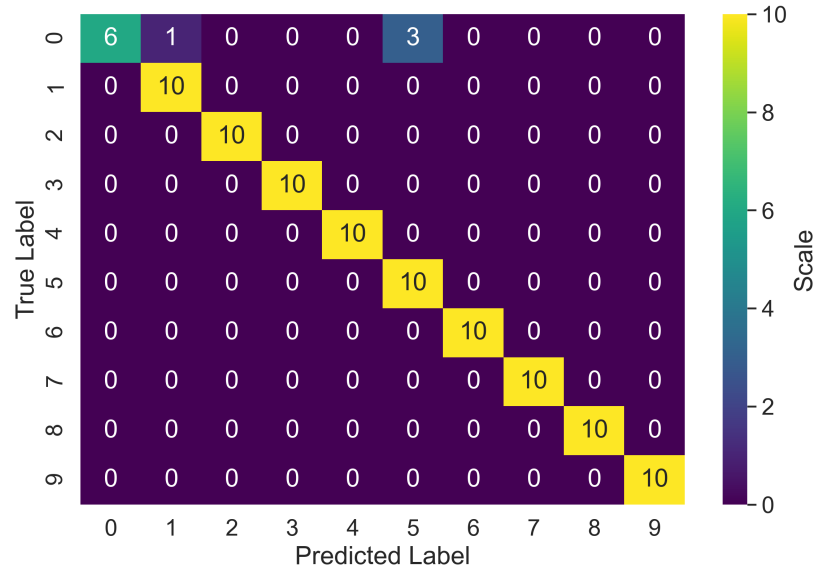


Figure 7-12: The confusion matrix of prediction tests by the CNN model

## 7.5 Discussion

In this study, the author defines the classification based on the number of voids. Datasets are taken from experimental data where measurements are conducted in different sessions. In each session, all cases including references are tested. It ensures that the datasets are statistically independent. Data from all measurement sessions are then compiled to constitute complete datasets. A dedicated function in TensorFlow randomly divides the data sets into proportion of training and validation data.

It is possible to define the classification in different ways depending on the application. The accuracy of the classifier, on the one hand, depends on the algorithm and training strategies and the other hand depends on the accuracy of the MIT data. With an interest in the interior region of the liquid metal, the accuracy of the MIT setup for low-frequency data will be an important factor.

The author intends to provide a prospect of the study for liquid metal processing where void or NMI determination is crucial. The developed ML approach provides a potent sensing method to address some issues on detecting and characterising the two-phase liquid metal-gas system. Although this case study is for steel-casting where the investigation of bubble distribution in metal flow is desired,

this approach would also apply in a wide area of implementation involving liquid metal such as reactor coolant and functional material processing.

The simplified experimental data is aimed as a starter to demonstrate the ML approach for liquid metal interior investigation. Additionally, computational fluid dynamics (CFD) simulation would also be used to provide training and validation input. This proposed method, once escalated to field test could offer an alternative to capture local and quantitative information relevant to operating condition.

## 7.6 Conclusion

The work proposes a liquid metal flow condition classifier focused on the interior voidage. Measurement datasets are multi-frequency mutual induction sensing of several wood inclusion variations inside liquid metal GaInSn. The 1D classifier architecture is a multi-layered fully connected neural network (FCNN). After 250 epochs, this model produces a training loss of 0.40, training accuracy 0.88; whereas test accuracy is 95%. The 2D classifier architecture is based on a convolutional neural network (CNN). After 250 epochs, this model produces a training loss of 0.15, training accuracy 0.95; whereas test accuracy is 96%. The number of woods, or non-metallic inclusions (NMI), classification can be further translated into other quantification such as interior void fraction. This framework provides a prospect for a data-driven liquid metal processing system.



# Chapter 8

## Conclusion

### 8.1 Summary

The research aims to deal with liquid metal through electromagnetic tomography using multi-frequency and complex methods. The work has been done in magnetic induction tomography with spectroscopy technique. Both computational and experimental works are explained.

In this work, three different types of MIT systems have been assembled. Magnitude-based hardware is meant for portable and fast measurement. As for the second system, the LCR bridge instrument provides stable wide-frequency measurement. The third system, which consists of an embedded module with custom analogue circuits, is tailored for complex impedance measurement in multi-frequency.

The author also designed and constructed MIT sensors capable of visualising liquid metal. Good correlations between actual shapes and reconstructed shapes have been obtained. In addition, a neural network has been trained to accurately classify flow shapes.

On the software side, spatio-spectral image reconstruction algorithm has been formulated to do a spectrally correlated analysis identifying an object's circumstances. Samples with conductivity, size, location and internal structure variations have been investigated. The resulting complex plots from reconstruction comprehensively indicate functional and structural behaviours in the metallic

materials.

Using eddy current based spectroscopic imaging data and appropriate calibration, this research demonstrates a novel thermal mapping system. The author demonstrated the feasibility of deriving the temperature distribution of a known metal using spectroscopic eddy current data. Both reconstructed images and regression plots provide a relationship between MIT and the object's temperature.

This study also proposes a liquid metal flow condition classifier focused on the interior voidage. It is capable of accurately determining the number of inclusions in liquid metal with a quick decision. The developed machine learning approach provides a potent sensing method to address some issues in detecting and characterising the two-phase liquid metal-gas system. It is intended to provide a prospect for liquid metal processing where void or non-metallic inclusions determination is crucial.

Multi-frequency setup contributes to the previously established MIT step forward. In addition to conductivity profiling using spectroscopic reconstruction, coil arrays are also able to sense and map the temperature of objects. To the best of the author's knowledge, this inductive thermography connects a theoretical basis and is the first of its kind. Complex measurement produces complex plots derived from reconstructed images to characterise the structure and function of metallic materials. Moreover, the richness of data can be utilised for machine learning approaches such as the classification of flow conditions. Tying together, this research dedicates part of the studied techniques for liquid metal process control demonstration.

## 8.2 Limitations and Further Work

Restating discussions from previous chapters, some limitations and suggestions are identified:

- The measurement setup is based on general-purpose electronics which span some frequency range. However, its performance is not uniform in all frequencies. This is indicated by relatively weaker SNR at low frequency. Although the work anticipates this problem by calibration and referencing,

specialised instrumentation might perform better. This factor is important, for instance, in producing a complex plot.

- In temperature detection, the sample's innate characteristic needs to be considered further. Based on preliminary experiments that have been done, rigorous modelling taking into account the physical coefficients is a direction to pursue. Furthermore, wider temperature variation represents the industrial case more realistically.
- Dynamic tests and online reconstruction will pose some impacts on sensing behaviour. The integrated setting along with another sensing and system affects the measurement differently from stand-alone lab testing. Both software and hardware should be tailored to fit the purpose.
- A data-driven method relies on raw data quality as well as quantity. Datasets should be a proper representation of the problem under investigation. On the other hand, the vast aspect of artificial intelligence demands more focus on fine-tuning the learning process and deployment practice.

The above highlights some issues worthy of future research. As this thesis has limitations, so the recommendation is also by no means exhaustive. To summarise, the MIT technique still has a lot to explore, and this work more or less serves as a good starting point to raise the new area of research and implementation.

# Appendix

Supplementary materials used throughout the thesis can be further accessed in the following:

- Figure 3-2 is based on [github.com/dreading/tex-neural-network](https://github.com/dreading/tex-neural-network)
- Figure 3-3 is based on [github.com/davidstutz/latex-resources](https://github.com/davidstutz/latex-resources)
- Figure 3-12 is based on [www.overleaf.com/latex/examples/demodulador-qam/qswnhnbyqycf](https://www.overleaf.com/latex/examples/demodulador-qam/qswnhnbyqycf)
- Hardware design and software resources from Subsection 3.3.3 are available upon request on <https://github.com/imuttakin/>.
- Figure 4-5 is based on [www.overleaf.com/latex/examples/neural-network-color/jwsbrhgwmgmt](https://www.overleaf.com/latex/examples/neural-network-color/jwsbrhgwmgmt)
- Dataset and script from Chapter 4 and Chapter 7 are available upon request on <https://github.bath.ac.uk/im463/>.
- Figure 7-9 is visualised using modified version of PlotNeuralNet [188].

# References

- [1] World Steel in Figures. Technical report, The World Steel Association (worldsteel), April 2021.
- [2] T. Wondrak, U. Hampel, M. Ratajczak, I. Glavinic, F. Stefani, S. Eckert, D. van der Plas, P. Pennerstorfer, I. Muttakin, M. Soleimani, S. Abouelazayem, J. Hlava, A. Blishchik, and S. Kenjeres. Real-time control of the mould flow in a model of continuous casting in frame of the TOMOCON project. *IOP Conference Series: Materials Science and Engineering*, 424:012003, oct 2018. doi: 10.1088/1757-899x/424/1/012003.
- [3] Lifeng Zhang, Yufeng Wang, and Xiangjun Zuo. Flow Transport and Inclusion Motion in Steel Continuous-Casting Mold under Submerged Entry Nozzle Clogging Condition. *Metallurgical and Materials Transactions B*, 39(4):534–550, August 2008. ISSN 1073-5615, 1543-1916. doi: 10.1007/s11663-008-9154-6.
- [4] M Ratajczak, D Hernández, T Richter, D Otte, D Buchenau, N Krauter, and T Wondrak. Measurement techniques for liquid metals. *IOP Conference Series: Materials Science and Engineering*, 228:012023, jul 2017. doi: 10.1088/1757-899x/228/1/012023.
- [5] Avinash Kumar Acharya, Anil Kumar Sharma, Ch.S.S.S. Avinash, Sanjay Kumar Das, Lydia Gnanadhas, B.K. Nashine, and P. Selvaraj. Investigation of molten fuel coolant interaction phenomena using real time x-ray imaging of simulated woods metal-water system. *Nuclear Engineering and Technology*, 49(7):1442–1450, 2017. ISSN 1738-5733. doi: <https://doi.org/10.1016/j.net.2017.07.003>.

- [6] Y. Saito, K. Mishima, Y. Tobita, T. Suzuki, M. Matsubayashi, I.C. Lim, and J.E. Cha. Application of high frame-rate neutron radiography to liquid-metal two-phase flow research. *Nuclear Instruments and Methods in Physics Research Section A: Accelerators, Spectrometers, Detectors and Associated Equipment*, 542(1):168–174, 2005. ISSN 0168-9002. doi: <https://doi.org/10.1016/j.nima.2005.01.095>. Proceedings of the Fifth International Topical Meeting on Neutron Radiography.
- [7] Y. Saito, K. Mishima, Y. Tobita, T. Suzuki, and M. Matsubayashi. Measurements of liquid-metal two-phase flow by using neutron radiography and electrical conductivity probe. *Experimental Thermal and Fluid Science*, 29(3):323–330, 2005. ISSN 0894-1777. doi: <https://doi.org/10.1016/j.expthermflusci.2004.05.009>. Third European-Japanese Two-Phase Flow Group Meeting.
- [8] Nobuyuki Takenaka, Hitoshi Asano, Terushige Fujii, Yasunori Motomura, Atsuo Ono, Masahito Matsubayashi, and Akira Tsuruno. Liquid metal flow measurement by neutron radiography. *Nuclear Instruments and Methods in Physics Research Section A: Accelerators, Spectrometers, Detectors and Associated Equipment*, 377(1):156–160, 1996. ISSN 0168-9002. doi: [https://doi.org/10.1016/0168-9002\(96\)00134-9](https://doi.org/10.1016/0168-9002(96)00134-9). Proceedings of the Second International Topical Meeting on Neutron.
- [9] M. Schneider and J. W. Evans. A novel probe for detecting gas bubbles in liquid metals. *Metallurgical and Materials Transactions B*, 37(3):333–337, June 2006. ISSN 1543-1916. doi: [10.1007/s11663-006-0018-7](https://doi.org/10.1007/s11663-006-0018-7).
- [10] Christophe Corazza, Kris Rosseel, Willem Leysen, Kristof Gladinez, Alessandro Marino, Jun Lim, and Alexander Aerts. Optical fibre void fraction detection for liquid metal fast neutron reactors. *Experimental Thermal and Fluid Science*, 113:109865, 2020. ISSN 0894-1777. doi: <https://doi.org/10.1016/j.expthermflusci.2019.109865>.
- [11] Ayaka Katayose, Ryosuke Yokose, Kento Obata, and Toshinori Makuta. New fabrication method and properties of porous metals produced by ultrasonic control of microbubble size. *Microsystem Technologies*, 24(1):709–

- 713, January 2018. ISSN 0946-7076, 1432-1858. doi: 10.1007/s00542-017-3390-0.
- [12] V. Gergely and T.W. Clyne. Drainage in standing liquid metal foams: modelling and experimental observations. *Acta Materialia*, 52(10):3047–3058, 2004. ISSN 1359-6454. doi: <https://doi.org/10.1016/j.actamat.2004.03.007>.
  - [13] Francisco García-Moreno, Paul Hans Kamm, Tillmann Robert Neu, Felix Bülk, Rajmund Mokso, Christian Matthias Schlepütz, Marco Stampanoni, and John Banhart. Using X-ray tomoscopy to explore the dynamics of foaming metal. *Nature Communications*, 10(1):3762, August 2019. ISSN 2041-1723. doi: 10.1038/s41467-019-11521-1.
  - [14] S. Fox and J. Campbell. Liquid metal quality. *International Journal of Cast Metals Research*, 14(6):335–340, 2002. doi: 10.1080/13640461.2002.11819451.
  - [15] Roderick I. L. Guthrie and Mei Li. In Situ detection of inclusions in liquid metals: Part I. Mathematical modeling of the behavior of particles traversing the electric sensing zone. *Metallurgical and Materials Transactions B*, 32(6):1067, December 2001. ISSN 1543-1916. doi: 10.1007/s11663-001-0095-6.
  - [16] R Binns, A R A Lyons, A J Peyton, and W D N Pritchard. Imaging molten steel flow profiles. *Measurement Science and Technology*, 12(8):1132–1138, aug 2001. ISSN 0957-0233. doi: 10.1088/0957-0233/12/8/320.
  - [17] S. R. Higson, P. Drake, A. Lyons, A. Peyton, and B. Lionheart. Electromagnetic visualisation of steel flow in continuous casting nozzles. *Ironmaking & Steelmaking*, 33(5):357–361, October 2006. ISSN 0301-9233, 1743-2812. doi: 10.1179/174328106X149897.
  - [18] J. van Oord, T.W.J. Peeters, A.E. Westendorp, S.H. Higson, and J.P.T.M Brockhoff. Transition of the flow pattern in the feeding system. In *2nd International Conference of Simulation and Modelling of Metallurgical Processes in Steelmaking*, Graz, Austria, September 2007.
  - [19] X. Ma, A. J. Peyton, R. Binns, and S. R. Higson. Electromagnetic tech-

- niques for imaging the cross-section distribution of molten steel flow in the continuous casting nozzle. *IEEE Sensors Journal*, 5(2):224–232, April 2005. ISSN 1558-1748. doi: 10.1109/JSEN.2004.842443.
- [20] X Ma, A J Peyton, S R Higson, and P Drake. Development of multiple frequency electromagnetic induction systems for steel flow visualization. *Measurement Science and Technology*, 19(9):094008, September 2008. ISSN 0957-0233, 1361-6501. doi: 10.1088/0957-0233/19/9/094008.
- [21] D.C. Barber, B.H. Brown, and I.L. Freeston. Imaging spatial distributions of resistivity using applied potential tomography. *Electronics Letters*, 19(22):933, 1983. ISSN 00135194. doi: 10.1049/el:19830637.
- [22] S.M. Huang, A.B. Plaskowski, C.G. Xie, and M.S. Beck. Capacitance-based tomographic flow imaging system. *Electronics Letters*, 24(7):418, 1988. ISSN 00135194. doi: 10.1049/el:19880283.
- [23] S Al-Zeibak and N H Saunders. A feasibility study of in vivo electromagnetic imaging. *Physics in Medicine and Biology*, 38(1):151–160, January 1993. ISSN 0031-9155, 1361-6560. doi: 10.1088/0031-9155/38/1/011.
- [24] Nataša Terzija, Wuliang Yin, Gunter Gerbeth, Frank Stefani, Klaus Timmel, Thomas Wondrak, and Anthony Peyton. Electromagnetic inspection of a two-phase flow of gainsn and argon. *Flow Measurement and Instrumentation*, 22(1):10 – 16, 2011. ISSN 0955-5986. doi: <https://doi.org/10.1016/j.flowmeasinst.2010.10.003>.
- [25] Thomas Wondrak and Manuchehr Soleimani. A novel metal flow imaging using electrical capacitance tomography. *Measurement Science and Technology*, 28(6):064001, jun 2017. ISSN 0957-0233. doi: 10.1088/1361-6501/aa670c.
- [26] Kenji Suzuki. Overview of deep learning in medical imaging. *Radiological Physics and Technology*, 10(3):257–273, September 2017. ISSN 1865-0333, 1865-0341. doi: 10.1007/s12194-017-0406-5.
- [27] Zhenwei Zhang and Ervin Sejdić. Radiological images and machine learning: Trends, perspectives, and prospects. *Computers in Biology and Medi-*



- cine*, 108:354–370, 2019. ISSN 0010-4825. doi: <https://doi.org/10.1016/j.compbio.2019.02.017>.
- [28] G. Wang. A perspective on deep imaging. *IEEE Access*, 4:8914–8924, 2016. ISSN 2169-3536. doi: 10.1109/ACCESS.2016.2624938.
- [29] Mauricio Araya-Polo, Joseph Jennings, Amir Adler, and Taylor Dahlke. Deep-learning tomography. *The Leading Edge*, 37(1):58–66, 2018. doi: 10.1190/tle37010058.1.
- [30] Ge Wang, Jong Chul Ye, and Bruno De Man. Deep learning for tomographic image reconstruction. *Nature Machine Intelligence*, 2(12):737–748, December 2020. ISSN 2522-5839. doi: 10.1038/s42256-020-00273-z.
- [31] Y. Wu, B. Chen, K. Liu, C. Zhu, H. Pan, J. Jia, H. Wu, and J. Yao. Shape reconstruction with multiphase conductivity for electrical impedance tomography using improved convolutional neural network method. *IEEE Sensors Journal*, pages 1–1, 2021. ISSN 1558-1748. doi: 10.1109/JSEN.2021.3050845.
- [32] Z. Wei, D. Liu, and X. Chen. Dominant-current deep learning scheme for electrical impedance tomography. *IEEE Transactions on Biomedical Engineering*, 66(9):2546–2555, Sep. 2019. ISSN 1558-2531. doi: 10.1109/TBME.2019.2891676.
- [33] Zuohui Chen, Qing Yuan, Xujie Song, Cheng Chen, Dan Zhang, Yun Xiang, Ruigang Liu, and Qi Xuan. Mitnet: Gan enhanced magnetic induction tomography based on complex cnn, 2021.
- [34] J. Yao, H. Chen, Z. Xu, J. Huang, J. Li, J. Jia, and H. Wu. Development of a wearable electrical impedance tomographic sensor for gesture recognition with machine learning. *IEEE Journal of Biomedical and Health Informatics*, 24(6):1550–1556, June 2020. ISSN 2168-2208. doi: 10.1109/JBHI.2019.2945593.
- [35] Shizuo Kaji and Satoshi Kida. Overview of image-to-image translation by use of deep neural networks: denoising, super-resolution, modality conversion, and reconstruction in medical imaging. *Radiological Physics and*

- Technology*, 12(3):235–248, September 2019. ISSN 1865-0333, 1865-0341. doi: 10.1007/s12194-019-00520-y.
- [36] Hyunkwang Lee, Chao Huang, Sehyo Yune, Shahein H. Tajmir, Myeongchan Kim, and Synho Do. Machine Friendly Machine Learning: Interpretation of Computed Tomography Without Image Reconstruction. *Scientific Reports*, 9(1):15540, December 2019. ISSN 2045-2322. doi: 10.1038/s41598-019-51779-5.
  - [37] O. Costilla-Reyes, P. Scully, and K. B. Ozanyan. Deep neural networks for learning spatio-temporal features from tomography sensors. *IEEE Transactions on Industrial Electronics*, 65(1):645–653, Jan 2018. ISSN 1557-9948. doi: 10.1109/TIE.2017.2716907.
  - [38] Jinku Li, Delin Hu, Wei Chen, Yi Li, Maomao Zhang, and Lihui Peng. Cnn-based volume flow rate prediction of oil–gas–water three-phase intermittent flow from multiple sensors. *Sensors*, 21(4), 2021. ISSN 1424-8220. doi: 10.3390/s21041245.
  - [39] Qiang Guo, Mao Ye, Wuqiang Yang, and Zhongmin Liu. A machine learning approach for electrical capacitance tomography measurement of gas–solid fluidized beds. *AIChE Journal*, 65(6):e16583, 2019. doi: <https://doi.org/10.1002/aic.16583>.
  - [40] Wuliang Yin. Electro-magnetic tomography (EMT) sensors. In Wuqiang Yang, editor, *Imaging Sensor Technologies and Applications*, pages 405–428. Institution of Engineering and Technology, July 2020. ISBN 9781785614972 9781785614989. doi: 10.1049/PBCE116E\_ch12.
  - [41] Lu Ma. *Magnetic Induction Tomography for Non-destructive Evaluation and Process Tomography*. PhD Thesis, University of Bath, October 2014.
  - [42] Fang Li. *Low Conductivity Magnetic Induction Tomography for Landmine Detection*. PhD Thesis, University of Bath, September 2018.
  - [43] Imamul Muttakin and Manuchehr Soleimani. Direct capacitance measurement for tomographic imaging of metallic object. In *9th World Congress in Industrial Process Tomography*, pages 509–514, 2018.

- [44] I. Muttakin, T. Wondrak, and M. Soleimani. Magnetic induction tomography sensors for quantitative visualization of liquid metal flow shape. *IEEE Sensors Letters*, 4(7):1–4, July 2020. ISSN 2475-1472. doi: 10.1109/LSENS.2020.3000292.
- [45] Imamul Muttakin and Manuchehr Soleimani. Magnetic induction tomography spectroscopy for structural and functional characterization in metallic materials. *Materials*, 13(11):2639, Jun 2020. ISSN 1996-1944. doi: 10.3390/ma13112639.
- [46] I. Muttakin and M. Soleimani. Noninvasive conductivity and temperature sensing using magnetic induction spectroscopy imaging. *IEEE Transactions on Instrumentation and Measurement*, 70:1–11, 2021. ISSN 1557-9662. doi: 10.1109/TIM.2020.3016435.
- [47] Imamul Muttakin and Manuchehr Soleimani. Interior void classification in liquid metal using multi-frequency magnetic induction tomography with a machine learning approach. *IEEE Sensors Journal*, pages 1–1, 2021. doi: 10.1109/JSEN.2021.3109629.
- [48] E Al Hosani, M Zhang, J F P J Abascal, and M Soleimani. Imaging metallic samples using electrical capacitance tomography: forward modelling and reconstruction algorithms. *Measurement Science and Technology*, 27(11):115402, nov 2016. ISSN 0957-0233. doi: 10.1088/0957-0233/27/11/115402.
- [49] M. Zhang and M. Soleimani. Imaging floating metals and dielectric objects using electrical capacitance tomography. *Measurement: Journal of the International Measurement Confederation*, 74:143–149, oct 2015. ISSN 02632241. doi: 10.1016/j.measurement.2015.07.009.
- [50] W Warsito, Q Marashdeh, and L Fan. Electrical Capacitance Volume Tomography. *IEEE Sensors Journal*, 7(4):525–535, 2007. ISSN 1530-437X VO - 7. doi: 10.1109/JSEN.2007.891952.
- [51] Kai Huang, Shuanghe Meng, Qiang Guo, Wuqiang Yang, Tao Zhang, Mao Ye, and Zhongmin Liu. Effect of Electrode Length of an Electrical Capacitance Tomography Sensor on Gas–Solid Fluidized Bed Measurements.

- Industrial & Engineering Chemistry Research*, 58(47):21827–21841, November 2019. ISSN 0888-5885, 1520-5045. doi: 10.1021/acs.iecr.9b03988.
- [52] A. Yusuf, I. Muttakin, W. Widada, and W.P. Taruno. Analysis of single excitation signal for high speed ECVT data acquisition system. In *Proceedings - 2014 6th International Conference on Information Technology and Electrical Engineering: Leveraging Research and Technology Through University-Industry Collaboration, ICITEE 2014*, 2015. ISBN 9781479953035. doi: 10.1109/ICITEED.2014.7007953.
  - [53] Q Marashdeh, W Warsito, L Fan, and F L Teixeira. A Multimodal Tomography System Based on ECT Sensors. *IEEE Sensors Journal*, 7(3):426–433, 2007. ISSN 1530-437X VO - 7. doi: 10.1109/JSEN.2006.890149.
  - [54] I. Muttakin, A. Yusuf, Rohmadi, W. Widada, and W.P. Taruno. Design and simulation of quadrature phase detection in electrical capacitance volume tomography. *Telkomnika (Telecommunication Computing Electronics and Control)*, 13(1), 2015. ISSN 23029293 16936930. doi: 10.12928/TELKOMNIKA.v13i1.1299.
  - [55] M.I. Ikhsanti, R. Bouzida, S.K. Wijaya, Rohmadi, I. Muttakin, and W.P. Taruno. Capacitance-digital and impedance converter as electrical tomography measurement system for biological tissue. In *AIP Conference Proceedings*, volume 1817, 2017. ISBN 9780735414853. doi: 10.1063/1.4976798.
  - [56] J Sun, Z Ren, and W Yang. 3D imaging with single-plane electrical capacitance tomography sensor. *Electronics Letters*, 51(3):222–224, 2015. ISSN 0013-5194 VO - 51. doi: 10.1049/el.2014.3667.
  - [57] Z. Z. Yu, A. T. Peyton, M. S. Beck, W. F. Conway, and L. A. Xu. Imaging system based on electromagnetic tomography (emt). *Electronics Letters*, 29(7):625–626, April 1993. ISSN 0013-5194. doi: 10.1049/el:19930418.
  - [58] A J Peyton, Z Z Yu, G Lyon, S Al-Zeibak, J Ferreira, J Velez, F Linhares, A R Borges, H L Xiong, N H Saunders, and M S Beck. An overview of electromagnetic inductance tomography: description of three different systems. *Measurement Science and Technology*, 7(3):261–271, mar 1996. doi: 10.1088/0957-0233/7/3/006.

- [59] M. Soleimani, W. R. B. Lionheart, and A. J. Peyton. Image reconstruction for high-contrast conductivity imaging in mutual induction tomography for industrial applications. *IEEE Transactions on Instrumentation and Measurement*, 56(5):2024–2032, Oct 2007. ISSN 1557-9662. doi: 10.1109/TIM.2007.895598.
- [60] A J Peyton. Electromagnetic induction tomography. In Mi Wang, editor, *Industrial Tomography: Systems and Applications*, pages 61–107. Woodhead Publishing, 2015. ISBN 978-1-78242-118-4. doi: <https://doi.org/10.1016/B978-1-78242-118-4.00003-4>.
- [61] J. R. Mortarelli. A generalization of the geselowitz relationship useful in impedance plethysmographic field calculations. *IEEE Transactions on Bio-medical Engineering*, BME-27(11):665–667, Nov 1980. ISSN 1558-2531. doi: 10.1109/TBME.1980.326677.
- [62] B. A. Auld and J. C. Moulder. Review of advances in quantitative eddy current nondestructive evaluation. *Journal of Nondestructive Evaluation*, 18(1):3–36, Mar 1999. ISSN 1573-4862. doi: 10.1023/A:1021898520626.
- [63] C Ktistis, D W Armitage, and A J Peyton. Calculation of the forward problem for absolute image reconstruction in MIT. *Physiological Measurement*, 29(6):S455–S464, jun 2008. doi: 10.1088/0967-3334/29/6/s38.
- [64] Stephen J Norton and John R Bowler. Theory of eddy current inversion. *Journal of Applied Physics*, 73(2):501–512, 1993.
- [65] Karl Hollaus, Christian Magele, Robert Merwa, and Hermann Scharfetter. Fast calculation of the sensitivity matrix in magnetic induction tomography by tetrahedral edge finite elements and the reciprocity theorem. *Physiological measurement*, 25(1):159, 2004.
- [66] Manuchehr Soleimani and William RB Lionheart. Absolute conductivity reconstruction in magnetic induction tomography using a nonlinear method. *IEEE Transactions on medical imaging*, 25(12):1521–1530, 2006.
- [67] Wuliang Yin and Anthony J Peyton. Sensitivity formulation including velocity effects for electromagnetic induction systems. *IEEE Transactions on Magnetism*, 46(5):1172–1176, 2010.

- [68] DN Dyck, DA Lowther, and EM Freeman. A method of computing the sensitivity of electromagnetic quantities to changes in materials and sources. *IEEE Transactions on Magnetics*, 30(5):3415–3418, 1994.
- [69] M. Soleimani and W. R. B. Lionheart. Image reconstruction in three-dimensional magnetostatic permeability tomography. *IEEE Transactions on Magnetics*, 41(4):1274–1279, April 2005. ISSN 1941-0069. doi: 10.1109/TMAG.2005.845158.
- [70] Frank Stefani, Thomas Gundrum, and Gunter Gerbeth. Contactless inductive flow tomography. *Phys. Rev. E*, 70:056306, Nov 2004. doi: 10.1103/PhysRevE.70.056306.
- [71] Matthias Ratajczak, Thomas Gundrum, Frank Stefani, and Thomas Wondrak. Contactless Inductive Flow Tomography: Brief History and Recent Developments in Its Application to Continuous Casting. *Journal of Sensors*, 2014:1–9, 2014. ISSN 1687-725X, 1687-7268. doi: 10.1155/2014/739161.
- [72] F Stefani and G Gerbeth. A contactless method for velocity reconstruction in electrically conducting fluids. *Measurement Science and Technology*, 11(6):758–765, June 2000. ISSN 0957-0233, 1361-6501. doi: 10.1088/0957-0233/11/6/319.
- [73] F Stefani and G Gerbeth. Velocity reconstruction in conducting fluids from magnetic field and electric potential measurements. *Inverse Problems*, 15(3):771–786, June 1999. ISSN 0266-5611, 1361-6420. doi: 10.1088/0266-5611/15/3/309.
- [74] T Wondrak, V Galindo, G Gerbeth, T Gundrum, F Stefani, and K Timmel. Contactless inductive flow tomography for a model of continuous steel casting. *Measurement Science and Technology*, 21(4):045402, April 2010. ISSN 0957-0233, 1361-6501. doi: 10.1088/0957-0233/21/4/045402.
- [75] Lifeng Zhang, Subo Yang, Kaike Cai, Jiying Li, Xiaoguang Wan, and Brian G. Thomas. Investigation of Fluid Flow and Steel Cleanliness in the Continuous Casting Strand. *Metallurgical and Materials Transactions B*, 38(1):63–83, April 2007. ISSN 1073-5615, 1543-1916. doi: 10.1007/s11663-006-9007-0.

- [76] Cesar Augusto Real-Ramirez, Ignacio Carvajal-Mariscal, Florencio Sanchez-Silva, Francisco Cervantes-de la Torre, Jose Raul Miranda-Tello, Ruslan Gabbasov, and Jesus Isidro Gonzalez-Trejo. Visualization and measurement of turbulent flow inside a SEN and off the ports. *Revista Mexicana de Física*, 67(4 Jul-Aug):040601 1–10, July 2021. ISSN 2683-2224. doi: 10.31349/RevMexFis.67.040601.
- [77] Klaus Timmel, Sven Eckert, Gunter Gerbeth, Frank Stefani, and Thomas Wondrak. Experimental Modeling of the Continuous Casting Process of Steel Using Low Melting Point Metal Alloys—the LIMMCAST Program. *ISIJ International*, 50(8):1134–1141, 2010. doi: 10.2355/isijinternational.50.1134.
- [78] Xu-feng Qin, Chang-gui Cheng, Yang Li, Wei-li Wu, and Yan Jin. Effects of argon blowing at tundish upper nozzle on multiphase flow behavior in nozzle. *Journal of Iron and Steel Research International*, September 2021. ISSN 2210-3988. doi: 10.1007/s42243-021-00648-5.
- [79] K. Chattopadhyay, S. Dinda, J. Sengupta, and A. Srivastava. A Comparative Study on the Characterization of Bubbles Inside a Ladle and a Continuous Casting Mold During Gas Injection Using Advanced Imaging Techniques. In *AISTech 2021 Proceedings of the Iron and Steel Technology Conference*, pages 1687–1698. AIST, 2021. ISBN 9781935117940. doi: 10.33313/382/172.
- [80] Dhiren Makwana and Jignesh Thaker. Identification of Gas-Liquid Two-Phase Flow Patterns Using Various Experimental Techniques: A Review. In Basant Singh Sikarwar, Bengt Sundén, and Qiuwang Wang, editors, *Advances in Fluid and Thermal Engineering*, Lecture Notes in Mechanical Engineering, pages 767–775, Singapore, 2021. Springer. ISBN 9789811601590. doi: 10.1007/978-981-16-0159-0\_67.
- [81] D. Xie, Z. Huang, H. Ji, and H. Li. An online flow pattern identification system for gas–oil two-phase flow using electrical capacitance tomography. *IEEE Transactions on Instrumentation and Measurement*, 55(5): 1833–1838, Oct 2006. doi: 10.1109/TIM.2006.881558.
- [82] Robert Banasiak, Radosław Wajman, Tomasz Jaworski, Paweł Fiderek,

- Henryk Fidos, Jacek Nowakowski, and Dominik Sankowski. Study on two-phase flow regime visualization and identification using 3d electrical capacitance tomography and fuzzy-logic classification. *International Journal of Multiphase Flow*, 58:1 – 14, 2014. ISSN 0301-9322. doi: <https://doi.org/10.1016/j.ijmultiphaseflow.2013.07.003>.
- [83] Pawel Fiderek, Jacek Kucharski, and Radoslaw Wajman. Fuzzy inference for two-phase gas-liquid flow type evaluation based on raw 3d ect measurement data. *Flow Measurement and Instrumentation*, 54:88 – 96, 2017. ISSN 0955-5986. doi: <https://doi.org/10.1016/j.flowmeasinst.2016.12.010>.
- [84] J. Pusppanathan, R. Abdul Rahim, F. A. Phang, E. J. Mohamad, N. M. Nor Ayob, M. H. Fazalul Rahiman, and C. Kok Seong. Single-plane dual-modality tomography for multiphase flow imaging by integrating electrical capacitance and ultrasonic sensors. *IEEE Sensors Journal*, 17(19):6368–6377, Oct 2017. doi: 10.1109/JSEN.2017.2731867.
- [85] Gelu-Ovidiu Tirian, Ioan Filip, and Gabriela Proştean. Adaptive control system for continuous steel casting based on neural networks and fuzzy logic. *Neurocomputing*, 125:236 – 245, 2014. ISSN 0925-2312. doi: <https://doi.org/10.1016/j.neucom.2012.11.052>. Advances in Neural Network Research and Applications Advances in Bio-Inspired Computing: Techniques and Applications.
- [86] M. Dussud, S. Galichet, and L. P. Foulloy. Application of fuzzy logic control for continuous casting mold level control. *IEEE Transactions on Control Systems Technology*, 6(2):246–256, March 1998. doi: 10.1109/87.664191.
- [87] Yunosuke Maki, Nobuhiro Takashima, Hiroshi Obata, Osamu Iida, Kazuma Nakashima, and Toshiro Sawada. Application of fuzzy theory to ironmaking process control. *Kawasaki Steel Giho*, 22(3):196–202, 1990.
- [88] I. Glavinić, S. Abouelazayem, M. Ratajczak, D. Schurmann, S. Eckert, F. Stefani, J. Hlava, and T. Wondrak. Flow control in the model of a continuous caster by using contactless inductive flow tomography. In Guillaume Lambotte, Jonghyun Lee, Antoine Allanore, and Samuel Wagstaff, editors, *Materials Processing Fundamentals 2019*, pages 49–58, Cham, 2019. Springer International Publishing. ISBN 978-3-030-05728-2.



- [89] Tomas Mauder, Cenek Sandera, and Josef Stetina. Optimal control algorithm for continuous casting process by using fuzzy logic. *steel research international*, 86(7):785–798, 2015. doi: 10.1002/srin.201400213.
- [90] N. Kiupel, P.M. Frank, and J. Wochnik. Improvement of mold-level control using fuzzy logic. *Engineering Applications of Artificial Intelligence*, 7(5):493 – 499, 1994. ISSN 0952-1976. doi: [https://doi.org/10.1016/0952-1976\(94\)90028-0](https://doi.org/10.1016/0952-1976(94)90028-0).
- [91] U Hampel, T. Wondrak, M. Fjeld, R. Mudde, L. Portela, S. Kenjeres, D. Legendre, G. Link, T. Koironen, J. Hlava, L. Babout, L. Jackowska-Strumiłło, M. Soleimani, M. Vaukhonen, T. Lähivaara, T. Rymarczyk, M. Trepte, A. Voutilainen, M. Rodriguez, J. Bos, S. Betz, J. Hysky, P. Pennerstorfer, M. Goldammer, C. Matten, R. Hoffmann, J.-P. Gingras, D. van der Plas, P. Veenstra, J. Nurmi, C. Pudack, and M. J. da Silva. Tomocon: A Marie Skłodowska-Curie European training network on tomography-based control in industrial processes. In *9th World Congress in Industrial Process Tomography*, page 891, 2018.
- [92] Manuchehr Soleimani, Fang Li, Stefano Spagnul, Juan Palacios, José I Barbero, Teresa Gutiérrez, and Alberto Viotto. In situ steel solidification imaging in continuous casting using magnetic induction tomography. *Measurement Science and Technology*, 31(6):065401, mar 2020. doi: 10.1088/1361-6501/ab6f30.
- [93] O. Bíró. Edge element formulations of eddy current problems. *Computer Methods in Applied Mechanics and Engineering*, 169(3-4):391–405, 1999. doi: 10.1016/S0045-7825(98)00165-0.
- [94] B. Rivière. *Discontinuous Galerkin Methods for Solving Elliptic and Parabolic Equations: Theory and Implementation*, 2008.
- [95] Lu Ma, Robert Banasiak, and Manuchehr Soleimani. Magnetic Induction Tomography with High Performance GPU Implementation. *Progress In Electromagnetics Research B*, 65:49–63, 2016. ISSN 1937-6472. doi: 10.2528/PIERB15101902.
- [96] W Q Yang, D M Spink, T A York, and H McCann. An image-reconstruction

- algorithm based on landweber's iteration method for electrical-capacitance tomography. *Measurement Science and Technology*, 10(11):1065–1069, sep 1999. doi: 10.1088/0957-0233/10/11/315.
- [97] B. Brandstätter. Jacobian calculation for electrical impedance tomography based on the reciprocity principle. *IEEE Transactions on Magnetics*, 39(3 I):1309–1312, 2003. doi: 10.1109/TMAG.2003.810390.
  - [98] X. Liu and L. Huang. Split bregman iteration algorithm for total bounded variation regularization based image deblurring. *Journal of Mathematical Analysis and Applications*, 372(2):486–495, 2010. doi: 10.1016/j.jmaa.2010.07.013.
  - [99] B. Chen, J.F.P.J. Abascal, and M. Soleimani. Electrical resistance tomography for visualization of moving objects using a spatiotemporal total variation regularization algorithm. *Sensors (Switzerland)*, 18(6), 2018. doi: 10.3390/s18061704.
  - [100] J.F.P.J. Abascal, P. Montesinos, E. Marinetto, J. Pascau, and M. Desco. Comparison of total variation with a motion estimation based compressed sensing approach for self-gated cardiac cine mri in small animal studies. *PLoS ONE*, 9(10), 2014. doi: 10.1371/journal.pone.0110594.
  - [101] P. Montesinos, J.F.P.J. Abascal, L. Cussó, J.J. Vaquero, and M. Desco. Application of the compressed sensing technique to self-gated cardiac cine sequences in small animals. *Magnetic Resonance in Medicine*, 72(2):369–380, 2014. doi: 10.1002/mrm.24936.
  - [102] S. Osher, M. Burger, D. Goldfarb, J. Xu, and W. Yin. An iterative regularization method for total variation-based image restoration. *Multiscale Modeling and Simulation*, 4(2):460–489, 2005. doi: 10.1137/040605412.
  - [103] T. Goldstein and S. Osher. The split bregman method for l1-regularized problems. *SIAM Journal on Imaging Sciences*, 2(2):323–343, 2009. doi: 10.1137/080725891.
  - [104] Martin H Gutknecht. A brief introduction to krylov space methods for solving linear systems. In *Frontiers of Computational Science*, pages 53–62. Springer, 2007.

- [105] Manuchehr Soleimani, William Lionheart, Claudia Riedel, and Olaf Dossel. Forward problem in 3d magnetic induction tomography (mit). page 275, 09 2003.
- [106] Naif Alqahtani, Fatimah Alzubaidi, Ryan T. Armstrong, Pawel Swietojanski, and Peyman Mostaghimi. Machine learning for predicting properties of porous media from 2d x-ray images. *Journal of Petroleum Science and Engineering*, 184:106514, 2020. ISSN 0920-4105. doi: <https://doi.org/10.1016/j.petrol.2019.106514>.
- [107] Wuliang Yin, Guang Chen, Lijing Chen, and Ben Wang. The design of a digital magnetic induction tomography (mit) system for metallic object imaging based on half cycle demodulation. *IEEE Sensors Journal*, 11(10): 2233–2240, 2011. doi: 10.1109/JSEN.2011.2128866.
- [108] Ziqi Chen, Haibin Hao, J R Salas-Avila, Mingyang Fan, Yuedong Xie, Shupeí Wang, Jiyao Li, Jianxin Xu, Hua Wang, and Wuliang Yin. Estimation of metal state in molten production processes using electromagnetic tomography with fast integrated processing. *Measurement Science and Technology*, 33(7):074003, apr 2022. doi: 10.1088/1361-6501/ac62aa.
- [109] Chao Tan, Yixuan Chen, Yiran Wu, Zhili Xiao, and Feng Dong. A modular magnetic induction tomography system for low-conductivity medium imaging. *IEEE Transactions on Instrumentation and Measurement*, 70:1–8, 2021. doi: 10.1109/TIM.2021.3073439.
- [110] Daniel S. Batista, Guilherme B. Silva, Francisco Granziera, Marcelo C. Tosin, Décio L. Gazzoni Filho, and Leonimer F. Melo. Howland current source applied to magnetic field generation in a tri-axial helmholtz coil. *IEEE Access*, 7:125649–125661, 2019. doi: 10.1109/ACCESS.2019.2939117.
- [111] Gavin Dingley and Manuchehr Soleimani. Multi-frequency magnetic induction tomography system and algorithm for imaging metallic objects. *Sensors*, 21(11):3671, May 2021. ISSN 1424-8220. doi: 10.3390/s21113671.
- [112] Thomas Wondrak, Sven Eckert, Gunter Gerbeth, Konrad Klotsche, Frank Stefani, Klaus Timmel, Anthony J Peyton, Natasa Terzija, and Wuliang Yin. Combined Electromagnetic Tomography for Determining Two-phase

- Flow Characteristics in the Submerged Entry Nozzle and in the Mold of a Continuous Casting Model. *Metallurgical and Materials Transactions B*, 42(6):1201–1210, 2011. ISSN 1543-1916. doi: 10.1007/s11663-011-9553-y.
- [113] Lifeng Zhang and Brian G. Thomas. State of the art in evaluation and control of steel cleanliness. *ISIJ International*, 43(3):271–291, 2003. doi: 10.2355/isijinternational.43.271.
- [114] Yuriy Plevachuk, Vasyl Sklyarchuk, Sven Eckert, Gunter Gerbeth, and Rada Novakovic. Thermophysical Properties of the Liquid Ga–In–Sn Eutectic Alloy. *Journal of Chemical & Engineering Data*, 59(3):757–763, mar 2014. ISSN 0021-9568. doi: 10.1021/je400882q.
- [115] Ivan Glavinić, Imamul Muttakin, Shereen Abouelazayem, Artem Blishchik, Frank Stefani, Sven Eckert, Manuchehr Soleimani, Iheb Saidani, Jaroslav Hlava, Saša Kenjereš, and Thomas Wondrak. Laboratory investigation of tomography-controlled continuous steel casting. *Sensors*, 22(6):2195, Mar 2022. ISSN 1424-8220. doi: 10.3390/s22062195.
- [116] Jaroslav Hlava and Shereen Abouelazayem. Control systems with tomographic sensors—a review. *Sensors*, 22(8):2847, Apr 2022. ISSN 1424-8220. doi: 10.3390/s22082847.
- [117] Klaus Timmel, Natalia Shevchenko, Michael Röder, Marc Anderhuber, Pascal Gardin, Sven Eckert, and Gunter Gerbeth. Visualization of Liquid Metal Two-phase Flows in a Physical Model of the Continuous Casting Process of Steel. *Metallurgical and Materials Transactions B*, 46(2):700–710, 2015. ISSN 1543-1916. doi: 10.1007/s11663-014-0231-8.
- [118] Slawomir Tumanski. Induction coil sensors—a review. *Measurement Science and Technology*, 18(3):R31–R46, 2007. ISSN 0957-0233. doi: 10.1088/0957-0233/18/3/r01.
- [119] F. N. Adiputri, E. N. Prasetiani, Rohmadi, A. Saputra, I. Muttakin, and W. P. Taruno. Simulation of magnetic induction tomography sensor with 8-coils solenoid and planar. In *2017 5th International Conference on Instrumentation, Communications, Information Technology, and Biomedical*

- Engineering (ICICI-BME)*, pages 1–5, Nov 2017. doi: 10.1109/ICICI-BME.2017.8537753.
- [120] M. Al-Hawari, A. I. Aulia, A. Rudin, Rohmadi, I. Muttakin, and W. P. Taruno. Receiver circuit design for signal conditioning in magnetic induction tomography system. In *2017 5th International Conference on Instrumentation, Communications, Information Technology, and Biomedical Engineering (ICICI-BME)*, pages 1–6, Nov 2017. doi: 10.1109/ICICI-BME.2017.8537732.
  - [121] Hsin-Yu Wei and M Soleimani. Two-phase low conductivity flow imaging using magnetic induction tomography. *Progress In Electromagnetics Research*, 131:99–115, 2012. doi: 10.2528/PIER12070615.
  - [122] S. Chowdhury, Q. M. Marashdeh, and F. L. Teixeira. Inverse normalization method for cross-sectional imaging and velocimetry of two-phase flows based on electrical capacitance tomography. *IEEE Sensors Letters*, 2(1): 1–4, March 2018. ISSN 2475-1472. doi: 10.1109/LSENS.2018.2806845.
  - [123] C. G. Xie, S. M. Huang, C. P. Lenn, A. L. Stott, and M. S. Beck. Experimental evaluation of capacitance tomographic flow imaging systems using physical models. *IEE Proceedings - Circuits, Devices and Systems*, 141(5): 357–368, Oct 1994. ISSN 1350-2409. doi: 10.1049/ip-cds:19941152.
  - [124] François Chollet et al. Keras. <https://keras.io>, 2015.
  - [125] Martín Abadi, Ashish Agarwal, Paul Barham, Eugene Brevdo, Zhifeng Chen, Craig Citro, Greg S. Corrado, Andy Davis, Jeffrey Dean, Matthieu Devin, Sanjay Ghemawat, Ian Goodfellow, Andrew Harp, Geoffrey Irving, Michael Isard, Yangqing Jia, Rafal Jozefowicz, Lukasz Kaiser, Manjunath Kudlur, Josh Levenberg, Dandelion Mané, Rajat Monga, Sherry Moore, Derek Murray, Chris Olah, Mike Schuster, Jonathon Shlens, Benoit Steiner, Ilya Sutskever, Kunal Talwar, Paul Tucker, Vincent Vanhoucke, Vijay Vasudevan, Fernanda Viégas, Oriol Vinyals, Pete Warden, Martin Wattenberg, Martin Wicke, Yuan Yu, and Xiaoqiang Zheng. TensorFlow: Large-scale machine learning on heterogeneous systems, 2015. Software available from [tensorflow.org](http://tensorflow.org).

- [126] Carl Kusche, Tom Reclik, Martina Freund, Talal Al-Samman, Ulrich Kerzel, and Sandra Korte-Kerzel. Large-area, high-resolution characterisation and classification of damage mechanisms in dual-phase steel using deep learning. *PLOS ONE*, 14(5):1–22, 05 2019. doi: 10.1371/journal.pone.0216493.
- [127] J. García-Martín, J. Gómez-Gil, and E. Vázquez-Sánchez. Non-destructive techniques based on eddy current testing. *Sensors*, 11(3):2525–2565, 2011. doi: 10.3390/s110302525.
- [128] X. Chen and Y. Lei. Electrical conductivity measurement of ferromagnetic metallic materials using pulsed eddy current method. *NDT and E International*, 75:33–38, 2015. doi: 10.1016/j.ndteint.2015.06.005.
- [129] N. Bowler and Y. Huang. Electrical conductivity measurement of metal plates using broadband eddy-current and four-point methods. *Measurement Science and Technology*, 16(11):2193–2200, 2005. doi: 10.1088/0957-0233/16/11/009.
- [130] A. Sophian, G. Tian, and M. Fan. Pulsed eddy current non-destructive testing and evaluation: A review. *Chinese Journal of Mechanical Engineering (English Edition)*, 30(3):500–514, 2017. doi: 10.1007/s10033-017-0122-4.
- [131] G.Y. Tian, Y. He, I. Adewale, and A. Simm. Research on spectral response of pulsed eddy current and nde applications. *Sensors and Actuators, A: Physical*, 189:313–320, 2013. doi: 10.1016/j.sna.2012.10.011.
- [132] R.T. Ko, M.P. Blodgett, S. Sathish, and T.R. Boehnlein. A novel multi-frequency eddy current measurement technique for materials characterization. volume 820 I, pages 415–422, 2006. doi: 10.1063/1.2184558.
- [133] W. Cheng. Thickness measurement of metal plates using swept-frequency eddy current testing and impedance normalization. *IEEE Sensors Journal*, 17(14):4558–4569, 2017. doi: 10.1109/JSEN.2017.2710356.
- [134] M. Lu, Y. Xie, W. Zhu, A. Peyton, and W. Yin. Determination of the magnetic permeability, electrical conductivity, and thickness of ferrite metallic plates using a multifrequency electromagnetic sensing system.

- IEEE Transactions on Industrial Informatics*, 15(7):4111–4119, 2019. doi: 10.1109/TII.2018.2885406.
- [135] J. Xiang, Z. Chen, Y. Dong, and Y. Yang. Image reconstruction for multi-frequency electromagnetic tomography based on multiple measurement vector model. 2020. doi: 10.1109/I2MTC43012.2020.9128898.
  - [136] A. Pirani, M. Ricci, R. Specogna, A. Tamburrino, and F. Trevisan. Multi-frequency identification of defects in conducting media. *Inverse Problems*, 24(3), 2008. doi: 10.1088/0266-5611/24/3/035011.
  - [137] Z. Zhang, M.A. Roula, and R. Dinsdale. Magnetic induction spectroscopy for biomass measurement: A feasibility study. *Sensors (Switzerland)*, 19(12), 2019. doi: 10.3390/s19122765.
  - [138] H. Scharfetter, R. Casañas, and J. Rosell. Biological tissue characterization by magnetic induction spectroscopy (mis): Requirements and limitations. *IEEE Transactions on Biomedical Engineering*, 50(7):870–880, 2003. doi: 10.1109/TBME.2003.813533.
  - [139] J. Rosell-Ferrer, R. Merwa, P. Brunner, and H. Scharfetter. A multifrequency magnetic induction tomography system using planar gradiometers: Data collection and calibration. *Physiological Measurement*, 27(5):S271–S280, 2006. doi: 10.1088/0967-3334/27/5/S23.
  - [140] P. Brunner, R. Merwa, A. Missner, J. Rosell, K. Hollaus, and H. Scharfetter. Reconstruction of the shape of conductivity spectra using differential multi-frequency magnetic induction tomography. *Physiological Measurement*, 27(5):S237–S248, 2006. doi: 10.1088/0967-3334/27/5/S20.
  - [141] S. Issa and H. Scharfetter. Detection and elimination of signal errors due to unintentional movements in biomedical magnetic induction tomography spectroscopy (mits). *Journal of Electrical Bioimpedance*, 9(1):163–175, 2018. doi: 10.2478/joeb-2018-0021.
  - [142] Wuliang Yin, S. J. Dickinson, and A. J. Peyton. Imaging the continuous conductivity profile within layered metal structures using inductance spectroscopy. *IEEE Sensors Journal*, 5(2):161–166, April 2005. ISSN 2379-9153. doi: 10.1109/JSEN.2004.842637.

- [143] W. Yin, S.J. Dickinson, and A.J. Peyton. Evaluating the permeability distribution of a layered conductor by inductance spectroscopy. *IEEE Transactions on Magnetics*, 42(11):3645–3651, 2006. doi: 10.1109/TMAG.2006.880992.
- [144] A. Barai, S. Watson, H. Griffiths, and R. Patz. Magnetic induction spectroscopy: Non-contact measurement of the electrical conductivity spectra of biological samples. *Measurement Science and Technology*, 23(8), 2012. doi: 10.1088/0957-0233/23/8/085501.
- [145] M.D. O’Toole, L.A. Marsh, J.L. Davidson, Y.M. Tan, D.W. Armitage, and A.J. Peyton. Non-contact multi-frequency magnetic induction spectroscopy system for industrial-scale bio-impedance measurement. *Measurement Science and Technology*, 26(3), 2015. doi: 10.1088/0957-0233/26/3/035102.
- [146] J.-Y. Wang, T. Healey, A. Barker, B. Brown, C. Monk, and D. Anumba. Magnetic induction spectroscopy (mis) - probe design for cervical tissue measurements. *Physiological Measurement*, 38(5):729–744, 2017. doi: 10.1088/1361-6579/aa6b4e.
- [147] C.A. Gonzalez, J.A. Valencia, A. Mora, F. Gonzalez, B. Velasco, M.A. Porras, J. Salgado, S.M. Polo, N. Hevia-Montiel, S. Cordero, and B. Rubinsky. Volumetric electromagnetic phase-shift spectroscopy of brain edema and hematoma. *PLoS ONE*, 8(5), 2013. doi: 10.1371/journal.pone.0063223.
- [148] L.A. Marsh, W. van Verre, J.L. Davidson, X. Gao, F.J.W. Podd, D.J. Daniels, and A.J. Peyton. Combining electromagnetic spectroscopy and ground-penetrating radar for the detection of anti-personnel landmines. *Sensors (Switzerland)*, 19(15), 2019. doi: 10.3390/s19153390.
- [149] G. El-Qady, M. Metwaly, and A. Khozaym. Tracing buried pipelines using multi frequency electromagnetic. *NRIAG J. Astron. Geophys.*, 3(1):101–107, 2014.
- [150] M. D. O’Toole, N. Karimian, and A. J. Peyton. Classification of nonferrous metals using magnetic induction spectroscopy. *IEEE Transactions on Industrial Informatics*, 14(8):3477–3485, Aug 2018. ISSN 1941-0050. doi: 10.1109/TII.2017.2786778.



- [151] H. Xu, M. Lu, J.R.S. Avila, Q. Zhao, F. Zhou, X. Meng, and W. Yin. Imaging a weld cross-section using a novel frequency feature in multi-frequency eddy current testing. *Insight: Non-Destructive Testing and Condition Monitoring*, 61(12):738–743, 2019. doi: 10.1784/insi.2019.61.12.738.
- [152] B. Dekdouk, C. Ktistis, D.W. Armitage, A.J. Peyton, R. Chapman, and M. Brown. Non-contact characterisation of conductivity gradient in isotropic polycrystalline graphite using inductance spectroscopy measurements. *Insight: Non-Destructive Testing and Condition Monitoring*, 53(2):90–95, 2011. doi: 10.1784/insi.2011.53.2.90.
- [153] A.J. Peyton, W. Yin, S.J. Dickinson, C.L. Davis, M. Strangwood, X. Hao, A.J. Douglas, and P.F. Morris. Monitoring microstructure changes in rod online by using induction spectroscopy. *Ironmaking and Steelmaking*, 37(2):135–139, 2010. doi: 10.1179/030192309X12506804200861.
- [154] C.L. Davis, M. Strangwood, and A.J. Peyton. Overview of non-destructive evaluation of steel microstructures using multifrequency electromagnetic sensors. *Ironmaking and Steelmaking*, 38(7):510–517, 2011. doi: 10.1179/030192311X13135947813816.
- [155] S.J. Dickinson, R. Binns, W. Yin, C. Davis, and A.J. Peyton. The development of a multifrequency electromagnetic instrument for monitoring the phase transformation of hot strip steel. *IEEE Transactions on Instrumentation and Measurement*, 56(3):879–886, 2007. doi: 10.1109/TIM.2007.894183.
- [156] H. Yang, F.D. van den Berg, C. Bos, A. Luinenburg, J. Mosk, P. Hunt, M. Dolby, J. Hinton, A.J. Peyton, and C.L. Davis. Em sensor array system and performance evaluation for in-line measurement of phase transformation in steel. *Insight: Non-Destructive Testing and Condition Monitoring*, 61(3):153–161, 2019. doi: 10.1784/insi.2019.61.3.153.
- [157] W. Zhu, H. Yang, A. Luinenburg, F. Van Den Berg, S. Dickinson, W. Yin, and A.J. Peyton. Development and deployment of online multifrequency electromagnetic system to monitor steel hot transformation on runout table of hot strip mill. *Ironmaking and Steelmaking*, 41(9):685–693, 2014. doi: 10.1179/1743281214Y.0000000183.

- [158] J. Shen, L. Zhou, W. Jacobs, P. Hunt, and C. Davis. Real-time in-line steel microstructure control through magnetic properties using an em sensor. *Journal of Magnetism and Magnetic Materials*, 490, 2019. doi: 10.1016/j.jmmm.2019.165504.
- [159] S. Lyons, K. Wei, and M. Soleimani. Wideband precision phase detection for magnetic induction spectroscopy. *Measurement: Journal of the International Measurement Confederation*, 115:45–51, 2018. doi: 10.1016/j.measurement.2017.09.013.
- [160] Lu Ma and Manuchehr Soleimani. Magnetic Induction Spectroscopy for Permeability Imaging. *Scientific Reports*, 8(1):7025, 2018. ISSN 2045-2322. doi: 10.1038/s41598-018-25507-4.
- [161] M. Soleimani. Computational aspects of low frequency electrical and electromagnetic tomography: A review study. *International Journal of Numerical Analysis and Modeling*, 5(3):407–440, 2008.
- [162] F. Li, J.F.P.J. Abascal, M. Desco, and M. Soleimani. Total variation regularization with split bregman-based method in magnetic induction tomography using experimental data. *IEEE Sensors Journal*, 17(4):976–985, 2017. doi: 10.1109/JSEN.2016.2637411.
- [163] Y. Ji, X. Meng, J. Shao, Y. Wu, and Q. Wu. The generalized skin depth for polarized porous media based on the cole-cole model. *Applied Sciences (Switzerland)*, 10(4), 2020. doi: 10.3390/app10041456.
- [164] S. Ley, S. Schilling, O. Fiser, J. Vrba, J. Sachs, and M. Helbig. Ultra-wideband temperature dependent dielectric spectroscopy of porcine tissue and blood in the microwave frequency range. *Sensors (Switzerland)*, 19(7), 2019. doi: 10.3390/s19071707.
- [165] James R. Wait. A conducting permeable sphere in the presence of a coil carrying an oscillating current. *Canadian Journal of Physics*, 31(4):670–678, 1953. doi: 10.1139/p53-062.
- [166] James R Wait. Some solutions for electromagnetic problems involving spheroidal, spherical and cylindrical bodies. *J. Res. Nat. Bur. Stand. B*, 64:15–32, 1960.

- [167] I. J. Won, D. A. Keiswetter, and T. H. Bell. Electromagnetic induction spectroscopy for clearing landmines. *IEEE Transactions on Geoscience and Remote Sensing*, 39(4):703–709, April 2001. ISSN 1558-0644. doi: 10.1109/36.917876.
- [168] Haoping Huang and I. J. Won. Automated identification of buried landmines using normalized electromagnetic induction spectroscopy. *IEEE Transactions on Geoscience and Remote Sensing*, 41(3):640–651, March 2003. ISSN 1558-0644. doi: 10.1109/TGRS.2003.809937.
- [169] O. A. Abdel-Rehim, J. L. Davidson, L. A. Marsh, M. D. O’Toole, and A. J. Peyton. Magnetic polarizability tensor spectroscopy for low metal anti-personnel mine surrogates. *IEEE Sensors Journal*, 16(10):3775–3783, May 2016. ISSN 2379-9153. doi: 10.1109/JSEN.2016.2535346.
- [170] David Ross-Pinnock and Paul G Maropoulos. Review of industrial temperature measurement technologies and research priorities for the thermal characterisation of the factories of the future. *Proceedings of the Institution of Mechanical Engineers, Part B: Journal of Engineering Manufacture*, 230(5):793–806, 2016. doi: 10.1177/0954405414567929.
- [171] B. Dekdouk, W. Yin, C. Ktistis, D. W. Armitage, and A. J. Peyton. A method to solve the forward problem in magnetic induction tomography based on the weakly coupled field approximation. *IEEE Transactions on Biomedical Engineering*, 57(4):914–921, April 2010. ISSN 1558-2531. doi: 10.1109/TBME.2009.2036733.
- [172] Keysight Technologies. Impedance measurement handbook: A guide to measurement technology and techniques, 2016.
- [173] Z. Cui, Y. Chen, and H. Wang. A dual-modality integrated sensor for electrical capacitance tomography and electromagnetic tomography. *IEEE Sensors Journal*, 19(21):10016–10026, Nov 2019. ISSN 2379-9153. doi: 10.1109/JSEN.2019.2927629.
- [174] H. Tesfalem, A. J. Peyton, A. D. Fletcher, M. Brown, and B. Chapman. Conductivity profiling of graphite moderator bricks from multi-frequency

- eddy current measurements. *IEEE Sensors Journal*, pages 1–1, 2020. ISSN 2379-9153. doi: 10.1109/JSEN.2020.2965201.
- [175] P. R. N. Childs, J. R. Greenwood, and C. A. Long. Review of temperature measurement. *Review of Scientific Instruments*, 71(8):2959–2978, 2000. doi: 10.1063/1.1305516.
- [176] R. Alfredo Osornio-Rios, J. A. Antonino-Daviu, and R. de Jesus Romero-Troncoso. Recent industrial applications of infrared thermography: A review. *IEEE Transactions on Industrial Informatics*, 15(2):615–625, 2019.
- [177] S. Bagavathiappan, B.B. Lahiri, T. Saravanan, John Philip, and T. Jayakumar. Infrared thermography for condition monitoring – a review. *Infrared Physics & Technology*, 60:35 – 55, 2013. ISSN 1350-4495. doi: <https://doi.org/10.1016/j.infrared.2013.03.006>.
- [178] John Banhart. Manufacturing routes for metallic foams. *JOM*, 52(12):22–27, December 2000. ISSN 1047-4838, 1543-1851. doi: 10.1007/s11837-000-0062-8.
- [179] Philippe Planquart, Chiara Spaccapaniccia, Giacomo Alessi, Sophia Buckingham, and Katrien Van Tichelen. Experimental and numerical characterization of the flow field at the core entrance of a water model of a heavy liquid metal-cooled reactor. *Nuclear Technology*, 206(2):231–241, 2020. doi: 10.1080/00295450.2019.1637240.
- [180] Wei Xu, Ke-Jun Xu, Jian-Ping Wu, Xin-Long Yu, and Xiao-Xue Yan. Peak-to-peak standard deviation based bubble detection method in sodium flow with electromagnetic vortex flowmeter. *Review of Scientific Instruments*, 90(6):065105, 2019. doi: 10.1063/1.5089690.
- [181] Itishree Mohanty and Dabashish Bhattacharjee. Artificial Neural Network and Its Application in Steel Industry. In Shubhabrata Datta and J. Paulo Davim, editors, *Computational Approaches to Materials Design: Theoretical and Practical Aspects*, pages 267–300. IGI Global, Hershey, PA, 2016. ISBN 9781522502906 9781522502913. doi: 10.4018/978-1-5225-0290-6.ch010.
- [182] David Cemernek, Sandra Cemernek, Heimo Gursch, Ashwini Pandeshwar,

- Thomas Leitner, Matthias Berger, Gerald Klösch, and Roman Kern. Machine learning in continuous casting of steel: a state-of-the-art survey. *Journal of Intelligent Manufacturing*, March 2021. ISSN 1572-8145. doi: 10.1007/s10845-021-01754-7.
- [183] H. Shin, H. R. Roth, M. Gao, L. Lu, Z. Xu, I. Nogues, J. Yao, D. Mollura, and R. M. Summers. Deep convolutional neural networks for computer-aided detection: Cnn architectures, dataset characteristics and transfer learning. *IEEE Transactions on Medical Imaging*, 35(5):1285–1298, May 2016. ISSN 1558-254X. doi: 10.1109/TMI.2016.2528162.
- [184] S. P. Sotiroudis, P. Sarigiannidis, S. K. Goudos, and K. Siakavara. Fusing diverse input modalities for path loss prediction: A deep learning approach. *IEEE Access*, 9:30441–30451, 2021. ISSN 2169-3536. doi: 10.1109/ACCESS.2021.3059589.
- [185] Yifeng Li, Xunpeng Qin, Zhenyuan Zhang, and Huanyu Dong. A robust identification method for nonferrous metal scraps based on deep learning and superpixel optimization. *Waste Management & Research*, 0(0):0734242X20987884, 2021. doi: 10.1177/0734242X20987884. PMID: 33499775.
- [186] Jin Zheng, Jinku Li, Yi Li, and Lihui Peng. A benchmark dataset and deep learning-based image reconstruction for electrical capacitance tomography. *Sensors*, 18(11), 2018. ISSN 1424-8220. doi: 10.3390/s18113701.
- [187] N. Vahabi, R. Yerworth, M. Miedema, A. van Kaam, R. Bayford, and A. Demosthenous. Deep analysis of eit dataset to classify apnea and non-apnea cases in neonatal patients. *IEEE Access*, 9:25131–25139, 2021. ISSN 2169-3536. doi: 10.1109/ACCESS.2021.3056558.
- [188] Haris Iqbal. Harisiqbal88/plotneuralnet v1.0.0, December 2018.